

NEW APPROACHES TO FUEL CELL DIAGNOSTICS

by

Omar Enrique Herrera

B.Sc. Universidad Nacional Autónoma de México, 2004

A THESIS SUBMITTED IN PARTIAL FULFILLMENT OF
THE REQUIREMENTS FOR THE DEGREE OF
DOCTOR OF PHILOSOPHY

in

The Faculty of Graduate Studies
(Mechanical Engineering)

THE UNIVERSITY OF BRITISH COLUMBIA

(Vancouver)

August 2011

© Omar Enrique Herrera, 2011

ABSTRACT

The durability and reliability of fuel cell products need to be improved. The lack of early diagnosis and failure-prevention techniques is one of the limiting factors. This thesis presents a non-invasive method for the early diagnosis of flooding, dehydration and low fuel stoichiometry (three common failure modes). The method is based on micro sensing electrodes (SE) that are placed at appropriate locations in a single cell. These electrodes have a characteristic potential response to each of the failure modes, which enables detection prior to overall fuel cell failure. The specific features in the measured responses (or combinations thereof) can be used to discern between different failure modes, and initiate corrective actions.

This thesis also reports on the separation of anodic and cathodic potentials in a working fuel cell via reference electrodes maintained at constant conditions. The reference electrodes consisted of four platinized platinum electrode wires and two patches of the same catalyst layer used in the anode. All the reference electrodes were unaffected by the operating conditions of the fuel cell and those with patches provided the most stable potentials.

Individual anodic and cathodic overpotentials (activation, ohmic, concentration and mass transport) were obtained in a segmented and un-segmented fuel cell for the first time. An array of reference electrodes and gases with different diffusion coefficients were used to discern the different overpotentials. The results show that the anodic overpotentials cannot be ignored, even if the conditions are changed at the cathode only. The oxygen concentration has an effect on the anode and in particular hydrogen oxidation and proton flux.

Under dry conditions the current in-plane gradients are very large and the heat generation profiles are affected, creating an uneven temperature distribution in the catalyst layer due to concurrent effects of the half-cell reactions and the water vaporization.

The combination of reference electrodes and multi-component gas analysis, allows the measurement and calculation of kinetic and diffusion parameters that can be used for modeling and to understand the behavior of different layers of a fuel cell.

PREFACE

The literature review, experimental design, performing of experiments, data analysis was done by O.E. Herrera under the supervision of Dr. Walter Mérida-Donis and Dr. David P. Wilkinson. The initial and final drafts of all manuscripts were prepared by O.E. Herrera with revisions edited and approved by Dr. Mérida and Dr. Wilkinson.

A version of Chapter 5 has been published. Herrera, O., W. Mérida, and D.P. Wilkinson, *Sensing electrodes for failure diagnostics in fuel cells*. Journal of Power Sources, 2009. 190(1): p. 103-109.

A version of Chapter 6 has been published. Herrera, O.E., W. Merida, and D.P. Wilkinson, *New Reference Electrode Approach for Fuel Cell Performance Evaluation*. ECS Transactions, 2008. **16**(2): p. 1915-1926.

A version of Chapter 7 has been submitted for publication. Herrera, O.E., W. Merida, and D.P. Wilkinson, *Anode and cathode overpotentials and heat profiles in PEMFC*.

TABLE OF CONTENTS

Abstract	ii
Preface	iii
Table of Contents	iv
List of Tables	vii
List of Figures	viii
List of Symbols	xiv
Acknowledgements	xvii
Dedication	xviii
1 Introduction	1
1.1 FUEL CELL HISTORY	1
1.2 ELECTROCHEMISTRY PRINCIPLES	3
1.2.1 <i>Effect of concentration</i>	5
1.2.2 <i>Effect of temperature</i>	5
1.2.3 <i>Effect of pressure</i>	6
1.2.4 <i>Electrochemical cell potential</i>	6
1.3 FUEL CELLS.....	7
1.4 PROTON EXCHANGE MEMBRANE FUEL CELLS	8
1.5 PEMFC CELL REAL POTENTIAL.....	10
1.6 WATER IN PEMFC.....	14
1.7 FAILURE MODES.....	22
1.7.1 <i>Starvation or low stoichiometric ratio</i>	24
1.7.2 <i>Dehydration</i>	26
1.7.3 <i>Flooding</i>	27
1.8 REFERENCE ELECTRODES	29
2 Research Objectives	36
3 Thesis Layout	37
4 Experimental	41

4.1	FUEL CELL AND MEASUREMENTS.....	41
4.1.1	<i>Operating conditions</i>	43
4.1.2	<i>Segmented cell measurements</i>	44
4.2	SENSING AND REFERENCE ELECTRODES IN FUEL CELL.....	47
4.2.1	<i>Reference electrode potential correction</i>	50
4.2.2	<i>High frequency resistance measurements</i>	51
5	Sensing Electrodes for Failure Diagnostics in Fuel Cells	52
5.1	INTRODUCTION	52
5.2	RESULTS AND DISCUSSION	52
5.3	SUMMARY	65
6	New Reference Electrode Approach for Fuel Cell Performance Evaluation	66
6.1	INTRODUCTION	66
6.2	RESULTS AND DISCUSSION.....	66
6.3	SUMMARY	73
7	Anode and Cathode Overpotentials and Heat Profiles on a PEMFC	74
7.1	INTRODUCTION	74
7.2	RESULTS AND DISCUSSION	75
7.2.1	<i>Fuel Cell Overpotentials</i>	75
7.2.2	<i>Overpotential Distribution</i>	84
7.3	SUMMARY	90
8	Conclusions	92
9	Future Work and Recommendations	95
	Bibliography	98
A.1	FUEL CELL AND TEST STATION ASSEMBLY FOR TESTING.....	109
A.2	FUEL CELL TESTING PROCEDURES	113
A.2.1	<i>Conditioning of MEA</i>	113
A.2.2	<i>Polarization Curves</i>	114
A.3	CALCULATIONS.....	116
A.3.1	<i>Enthalpy from Bond Dissociation Energies</i>	116

A.3.2	<i>Tafel Plot Calculations</i>	117
A.3.3	<i>Overpotential calculations</i>	118
A.4	SEGMENTED CELL	119
A.5	DUPONT™ NAFION® PFSA MEMBRANES	125

LIST OF TABLES

Table 1-1 Some reported water drag coefficients (ω) for Nafion [®] [35].....	21
Table 1-2 Operating failure modes measurement summary.	23
Table 4-1 Membrane Electrode Assembly and flow-field details	42
Table 4-2 Operating conditions for normal, flooding and dry experiments. The stoichiometric flows, the inlet pressure, the temperature of the cell and the dry gases (oxygen, heliox, air and hydrogen) were maintained constant.....	44
Table 4-3 Nomenclature for potential connections of electrodes	49
Table 7-1 Measured values for the potential losses obtained from Figure 7-1 and their values at a current density of 1 Acm^{-2} . $I_x = 2.8 \text{ mAcm}^{-2}$ at 2.04 atm, 298 K, and a fully humidified membrane.	75
Table 7-2 Tafel kinetic parameters for the anode and cathode for different conditions. The exchange current densities were corrected for the partial pressure of oxygen as described in Chapter 1.....	80
Table 7-3 Diffusion coefficient for water in the respective gases and thermal conductivity of air, helium and nitrogen.	81
Table 7-4 Pressure drop values at the inlet and outlet of the fuel cell for all gases and conditions at 800 mAcm^{-2}	82
Table A-1 Bond dissociation energies of molecules from the National Institute of Standards and Technology [189].	116
Table A-2 Measured potential and high frequency resistance values at 1 Acm^{-2}	118

LIST OF FIGURES

Figure 1-1 Grove's gaseous voltaic battery (1842).....	2
Figure 1-2 Fuel Cell classifications.....	7
Figure 1-3 Basic components of a PEMFC (Proton Exchange Membrane Fuel Cell). In this case, the fuel used is hydrogen (white) and the oxidant is oxygen (red). ..	8
Figure 1-4 Polarization curve and losses in a PEMFC (Adapted from results in Chapter 7: Anode and cathode overpotentials and heat profiles on a PEMFC).....	12
Figure 1-5 Conductivity of perfluorosulfonated membranes, such as Nafion®, as a function of relative humidity. Adapted from reference [29] with permission.	15
Figure 1-6 Chemical structure of Nafion. Typically $x=6-10$ and $y=1$. For the 3d structure, the values chosen were $x=7$ and $y=1$	16
Figure 1-7 Membrane conductivity as a function of water content. From reference [39] with permission.	17
Figure 1-8 Some of the most important water mechanisms in a PEMFC. Here, the fuel (hydrogen in white) and the oxidant (oxygen in red) are humidified. The active sulfonic sites (sulfur in yellow) of the persulfonated membrane carry protons as ions and water charged molecules. The transport through the GDL and the two phase flow are omitted.	19
Figure 1-9 A graph of relative humidity versus temperature for the exit air of a PEMFC with air stoichiometry of 2 and 4. From reference [61] with permission.	22
Figure 1-10 Voltage drop due to dehydration.	26
Figure 1-11 Voltage drop after RH is increased above 100% (from DPT = 75 °C to DPT = 95 °C). The cell and gas temperatures are maintained constant at 75 °C.	28
Figure 1-12 Measurement of an electrode potential with a reference electrode. The tube joining the reference electrode with the working electrode is called a Luggin capillary. It helps to reduce the inclusion of iR drop in the measurement.	30
Figure 1-13 Three-electrode system required to measure electrode overpotentials, i.e., $\Delta E - \Delta E_e$. The potential between the working electrode and the reference electrode when both ΔE and ΔE_e correspond to the same reaction is equal to the overpotential η . The Luggin capillary reduces the distance between the RE and the WE and thus, reduces the iR drop.	31

Figure 1-14 Effects to the potential profiles of the misalignment of the anode and cathode electrodes in a solid electrolyte. The figures were modeled with Comsol Multiphysics® software.....	33
Figure 1-15 General electric connection and placement of reference electrodes in a fuel cell.....	34
Figure 3-1 Thesis layout	37
Figure 3-2 Effect on the potential of uneven membrane resistance. The conductivity is homogenous in (a) and it decreases from bottom to top in (b). The figures were modeled with Comsol Multiphysics® software.	38
Figure 4-1 (a) Diagram of research fuel cell components (b) Picture of research fuel cell, with components identified: (A) current collectors, (B) gas ports, (C) thermocouple ports, (D) bipolar plates, (E) ports for the water coolant, and (F) coolant plates.	41
Figure 4-2 Pressure drop of fuel cell with Ion-Power MEA's at different flow rates (anode: pure hydrogen and cathode: air) and the equivalent current densities.	43
Figure 4-3 Location of the current collectors and thermistors of the PCB with respect to the flow fields.	45
Figure 4-4 PCB with the current collectors (a), thermistors (b), resistors (c), and contact for the reference electrodes (d) for the segmented cathode plate.....	46
Figure 4-5 Placing of reference and sensing electrodes in isolated chambers.	48
Figure 4-6 Potential connections of electrodes	49
Figure 4-7 Reference electrode HFR measurements from node A to B and node B and P. The drawing is not to scale, but the potential line calculations remain constant up to the reference electrode as can be seen.	51
Figure 5-1 Stability of sensing electrodes in a fully humidified fuel cell at different current densities for more than 10 hours.	53
Figure 5-2 Potential responses and standard deviation of $SE_{F,in}$ and $SE_{F,out}$ at different conditions: normal (i), dehydration (ii), and flooding (iii).	54

Figure 5-3 General treatment of the data obtained with SEs. The average and standard deviation of the data for at least 15 minutes per point was calculated. Also, the potential difference between SE_{in} and SE_{out}, on the cathode, is shown. .55

Figure 5-4 Potential response of SE_{in} and SE_{out} at different RH at a current density of 500 mAcm⁻². The RH is gradually reduced to a minimum of 5 % and then back to 100 %. Each point is an average over 30 minutes.....57

Figure 5-5 Potential response SE_{in} vs. SE_{out} during flooding conditions at a current density of 500 mAcm⁻². The pressure differences between the inlet and the outlet of both the anode and the cathode confirm the potential response results. Each point is an average of 30 minutes.58

Figure 5-6 Potential response of SE_{in} vs. E_{out} to gradual reduction of fuel stoichiometry at a current density of 500 mAcm⁻². This potential difference shows an earlier response than the fuel cell. Each point is an average of 30 minutes.59

Figure 5-7 Characteristic response under simulated low fuel stoichiometry (i), drying (ii) and flooding (iii) at a current density of 500 mAcm⁻². Time 0 is when the undesired conditions are detected by the SEs ($\nu=1.15$, RH < 60 %, and dew point temperature 5° higher than the cell temperature). The fuel cell potential shows little variation while the potential difference between SE_{in} and SE_{out} is changing.61

Figure 5-8 Early potential response of sensing electrodes to flooding conditions. Time 0 is when the undesired conditions are detected by the SEs (dew point temperature 5° higher than the cell temperature). The fuel cell potential shows little variation while the potential difference between SE_{in} and SE_{out} is changing. The standard deviations of the different experimental runs show good response and reproducibility of the sensing electrodes.62

Figure 5-9 Early potential response of the sensing electrodes to drying conditions. Time 0 is when the undesired conditions are detected by the SEs (RH < 60). The fuel cell potential shows little variation while the potential difference between SE_{in} and SE_{out} is changing. The standard deviations of the different experimental runs show good response and reproducibility of the sensing electrodes.63

Figure 5-10 Early potential response of the sensing electrodes to low stoichiometric flows. Time 0 is when the undesired conditions are detected by the SEs ($v=1.15$). The fuel cell potential shows little variation while the potential difference between SE_{in} and SE_{out} is changing. The standard deviations of the different experimental runs show good response and reproducibility of the sensing electrodes.64

Figure 6-1 Stability of sensing electrodes at different humidity conditions and the reference electrodes at constant conditions.....67

Figure 6-2 Anodic, cathodic and fuel cell potentials at different humidity conditions and current densities.68

Figure 6-3 Effects of dehydration over the different electrodes. RH was reduced to 4% and then increased to 100% at a constant current of 500 mAcm^{-2}69

Figure 6-4 Reference electrode and sensing electrode response to flooding conditions at 1000 mAcm^{-2} . The DPT was increased from 348 K to 368 K, increasing the potential oscillations of the sensing electrodes.70

Figure 6-5 Potential response of the anode, cathode, fuel cell and the sensing electrodes ($SE_{O,out}$, $SE_{O,in}$) to low oxidant stoichiometry at 500 mAcm^{-2} : (i) oxidant stoichiometry as a function of time, (ii) voltage response as a function of time, (iii) voltage response at each stoichiometric point, and (iv) potential difference between stoichiometry at normal conditions ($v_c = 2$) and different stoichiometric values.71

Figure 6-6 Potential response of the anode, cathode, fuel cell and the sensing electrode ($SE_{F,out}$) to low oxidant stoichiometry at 500 mAcm^{-2} : (i) voltage response at each stoichiometric point, and (ii) potential difference between stoichiometry at normal conditions ($v_a = 1.5$) and different stoichiometric values.....72

Figure 7-1 Measured anodic and cathodic losses obtained from using different gases with different diffusion coefficients in the cathode and the ohmic losses obtained from high frequency impedance measurements.76

Figure 7-2 (i) Polarization curves for all humidity conditions (Cathode: Air). (ii) Cathode overpotential divided by the total overpotential. (iii) The anode overpotential

	divided by the total overpotential. In (ii) and (iii), the red line shows the cathode and anode behaviour during normal conditions, respectively.	78
Figure 7-3	Anodic and cathodic overpotentials of dry and flooding conditions normalized against normal conditions (baseline). η/η_0 <i>MT</i> includes concentration losses for dry conditions as heliox dries the cell faster and the potential response is lower than the potential response when using air.	79
Figure 7-4	Average ohmic resistances (stacked) and temperature averages (white open circles) for anode and cathode during normal, flooding, and dry conditions for the air and oxygen. Only normal and flooding conditions are presented for heliox.	84
Figure 7-5	Current distribution of air/H ₂ for different operating conditions (a) 100 % RH (b) 50 % RH and (c) 0 % RH. The current was kept constant at 25 A (522 mAcm ⁻²). Segment 1-1 and segment 4-4 are the segments where the inlet and outlet are located, respectively.	86
Figure 7-6	Fuel cell's energy profiles. The gray area is the heat of vaporization in the cathode, which consumes energy from the heat of reaction of the cathode.	88
Figure 7-7	In-plane power generation from heat for the cathode (top) and anode (bottom) catalyst layers for 100 % RH (i) and under dry conditions (ii). No heat of evaporation is considered for the 100% RH case. The values were calculated using the current distributions and the overpotential values and then interpolated to create a continuous function.	89
Figure 9-1	Nafion [®] coated platinized platinum wire located in catalyst coated membrane and half-cell patch located in a catalyst coated membrane to use as a sensing electrode.	95
Figure A-1	Fuel Cell in cross-flow configuration	109
Figure A-2	Fuel Cell plates for cross-flow configuration.....	110
Figure A-3	Fuel Cell in co-flow configuration with reference electrodes and segmentation on the cathode.	111
Figure A-4	Test station components	112
Figure A-5	Current density set points for polarization curve.....	115

Figure A-6 Tafel plots for the anodic and cathodic branches of the current-overpotential curve for $H_2 + 1/2O_2 \rightleftharpoons H_2O$, the fuel cell reaction evaluated in this thesis. The Tafel plot shown is the calculated from the results obtained during normal conditions.	118
Figure A-7 Segmented fuel cell graphite plate.....	119
Figure A-8 Diagram for the machining of segmented graphite plates.	120
Figure A-9 Segmented current collector diagram.....	121
Figure A-10 Segmented cell current collector PCB detailed diagram	122

LIST OF SYMBOLS

Symbol	Meaning	Units, value or comments
A	Area	cm ²
a	Activity	
A _{Pt,elec}	Mass-specific surface area of supported Pt	m ² Ptg ⁻¹
b	Tafel slope	
C	Concentration	
DPT	Dew point temperature	K / °C
E	Potential/Electromotive Force	V
EIS	Electrochemical Impedance Spectroscopy	Ohm
F	Faraday's constant	96485 Cmol ⁻¹
FF	Flow-field	
G	Gibbs Free Energy	J
GDE	Gas diffusion electrode	
GST	Gas standard temperature	K / °C
H	Enthalpy	J
i	Current density	Acm ⁻²
L	Electrode areal loading of supported Pt	mgPtcm ⁻²
MEA	Membrane Electrode Assembly	
MRI	Magnetic Resonance Imaging	
m	Number of moles	mol
n	Molar flow rate	mols ⁻¹
N	Molar flux	molm ⁻² s ⁻¹
p	Partial pressure	Atm
PEMFC	Proton Exchange Membrane Fuel Cell	
PTFE	Polytetrafluoroethylene	
Q	Electric charge	C
\dot{Q}	Volumetric flow rate	Ls ⁻¹
\hat{r}	Orthogonal vector to the area through which water is diffusing.	
R	Resistance	Ωcm ²
R _g	Gas constant	96 485 Cmol ⁻¹
RE	Reference electrode	
RH	Relative humidity	%

Symbol	Meaning	Units, value or comments
RHE	Reversible Hydrogen Electrode	
S	Entropy	JK^{-1}
s	Stoichiometric coefficient	
SE	Sensing electrode	
SFi	Sensing electrode Fuel inlet	
SFo	Sensing electrode Fuel outlet	
SHE	Standard Hydrogen Electrode	
SLPM	Standard liters per minute	Lmin^{-1}
SOi	Sensing electrode Oxidant inlet	
SOo	Sensing electrode Oxidant outlet	
T	Temperature	$\text{K} / ^\circ\text{C}$
t	Time	S
w	Antoine's equation constant	
WE	Working electrode	
x	Antoine's equation constant	
y	Antoine's equation constant	
z	Number of electrons	
α	Transfer coefficient	
Δ	Change	
η	Overpotential	V
κ	Thermal conductivity	$\text{mWm}^{-1}\text{K}^{-1}$
λ	Water content in membrane	Number of water molecules per sulfonic acid group in the membrane
μ	Potential	V
v	Stoichiometric ratio	
σ	Standard deviation	
ϕ	Volumetric content of dry gas	
ω	Electro-osmotic drag coefficient	

Subscripts

Symbol	Meaning
0	Exchange
a	Anode
Act	Activation
c	Cathode
d	Diffusion
e	Equilibrium
eff	Effective
EOD	Electro-osmotic drag
F	Fuel
H ⁺	Protonic
in	Inlet
m	Membrane
O	Oxidant
out	Outlet
Ox	Oxidized
P	Patch
r	Reaction
Red	Reduced
T	Temperature
W	Water
Ω	Ohmic

Superscripts

Symbol	Meaning
o	Standard conditions

ACKNOWLEDGEMENTS

It took a few years and at least two guiding lights to complete this thesis. First and foremost, I have to thank my supervisor and friend Dr. Walter Mérida that showed me how to enjoy life as a researcher and how to be the best that I can be. Secondly, Dr. David Wilkinson that through numerous corrections and discussions took my work and thesis where it is now.

Special thanks to Elöd Gyenge for taking the time for reviewing the work and the thesis as a committee member.

All these past years wouldn't have been the same without all my great friends and colleagues; especially: Mauricio Blanco, Alfred Lam, David Bruce and Jonathan Martin. Thanks for being there whenever I needed you!

Thanks to my family that brought “un cachito de México” every time they were around or every time that they called...Without their encouragement I just wouldn't be me... Gracias Chavez! Gracias Herrera!

I just couldn't be here without Claudia... Gracias!

I would also like to thank the “Consejo Nacional de Ciencia y Tecnología” (Science and Technology National Council of Mexico, CONACYT) and the National Sciences and Engineering Research Council of Canada (NSERC) for the financial support to this work and the projects associated with it.

DEDICATION

A Claudia

1 INTRODUCTION

1.1 FUEL CELL HISTORY

A Swiss Professor named Christian Friedrich Schönbein presented in the late summer of 1838 what Bossel later called the “fuel cell effect” [1]. The experiment consisted of two platinum electrodes in diluted sulphuric acid; these experiments led to the discovery of ozone. He saw that when applying a potential, bubbles were produced with a distinctive smell that’s why he named it after the Greek word: οζειν (I smell) [2]. He also noticed that when he wasn’t applying a potential a small current was produced. The next year in 1839, he published his findings in a paper in the January issue of the Philosophical Magazine. The concluding remarks of his paper were: “...*we are entitled to assert that the current in question is caused by the combination of hydrogen with oxygen (contained dissolved in water) and not by the conduct*” [3]. Schönbein corresponded with numerous authorities of the time, from Berzelius to Faraday to Sir William Grove, who was the patent officer for the cotton powder of Schönbein (an explosive made with cotton and nitric acid).

Sir William Grove sent a letter in 1838 to the editor of the Philosophical Magazine that was later published in 1839, where he described the same effect, but in more depth and stating that he was going to repeat the experiments in series. He then published what could be called his first paper of a working fuel cell: “On a Gaseous Voltaic Battery” [4]. A diagram of his experiment is shown in Figure 1-1. According to Bossel, it was not until 1845 when he described a complete fuel cell electricity generator that included the generation of hydrogen from zinc and sulphuric acid [5].

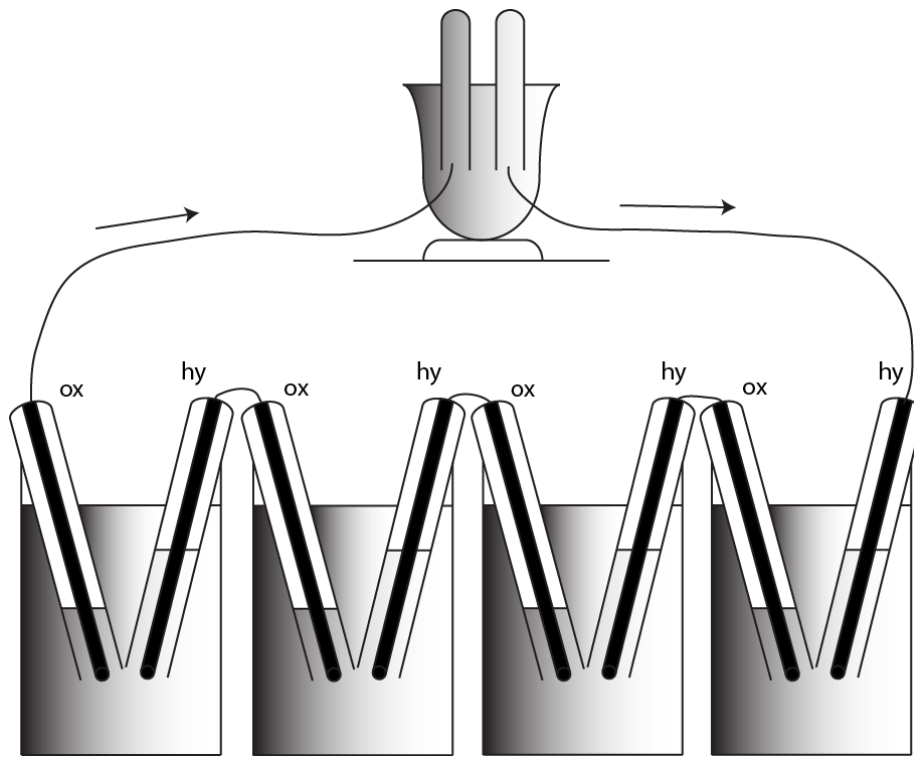


Figure 1-1 Grove's gaseous voltaic battery (1842).

Grove kept improving his work up to the point where he was able to use coal as a fuel. From then on there were several breakthroughs in electrochemical knowledge and fuel cells in general. Some of the most important contributions were done by Ludwig Mond and Charles Langer with 15 published papers after Grove. In 1889, they discovered that they had to increase the surface of the triple contact (three-phase region: electrode, electrolyte and gas) [6]. They introduced the name fuel cell. According to Appleby, the fuel cells that they used are very similar to the phosphoric acid fuel cells of today [7]. Contributions from Ostwald, Nernst, Jacques, Baur, Schmid, Berl, Niederreither, and Bacon, who is considered the most successful fuel cell pioneer [3] improved the understanding of fuel cells and electrochemistry. In the 1960's the first proton exchange membrane was developed at General Electric, through the work of Thomas Grubb and Leonard Niedrach for the US Navy and later for the Gemini spacecraft [8]. Since then, there were several more advances in different types of fuel cells and different countries in the world that led to the fuel cells that we know today.

1.2 ELECTROCHEMISTRY PRINCIPLES

In order to understand fuel cells, it is necessary to understand the basic principles of electrochemistry. Electrochemistry is the science that is concerned with the study of the interface between an electronic and an ionic conductor, and traditionally concentrates on:

- i. The nature of the ionic conductor, an aqueous (or more rarely) a non-aqueous solution, polymer or superionic solid containing mobile ions;
- ii. the structure of the electrified interface that forms on immersion of an electronic conductor into an ionic conductor;
- iii. the electron-transfer processes that can take place at this interface, and the limitations on the rates of such processes [9].

An ionic conductor is also called an electrolyte. The ions can be induced to move by an electrical force. This electric field can be generated by introducing two electronic conductors and applying a potential difference. These electronic conductors are named electrodes.

When current flows in the cell, the negative charged ions (anions) move towards the anode (where oxidation occurs) and the positive charged ions (cations) move towards the cathode (where reduction occurs), as shown in equation (1-1).



where $s_{Ox,j}$ is the stoichiometric coefficient of oxidized species (Ox_j) and $s_{Red,j}$ is the stoichiometric coefficient of the reduced species (Red_j). The stoichiometric number provides the relationship among changes in mole numbers of the chemical species which occur as a result of the chemical reaction [10].

The reaction consumes or produces energy. The enthalpy (H) is a measurement of the total energy in the system [10]. It can be defined as the internal energy of the system (U) plus the amount of work needed to push against the ambient pressure (PV), as shown in equation . The values for a specific reaction can be calculated from tabulated enthalpies

of formation or the bond energy of dissociation that are associated to specific conditions of activity, pressure and temperature [10, 11]. The standard values are measured at a reference state of 298 K, 1 atm and an activity of 1 for all species present.

$$H = U + PV \quad (1-2)$$

From the enthalpy of the system (H), there is only a certain amount that can be converted to work; the rest is released as heat associated with the entropy change (ΔS). This usable energy is defined as the Gibbs free energy (G), as shown in equation (1-3).

$$G = H - T\Delta S \quad (1-3)$$

The change of Gibbs energy of reaction is the difference between the Gibbs energy of the reduced species and the Gibbs energy of the oxidized species:

$$\Delta G_{a/c}^0 = \sum_j s_{Red,j} G_{Red,j}^0 - \sum_j s_{Ox,j} G_{Ox,j}^0 \quad (1-4)$$

If the change of free energy per species is considered, the chemical potential of the species (μ_j) is used, i.e., $\mu_j = \frac{G_j}{m_j}$. When a reaction deviates from the standard conditions, the chemical potential is equal to the standard chemical potential (μ_j^0) plus the effect of the activity, as shown in equation (1-5).

$$\mu_j = \mu_j^0 + RT \ln a_j \quad (1-5)$$

The activity represents the effective concentration of the species. It is a dimensionless quantity and can be substituted with the following conventions [12, 13]:

1. Ideal solution assumption (i.e., dilute electrolytes): The activity of soluble species can be assumed to be equivalent to the molar concentration (M, molL⁻¹) divided by the molar concentration at standard conditions (1 molL⁻¹).
2. For substances in excess (e.g., solids, liquid H₂O): $a = 1$
3. Ideal gas assumption: The activity of the gas is equivalent to its partial pressure (atm) divided by the pressure at standard conditions (1 bar = 0.986 atm = 100 kPa).

- a. Ideal gas mixtures $p = y \frac{P}{p^0}$; where y is the mole fraction of the gas in the mixture, P is total pressure and P^0 is the standard pressure (1 atm).

1.2.1 Effect of concentration

For a given chemical reaction, the van't Hoff isotherm expresses the change of free energy in terms of the reaction, the temperature, and the activities (a), as shown in equation (1-6). The activities of the initial states (reactants) are taken as negative and final states (products) are positive.

$$\Delta G = \Delta G^0 + RT \ln \left(\frac{\prod a_{products}}{\prod a_{reactants}} \right) \quad (1-6)$$

1.2.2 Effect of temperature

The Gibbs free energy can be written as:

$$dG = VdP - SdT \quad (1-7)$$

where V is the volume, P is the pressure, S is the entropy and T is the temperature. By taking its partial derivative with respect to temperature and keeping the pressure constant, we obtain

$$\left(\frac{\delta G}{\delta T} \right)_P = -S \quad (1-8)$$

It can also be written as the change between two states:

$$\left(\frac{\delta \Delta G}{\delta T} \right)_P = -\Delta S \quad (1-9)$$

that integrated over the temperature range

$$\Delta G = \Delta G^0 - \int \Delta S dT \quad (1-10)$$

1.2.3 Effect of pressure

The pressure effects can also be solved by maintaining the temperature constant to obtain

$$\left(\frac{\delta\Delta G}{\delta P}\right)_T = \Delta V \quad (1-11)$$

If ideal gas behaviour is assumed,

$$\Delta V_g = \frac{\Delta nRT}{P} \quad (1-12)$$

Substituting equation (1-12) in equation (1-11) and integrating between P_1 and P_2 , we obtain:

$$\Delta G_{P_2} = \Delta G_{P_1} - \frac{\Delta nRgT}{zF} \ln\left(\frac{P_2}{P_1}\right) \quad (1-13)$$

1.2.4 Electrochemical cell potential

Electrical energy is defined as the product of the electromotive force (E) by the charge transferred (Q). Therefore, the Gibbs free energy of an electrochemical reaction can be expressed with the following equation:

$$\Delta G^0 = -QE = -zFE^0 \quad (1-14)$$

where z is the number of electrons involved in the reaction and F is Faraday's constant. The cell potential is the ideal maximum voltage at a reference state and can also be expressed as the difference between the anodic and cathodic potentials.

$$E^0 = E_c^0 - E_a^0 \quad (1-15)$$

Substituting equation (1-15) in equation (1-14) gives the Nernst equation.

$$E_e = E^0 - \frac{RgT}{zF} \ln \frac{\prod a_{Red}^{SRed}}{\prod a_{Ox}^{SOx}} \quad (1-16)$$

The Nernst equation defines the equilibrium potential (E_e). The equilibrium potential is the potential where the forward and reverse reaction rates are equal in an electrolyte.

1.3 FUEL CELLS

Fuel cells are electrochemical devices that transform chemical energy into electrical energy. Fuel cells can use a variety of fuels: from hydrogen to coal [14, 15]. They can produce electricity with high efficiency and low emissions. There are different types of fuel cells that can be classified according to their operating temperature and to the electrolyte that they use. The electrolyte is the ionic conductor. The main types are displayed on Figure 1-2.

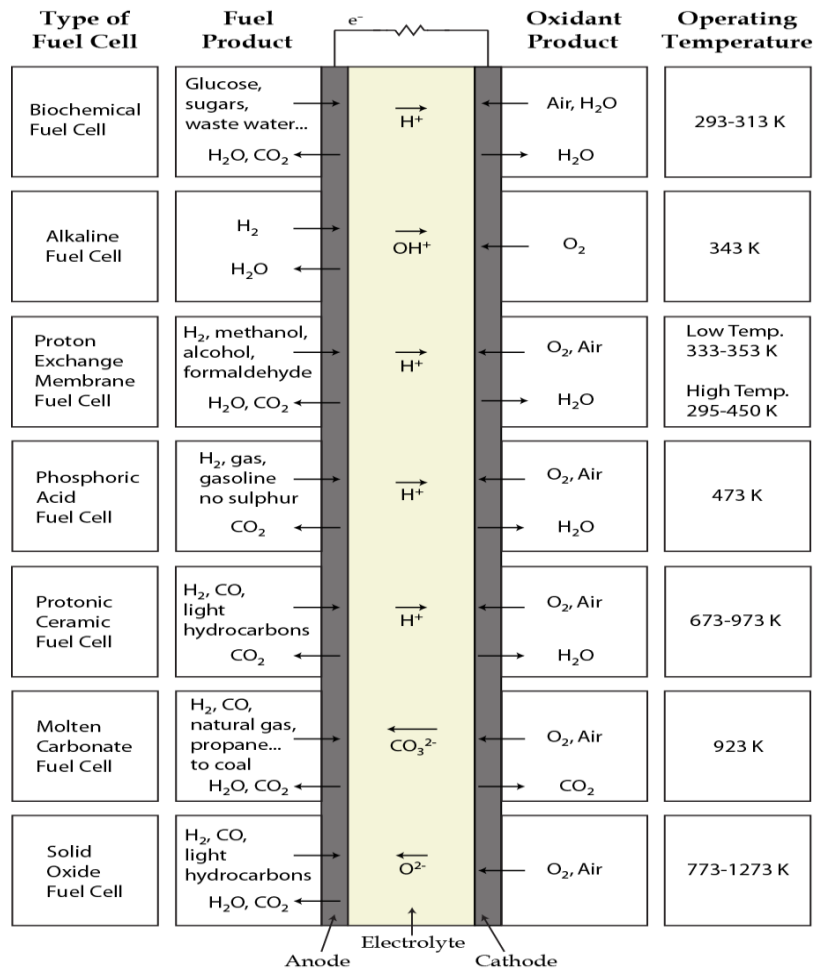


Figure 1-2 Fuel Cell classifications

1.4 PROTON EXCHANGE MEMBRANE FUEL CELLS

The main focus of the present work is low temperature ($<100\text{ }^{\circ}\text{C}$) Proton Exchange Membrane Fuel Cells (PEMFC) that use a proton conductive membrane as the electrolyte.

In a PEMFC, the gases flow to a flow-field where they diffuse through the gas diffusion layer (GDL), then usually to a microporous layer (MPL). Both of these layers enhance the gas diffusion to the catalyst layers, maintaining the membrane moist, while removing the excess water as shown in Figure 1-3.

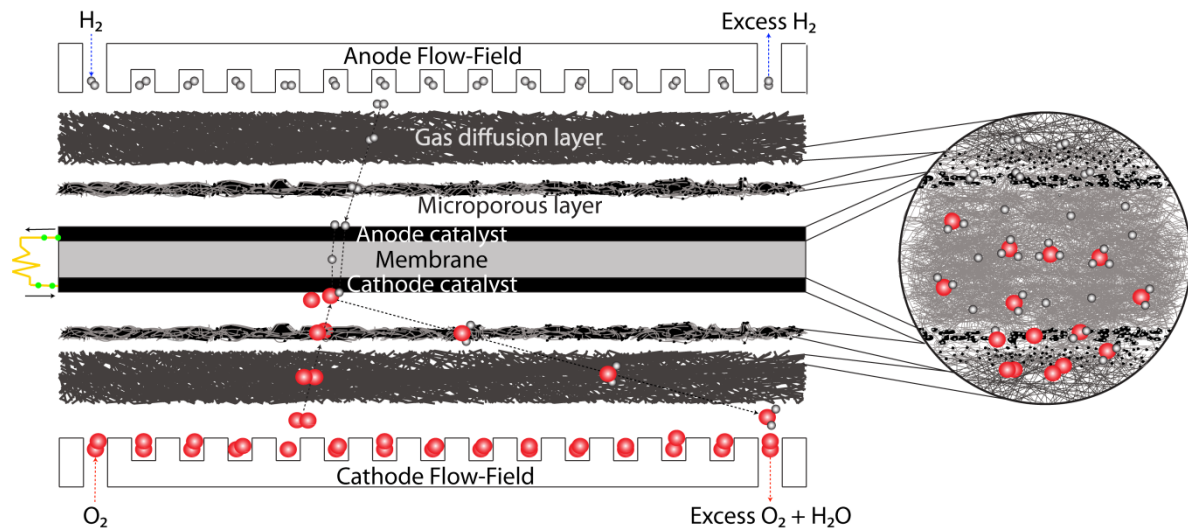


Figure 1-3 Basic components of a PEMFC (Proton Exchange Membrane Fuel Cell). In this case, the fuel used is hydrogen (white) and the oxidant is oxygen (red).

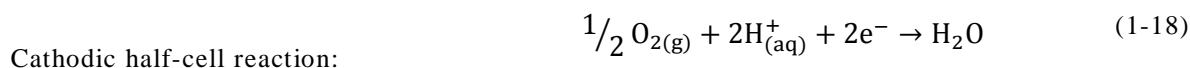
Half of the reaction occurs on the anode catalyst and the other half occurs on the cathode catalyst. In order for these half-cell reactions to occur a three-phase boundary (where the catalyst, gas, and electrolyte meet) is needed. The reactions for a low temperature PEMFC working with pure hydrogen and oxygen are shown below. The half-cell reaction enthalpy and Gibbs free energy can be calculated based on the bond energy or bond dissociation enthalpy. The bond energy is the energy required to break a given type of bond between atoms in certain valence states. An averaged bond energy is commonly derived by dissecting the heat of atomization of a molecule into contributions of individual bonds. For molecules with localized bonds, the heats of atomization

(formation) are usually well approximated by the sum of pertinent averaged bond energies [13]. If this concept is applied to the reactants and products of a reaction, it should be clear that a common atomization state exists, and that the total bond energies of the reactants compared with the bond energies of the products determines the enthalpy change of reaction. Thus, if the products have greater total bond energy than the reactants the reaction will be exothermic, and the opposite is true for an endothermic reaction. However, for the common covalent bonds found in polyatomic molecules (e.g., C-H and C-C) these are average dissociation enthalpies, in contrast to specific bond dissociation enthalpies determined for individual bonds in designated compounds. Factors such as hybridization, strain and conjugation may raise or lower these numbers substantially



$$\Delta H^{\circ}_{\text{reaction}} = 435.93 \text{ kJmol}^{-1}$$

$$E^{\circ}_{\text{a}} = 0 \text{ V}$$



$$\Delta G^{\circ} = -237.16 \text{ kJmol}^{-1}$$

$$\Delta H^{\circ}_{\text{reaction}} = -721.76 \text{ kJmol}^{-1}$$

$$E^{\circ}_{\text{c}} = 1.23 \text{ V}$$



$$\Delta G^{\circ} = -237.16 \text{ kJmol}^{-1}$$

$$\Delta H^{\circ}_{\text{reaction}} = -285.83 \text{ kJmol}^{-1}$$

$$E^{\circ}_{\text{overall}} = 1.23 \text{ V}$$

Each one of the reactions has an enthalpy that defines the amount of energy being transformed by the reaction (an exothermic reaction is negative and an endothermic reaction is positive). The half-cell reaction enthalpies were calculated with the bond

dissociation energy of each one of the chemical bonds of the molecules as described in Appendix A.3. They can be added to represent the overall electrochemical cell reaction, as shown in equation (1-19). From that energy, there is only a certain amount that can be converted to work (ΔG) the rest is released as heat associated with the entropy change (ΔS). Therefore, the maximum thermodynamic efficiency for an isothermal fuel cell is the negative of the change of the Gibbs free energy (maximum electric work) divided by the change of the enthalpy, as shown in equation(1-20)[16].

$$Efficiency = \frac{\Delta G}{\Delta H} = \frac{zFE}{zFE + T\Delta S} \quad (1-20)$$

where E is the cell potential, z is the number of electrons involved in the reaction, F is Faraday's constant, T is the temperature of operation, and ΔS is the entropy change. This efficiency is only valid when no losses are considered. The real electrochemical potential needs to be measured to calculate the real efficiency.

1.5 PEMFC CELL REAL POTENTIAL

The equilibrium potential of a fuel cell can be predicted by the Nernst equation (1-15). For a PEMFC running with pure hydrogen and oxygen, the equation becomes

$$E_e = E^0 - \frac{RgT}{nF} \ln \frac{[H_2O]}{[H_2][O_2]^{1/2}} = E^0 - \frac{RgT}{nF} \ln \frac{1}{[H_2][O_2]^{1/2}} \quad (1-21)$$

where $[H_2]$ is the molar concentration of hydrogen and $[O_2]$ is the molar concentration of oxygen in the system. If air is used, the equation becomes

$$E_e = E^0 - \frac{RgT}{nF} \ln \frac{1}{[H_2][0.21O_2]^{1/2}} \quad (1-22)$$

The real cell potential is not the same as the equilibrium potential. The deviations from the ideal equilibrium potential are called overpotentials (η), and they reduce the useful cell voltage. The overpotentials are commonly classified into four main categories: activation (η_{Act}), ohmic (E_Ω), diffusion (η_d), and crossover [17], as shown in equation (1-22) and Figure 1-4. There are several different models that describe the behaviour of

the fuel cell potential that are based on the overpotential losses, but they use empirically obtained constants to fit their data [18-25]. Anodic overpotentials are usually neglected, unless the fuel is other than pure hydrogen. Therefore, for the purposes of this thesis, the complete mathematical model (separating the anode and cathode overpotentials) was used to interpret the results obtained.

$$E_{cell} = E_e - \eta_{Act,a} + \eta_{Act,c} - \eta_{d,a} + \eta_{d,c} - E_{\Omega(cathode,anode \& membrane)} = E_e - \sum \eta \quad (1-23)$$

For PEMFC operation the current density ideally needs to take into account and be corrected for fuel and oxidant crossover. Crossover refers to gases passing through the electrolyte and reacting on the other side, creating parasitic current losses. The hydrogen crossover is the most common one, ranging from 0.12 to 7.8 mAcm⁻² parasitic loss, depending on the membrane thickness, temperature, pressure and relative humidity (*RH*) [14, 26, 27]. The *RH* is a ratio between the partial pressure of water vapor in the gas and the saturated partial pressure of water at a given temperature. The effective current density (*i*) reported in this work is the sum of the measured current density (*i*^{*}) plus the crossover current density (*i*_x) as shown in equation (1-23).

$$i = i^* + i_x \quad (1-24)$$

where *i*_x = 2.8 mAcm⁻² (value obtained from voltammetric measurements at 2.04 atm, 298 K with a fully humidified membrane).

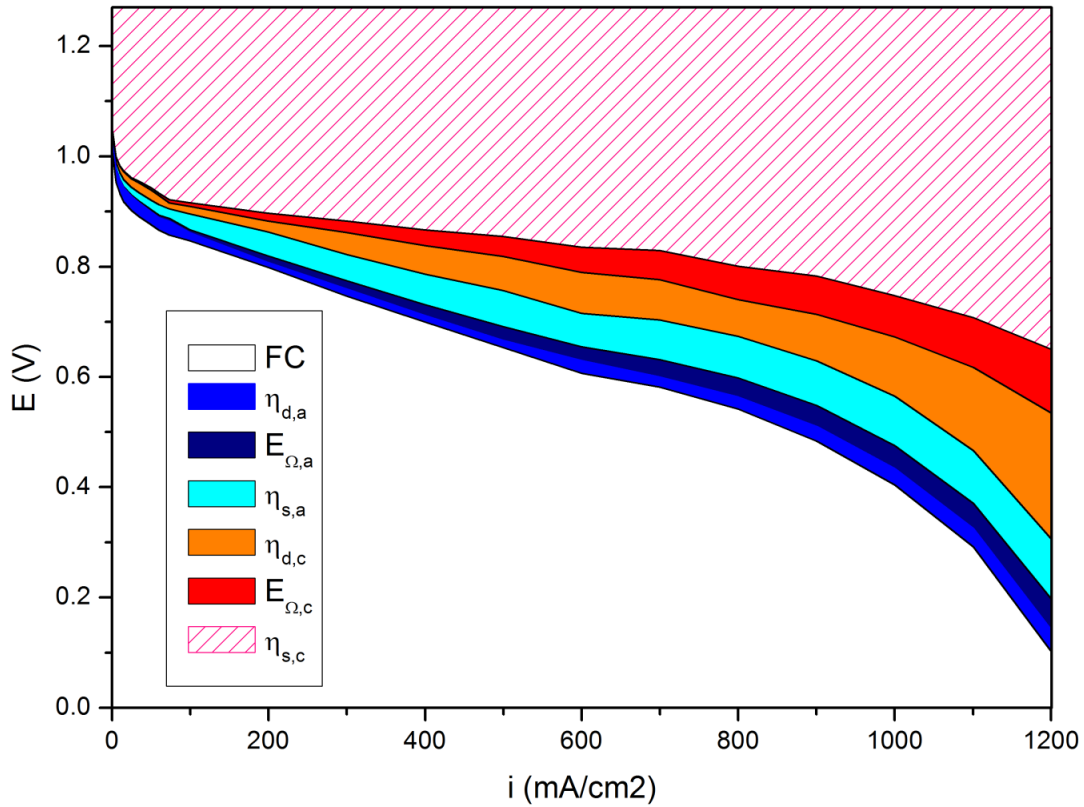


Figure 1-4 Polarization curve and losses in a PEMFC (Adapted from results in Chapter 7: Anode and cathode overpotentials and heat profiles on a PEMFC)

The ohmic losses are comprised of contact and overall bulk component resistances, with the membrane (function of the humidity) being one of the most important resistances. These losses can be mathematically described with equation (1-24).

$$E_{\Omega} = iR = i(R_a + R_c + R_m) + i(R_{electronic} + R_{contact}) \quad (1-25)$$

The contact and electronic resistances can be measured by using a graphite separator instead of the MEA. After correcting the ohmic potential for the electronic and contact resistances, the anode, cathode and membrane resistances can be isolated. Furthermore, the resistances can be isolated into the cathodic and anodic contributions through the use of a reference electrode as shown in equation 4. In this work, the membrane contribution was separated into anode's and cathode's.

$$E_{\Omega} = i(R_a + \alpha R_{membrane}) + i(R_c + \beta R_{membrane}) \quad (1-26)$$

where α and β as anodic and cathodic proportional factors ($\alpha + \beta = 1$). These resistances also include the ionomer ionic resistance for the anode and cathode, separately.

The activation loss or activation overpotential is mainly due to the cathodic oxygen reduction reaction. It can be described using the Butler-Erdey-Grúz-Volmer (BEV) equation (1-26). This equation relates the current density (i) to the overpotentials. The exchange current density (i_0) is the magnitude of the current density of both the anode and cathode at equilibrium. α_a and α_c are the anodic and cathodic transfer coefficients, respectively, that can be regarded as the fraction of change in the overpotential which leads to a change in the electron transfer rate.

$$i = i_0 \left\{ e^{\frac{\alpha_a n F}{RT} \eta_{Act,a}} - e^{\frac{\alpha_c n F}{RT} \eta_{Act,c}} \right\} \quad (1-27)$$

Assuming that one of the reactions is more dominant than the other one, the anodic and cathodic activation losses can be expressed by a Tafel approximation as follows:

$$\eta_{Act,a/c} = b_{a/c} \ln \frac{i}{i_{0,a/c}} \quad (1-28)$$

where $\eta_{a/c}$ is the dominant anodic or cathodic overpotential, $b_{a/c}$ is the anodic or cathodic Tafel slope and $i_{0,a/c}$ is the exchange current density for the anode or the cathode, respectively. The Tafel approximation is valid for current densities of less than 25 mAcm⁻² where the diffusion overpotentials are negligible. To be able to compare values from different sources, the cell potential needs to be corrected for iR losses and the characteristics of the catalyst layers need to be considered [14, 28], and equation (1-23) becomes:

$$E_{cell,iRcorrected} = E_e - b_a \ln \frac{i}{10L_a A_{Pt,elec} i_{0,a}(p_{H_2})} - b_c \ln \frac{i}{10L_c A_{Pt,elec} i_{0,c}(p_{O_2})} \quad (1-29)$$

where L is the electrode areal loading of supported Pt catalyst in mgPtcm⁻², $A_{Pt,elec}$ is the mass-specific surface area of supported Pt available for the reaction in m²Ptg⁻¹ Pt

(average of $75 \text{ m}^2\text{Ptg}^{-1}\text{Pt}$, from literature [14]), and i_0 is the exchange current density (a for anode and c for cathode) as a function of the partial pressure of oxygen for the cathode $i_{0,c}(p_{O_2})$. The anodic contribution to the cell voltage is not neglected because even at open circuit potential the anode contributes at least 5% of the total cell voltage under optimal conditions, more than the diffusion overpotentials at 1-2%. Typical values of the Tafel slope for the cathode range between 59 and 64 mVdec^{-1} and for the exchange current density ($i_{0,c}$) range between 0.8×10^{-9} and $8.7 \times 10^{-9} \text{ Acm}^{-2}$ [14].

The diffusion (transport or concentration) overpotential can be described after obtaining the effective current density (i) and the limiting current density (i_L) as shown in equation (1-30).

$$\eta_{d,a/c} = \frac{RT}{nF} \ln \left(1 - \frac{i}{i_L} \right) \quad (1-30)$$

In order to maintain all the overpotentials as low as possible, state of the art fuel cells need specific conditions of humidity, temperature, pressure, stoichiometry, catalyst loading and type, etc. Changes in operating conditions and degradation can affect the anode and the cathode in different ways. However, overall cell voltage measurement does not provide electrode-specific information, and special techniques are required to discern the effects occurring at each electrode.

1.6 WATER IN PEMFC

Polymer electrolytes for fuel cells require the presence of water to conduct protons. There is a direct relationship between their water content and their conductivity, as shown in Figure 1-5 [29]. As it is well known, the humidity in a gas mixture is only a function of temperature, but in a fuel cell, there are a lot of parameters that contribute to the control of the water content in the membrane (thickness, hydrophobic and hydrophilic species content, electro-osmotic drag, diffusion, etc.) [30-32]. Fuel cells use different types of membranes, such as perfluorsulfonated ionomer membranes. An ionomer is a polymer that comprises repeat units of both electrically neutral repeating units and a fraction of ionized units (usually no more than 15 percent). Ionomers have unique physical properties including electrical conductivity and isoviscosity (increase in ionomer solution

viscosity with increasing temperatures) [33]. The first ionomer discovered was Nafion[®] by Walther Grot of Dupont in the late 1960's [34] and it is still the most frequently used. Nafion[®] is comprised of a hydrophobic polytetrafluoroethylene (PTFE) backbone and pendant perfluorinated vinyl ether side chains, terminated by hydrophilic sulfonic groups, as shown in Figure 1-6. The ratio of the hydrophobic backbone to the hydrophilic side chains determines the equivalent weight (EW) of the polymer membrane [35]. The equivalent weight is the ratio of dry polymer's weight to the amount of anionic groups, as shown in equation (1-31). The sulfonic acid (anionic) groups in the membrane are responsible for the proton conduction and hydration properties of the membrane [34-38].

$$EW = \frac{\text{dry weight}}{\text{moles of } SO_3^- \text{ sites}} \quad (1-31)$$

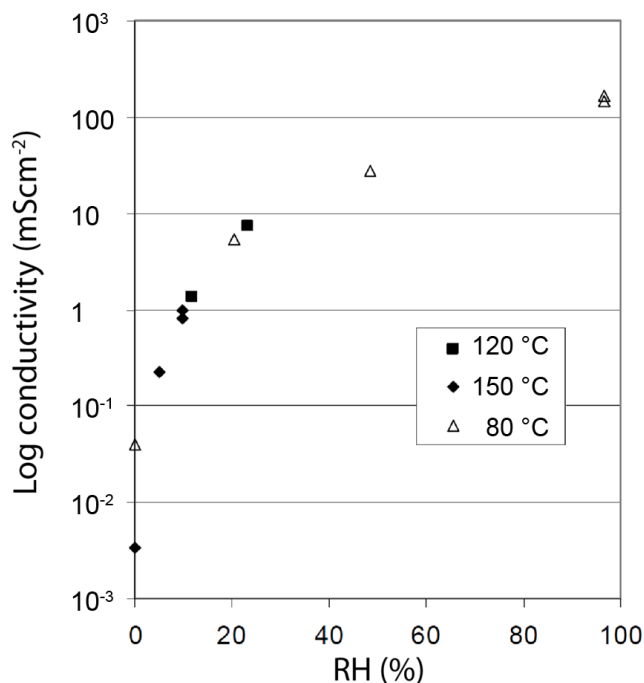


Figure 1-5 Conductivity of perfluorosulfonated membranes, such as Nafion[®], as a function of relative humidity. Adapted from reference [29] with permission.

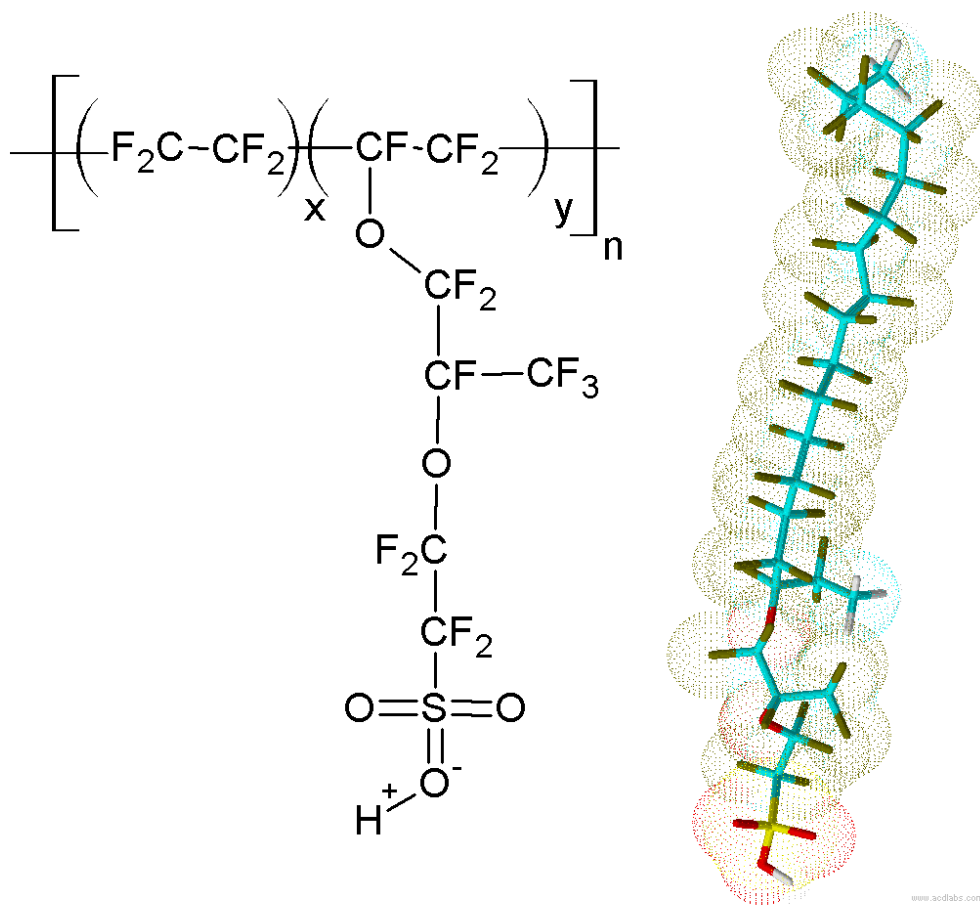


Figure 1-6 Chemical structure of Nafion. Typically $x=6-10$ and $y=1$. For the 3d structure, the values chosen were $x=7$ and $y=1$.

The water content in a proton exchange membrane (λ) is represented by the number of water molecules per active site [38, 39]. The membrane conductivity depends on its water content. There have been numerous models, but very few experimental results for different membranes at different temperatures [38, 40]. According to Zawodzinski's experimental results for Nafion[®] 117 [39], the conductivity at 303.15 K increases linearly with water content (λ), as shown in Figure 1-7.

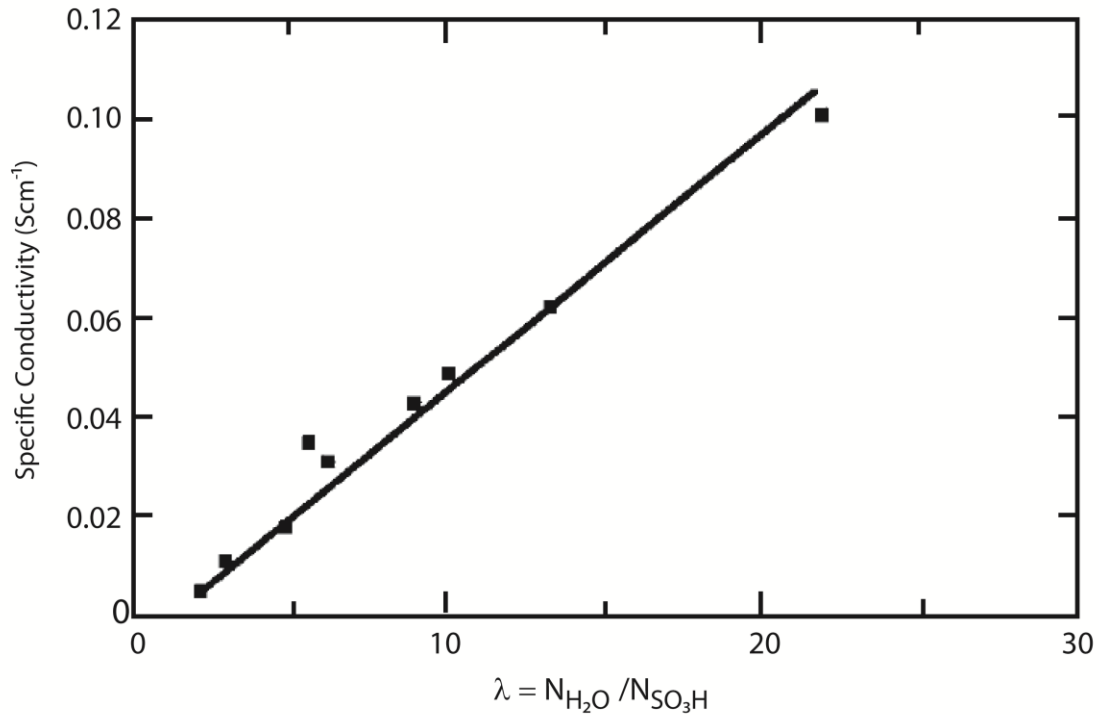


Figure 1-7 Membrane conductivity as a function of water content. From reference [39] with permission.

Fuel cells have a certain conditions of temperature, pressure, humidity, etc. in which the optimal performance is achieved. One of the most important constraints is the humidity control in the system as water is mostly required in the membrane and in the catalyst layer for good proton conduction, but if there is too much, flooding occurs. There are several processes that need to be considered with respect to water in the fuel cell:

- i. Evaporation
- ii. Ohmic heating at high current densities
- iii. Non-uniform levels of hydration
- iv. Drying and humidifying effects of the flowing reactants.

There are several water mechanisms to take into account in a fuel cell: humidification of the anode and humidification of the cathode, evaporation at the anode and at the cathode, water produced in the cathodic reaction, electro-osmotic drag (EOD), and water

diffusion, as shown in Figure 1-8 and expressed by equations (1-32) for the cathode and (1-33) for the anode.

$$N_{W,c,out} = N_{W,c,in} + N_{EOD} - N_d + N_{W,r} \quad (1-32)$$

$$N_{W,a,out} = N_{W,a,in} - N_{EOD} + N_d \quad (1-33)$$

where $N_{W,c,out}$ is the water flux in the cathode outlet stream, $N_{W,c,in}$ is the water flux supplied to the cathode inlet stream, $N_{W,a,out}$ is the water flux in the anode outlet stream, $N_{W,a,in}$ is the water flux supplied to the anode inlet stream. N_{EOD} is the water flux moved through the membrane due to the electro-osmotic drag (ωN_{H^+}), and $N_{W,r}$ is the water produced by the electrochemical reaction. The water diffusion through the membrane (N_d , $\text{molm}^{-2}\text{s}^{-1}$) is due to a gradient of activity:

$$N_d = \frac{1}{A} \frac{dn_{H_2O}}{dt} \frac{\hat{r}}{|\hat{r}|} \propto a_{H_2O} \quad (1-34)$$

where A is the area, n_{H_2O} is the water molar rate, t is time, \hat{r} is a vector orthogonal to the area through which water is diffusing, and a_{H_2O} is the activity of water. The activity gradient has been described as a concentration gradient [41].

The water content in the inlet streams depend on the humidity of the gases, which depend on the gas flow. Many models have emerged trying to describe the water mechanisms inside a fuel cell [37, 42-50] and considerable computer power is necessary when three dimensions and two phase flow is taken into account.

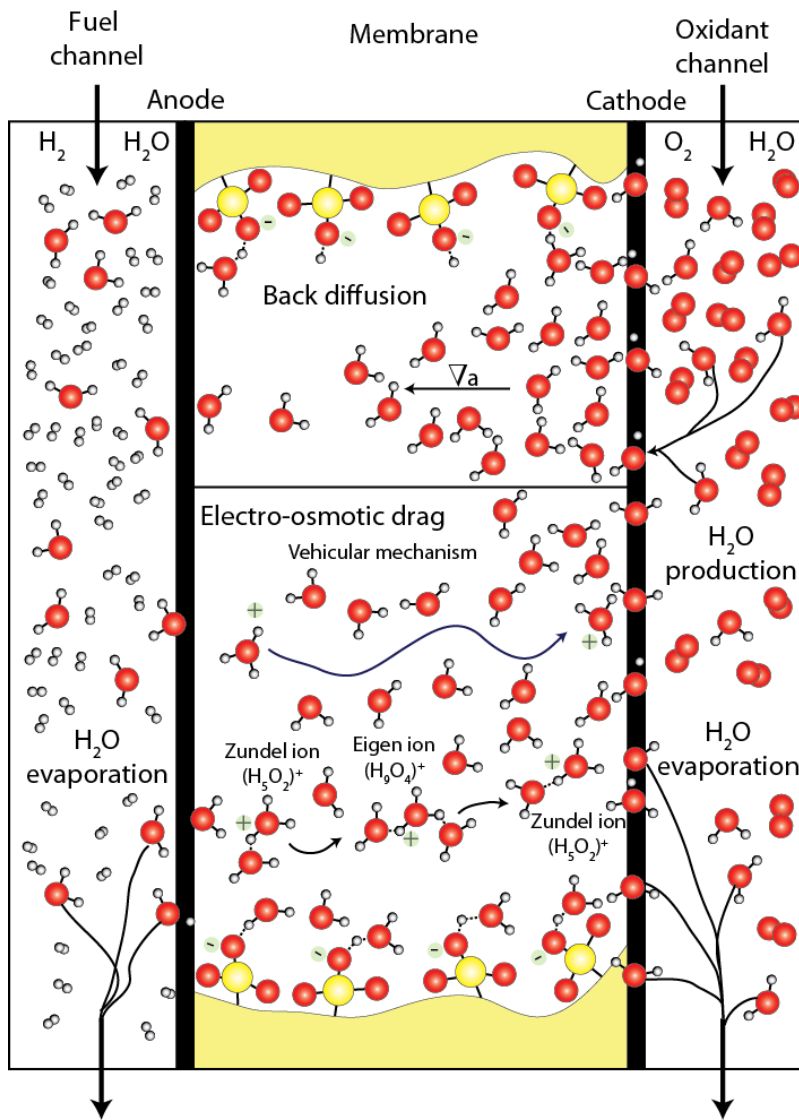


Figure 1-8 Some of the most important water mechanisms in a PEMFC. Here, the fuel (hydrogen in white) and the oxidant (oxygen in red) are humidified. The active sulfonic sites (sulfur in yellow) of the persulfonated membrane carry protons as ions and water charged molecules. The transport through the GDL and the two phase flow are omitted.

The gases are usually humidified and the water content can be known by calculating their relative humidity. In order to calculate the relative humidity, the gas temperature and the dew point temperature (*DPT*) are measured. The dew point temperature is the temperature at which a moist gas needs to be cooled, at constant pressure, for water vapor

to condense into liquid water. This temperature is also equivalent to the temperature of saturation or the temperature at which the liquid and gaseous phases of a material present in a gas are in equilibrium at a given gas pressure. In other words, the dew point temperature is the temperature at which the liquid phase evaporates at the same rate at which it condenses.

The temperature at the catalyst layer, where the water is produced and probably evaporated, depends on the current density. The rate of evaporation is linked to the flow rate, the humidity levels and the temperature of the surroundings. The water produced by the electrochemical reaction ($N_{W,r}$) can be described by a form of Faraday's law for electrolysis:

$$N_{W,r} = \frac{iA}{zF} \quad (1-35)$$

where A is the area, z is the number of electrons and F is Faraday's constant (96485 Cmol⁻¹) and i is the current density.

The electro-osmotic drag (EOD) is the method through which water is carried from the anode to the cathode by the protons that go through the membrane due to the dipolar moment created between the molecules. There are two mechanisms that have been proposed:

- i. Vehicular-mechanism: The protons move as hydroniums (water cations produced by water protonation) from the anode side of the membrane to the cathode side of the membrane without transferring protons [35].
- ii. Grotthuss mechanism: It was first published in 1806 by Grotthuss, when there was no knowledge of the water molecule being comprised of an oxygen molecule and two hydrogen molecules [51]. The process can be described as a proton hopping mechanism between two solvated structures: the Eigen cation ($H_9O_4^+$) and the Zundel ($H_5O_2^+$), as shown in Figure 1-8 [35, 52].

The proton flux due to the EOD (N_{EOD}) is a function of the water drag coefficient (ω) and the protonic flux through the membrane (N_{H^+} , molm⁻²s⁻¹) that can be obtained

experimentally [35, 39, 53-60]. The ω is the number of water molecules that are transported by a proton and is a function of temperature and the hydration state, as shown in Table 1-1. Proton transport occurs only by migration under the action of the electric field and convection due to the water flow in the membrane pores. The proton concentration is constant in the membrane (i.e., depends only on the number of active sites of the membrane). Therefore, there is no proton transport by diffusion as there is no activity gradient inside the membrane. However, there can be an activity gradient between the anode and the cathode membrane surfaces.

	T (K)	Hydration state	ω (H₂O/H⁺)	PEM
Zawodzinski et al. [60]	30	22 (H ₂ O/SO ₃ H)	~2.5	Nafion® 117
Zawodzinski et al. [60]	30	1 –14 (H ₂ O/SO ₃ H)	~0.9	Nafion® 117
Fuller and Newman [54]	25	1 –14 (H ₂ O/SO ₃ H)	0.2 - 1.4	Nafion® 117
Ise et al. [57]	27	11 –20 (H ₂ O/SO ₃ H)	1.5 - 3.4	Nafion® 117
Xie and Okada [58]	Ambient	22 (H ₂ O/SO ₃ H)	~2.6	Nafion® 117
Ge et al. [56]	30-80	0.2-0.95 (activity)	0.3 - 1.0	Nafion® 117
Ge et al.	30-80	Contact with liquid water	1.8 - 2.6	Nafion® 117
Aotani et al. [53]	70	2 – 6 (H ₂ O/SO ₃ H)	2.0 - 1.1	Nafion® 115
Ye et al. [59]	80	3 – 13 (H ₂ O/SO ₃ H)	~1.0	Layered Nafion® 115

Table 1-1 Some reported water drag coefficients (ω) for Nafion® [35]

There are many different types of Nafion® membranes that differ in thickness as shown in Appendix A.5. The desired operational relative humidity of the environment surrounding the Nafion 115 membrane is between 82-100% ($\lambda \sim 22$), but depending on the characteristics of the membrane, the casting method, the reactivation, etc., the range of operation can increase [29]. As can be seen in Figure 1-9, it is difficult to maintain this optimal condition. In the figure the flow rates equivalent to stoichiometric ratios are changed between 2 and 6, and at different pressures (1 and 4 atm). The stoichiometric ratio(ν)¹ is the amount of reactants needed to have a complete reaction, i.e., where no residues from the reactants remain. The region chosen by the author to be too wet

¹ Traditionally λ is used to represent this ratio, but in this thesis we will use ν to avoid confusion with the water content in the membrane, λ

(flooding) or too dry (dehydration) depends on the membrane's characteristics. These two conditions of humidity have a negative effect on the fuel cell, increasing different overpotentials, leading to voltage losses, as will be detailed below.

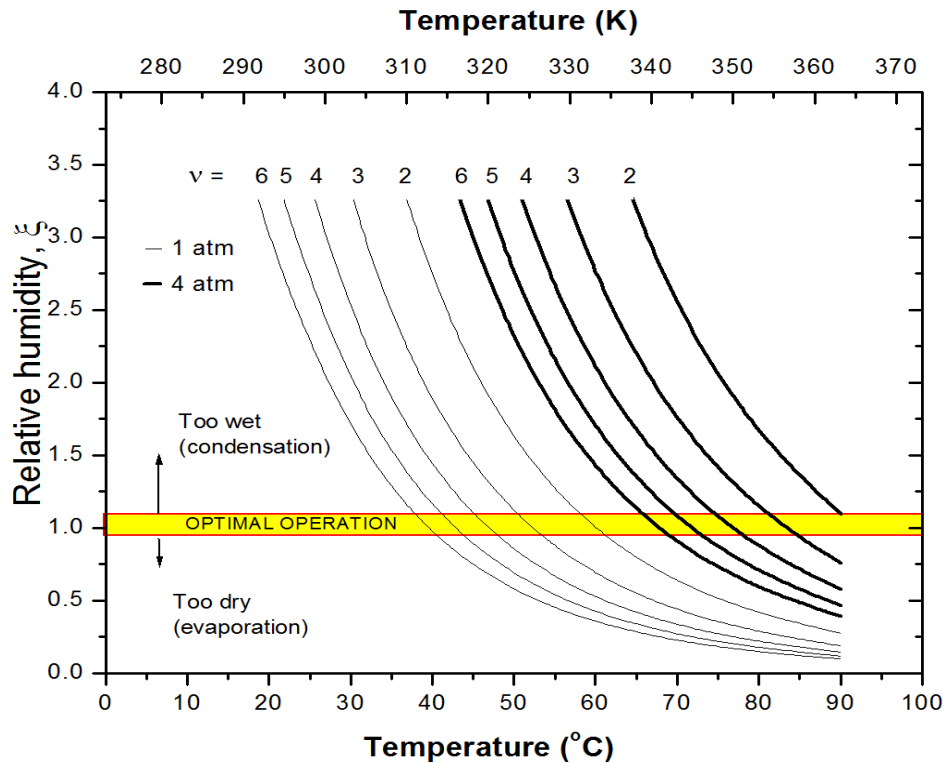


Figure 1-9 A graph of relative humidity versus temperature for the exit air of a PEMFC with air stoichiometry of 2 and 4. From reference [61] with permission.

1.7 FAILURE MODES

There are different types of failure modes associated to abnormal conditions of operation, such as, reactant starvation (low stoichiometric ratio), dehydration, flooding, etc. In order to achieve optimal performance, it is necessary to understand each of these failures, detect them and ultimately diagnose them in a running fuel cell. In Table 1-2 (updated from St-Pierre, 2007 [62]) a summary of some failures modes and the different in-situ detection techniques is shown.

	Failure mode	Target	Type of measurement	Invasiveness ²	Can be used in applied fuel cell	Cost ³
Magnetic resonance imaging [63-67]	Flooding and drying	FF, GDE, membrane	External MRI	High	No	High
X-ray [68, 69]	Flooding and drying	GDE, membrane	External beam	Low	No	High
Neutron imaging [70-84]	Flooding and drying	FF, GDE, membrane	External beam	High	No	Very high
Transparent fuel cell [55, 85-93]	Flooding and drying	FF	Camera	High	No	Medium
Residence time distribution [94, 95]	Flooding and drying	FF, GDE	Residence time of a trace substance	Low to high	Yes	Low
Pressure drop [87, 88, 96, 97]	Flooding	FF, GDE	Pressure drop	Low to high	Yes	Low
Ionic resistance [98-102]	Flooding and drying	Membrane	Ionic resistance in wires in the membrane	Low to high	Yes	Low
Infrared adsorption [103]	Flooding and drying	Membrane	External light source	High	No	Medium
Raman microscopy [104]	Flooding and drying	Membrane	External light source	High	No	Medium
Fluorescence microscopy [105]	Flooding and drying	Membrane	External light source	High	No	Medium
EIS [61, 106, 107]	Flooding, drying, CO poisoning, starvation	FF, GDE, membrane	External AC signal input	Medium	Yes	Low
Diagnostic cells [108, 109]	CO poisoning, starvation	FF, GDE, membrane	Potential response	High	Yes	Medium
DHE [110]	Starvation	GDE	Potential response	High	Yes	Low
RHE [111-114]	Flooding, drying, starvation	FF, GDE	Potential response	Low	Yes	Low
This work						
Ideal	As many as possible	FFC, GDE, membrane	Potential response	Low	Yes	Low

Table 1-2 Operating failure modes measurement summary.

² High: Fuel cell design changes, Medium: fuel cell material changes, Low: fuel cell design or materials changes are not required

³ High: major equipment (equipment requiring dedicated personnel for operation or dedicated space situated at only a few locations worldwide), High: major equipment (equipment requiring dedicated personnel for operation or dedicated space), Medium: Medium equipment (equipment not requiring dedicated personnel for operation or dedicated space), Low: minor equipment (equipment not requiring dedicated personnel for operation nor dedicated space)

1.7.1 Starvation or low stoichiometric ratio

In most electrochemical systems, an excess of reactants is needed to overcome mass transport limitations. Therefore, a $\nu > 1$ is used. For PEMFC the usual values of ν range between 1.2 – 1.5 for the fuel (if pure hydrogen is used) and 1.5 – 3 for the oxidant (if air is used). Starvation refers to a low fuel or oxidant input to the fuel cell, the most important being anode starvation. For a PEMFC, depending on the type and area of the MEA, the failure can start with $\nu_{Fuel} < 1.1$, while using pure hydrogen as fuel [110, 113] and $\nu_{Oxidant} < 1.4$, while using air as the oxidant [14, 115]. It can arise from a lack of system control during a sudden change in reactant demand, uneven pressure distribution within the cell or between cells in a stack or even a compressor failure. This is a failure of high importance, as the lack of fuel or oxidant reduces drastically the performance and can drive the fuel cell into cell reversal [116-118]. At potentials of -2.0 V or less the MEA can be electrically shorted, which is irreparable [14, 17, 42, 61].

The prolonged or repeated fuel starvation results in damage through carbon corrosion. When this occurs, the fuel cell is damaged in different areas containing carbon (supported catalyst, GDL, etc.). Another effect of fuel starvation is that it can lead to dehydration, as the reactions that occur consume water. Dehydration, as will be described below, can accelerate membrane degradation [42, 61, 119-121].

1.7.1.1 Diagnostic techniques for low reactant flow or Starvation

Many groups have investigated this failure mode [116-118, 122-129]. Other investigations studied the behaviour of a PEMFC after cell reversal [130], proposed a transient analysis of starvation (undershoot / overshoot of the transition) [131], created a current distribution mapping method that studied the starvation mode [132], and developed a low cost diagnosis technique that involved the screening of the MEA (Membrane Electrode Assembly) achieving different zones of analysis [133]. Other efforts have taken advantage of the specific behaviour of the anode or cathode starvation [42, 134-136] to improve the fuel cell performance by starving regions of the fuel cell that result in the oxidation and removal of electrocatalyst poisons, and ultimately be able to diagnose this failure [108].

These research efforts resulted in the development of different strategies to mitigate the effect of reactant starvation in fuel cells and different diagnostic methods to detect reactant starvation. Diodes (electrical device allowing current to move through it in one direction with far greater ease than in the other) can be connected to carry current externally, or the potential of all cells can be monitored, but they are expensive and external approaches. Testing of the anode outlet stream for O₂ and CO₂, or incorporating cell reversal tolerance within the MEA, is a better approach, but also expensive because of the need for external equipment, such as, mass spectrometers and sensors [130]. Improving cell reversal tolerance involves incorporating electrocatalysts to promote the electrolysis rather than the carbon corrosion reaction [134-136]. Alternatively, integration of diagnostic cells in the fuel cell stack that can detect detrimental operating conditions before the failure appears is another method [108].

For any electrochemical system, there are in-situ and ex-situ methods for measuring, exploring, and diagnosing fuel cells. In-situ methods are measurements done within an operational electrochemical device. Ex-situ methods are measurements done outside of the electrochemical system, such as microscopy of the electrode before or after operation. The ex-situ electrochemical methods for fuel cells are usually based on a classical three-electrode cell arrangement (working electrode, reference electrode and counter electrode) [137]. Electrochemical techniques by themselves are not enough to diagnose reactant starvation in fuel cell systems, as most failure modes induce a voltage drop, even though, the voltages that can be reached are different. The alternative methods of diagnosing this failure include monitoring the anode outlet searching for CO₂ and O₂, measuring the voltage of each cell in a fuel cell stack, diagnostic cells [108, 109], and for this project, reference electrodes.

The early, reliable, and cost effective diagnosis of this failure mode is imperative, as the damage that it can produce is irreparable. The use of techniques like the reference electrodes approach that are cost effective and reliable is a valuable tool because of the characteristic potential response to the failure.

1.7.2 Dehydration

Low water content in a fuel cell can mean that the membrane is not well humidified. During this process, the membrane suffers a reduction in size of the ionic clusters, and in the diameter of the membrane channels. Smaller channels limit the hydrated ions and the protonic mobility. When the membrane is not well humidified, there is a loss of ionic conductivity in the membrane and the potential is reduced.

This failure mode is very common, especially on large stacks, as there is a need for high stoichiometries, high currents, and high flows (usually in the cathode), which can easily lead to membrane drying. After this failure mode appears, the fuel cell never recovers, as shown in Figure 1-10. The modification of the membrane affects the performance even after re-humidification. It is clear that good diagnosis is imperative for this failure mode, as the longevity and reliability of the fuel cell and/or stack can be compromised after this failure mode occurs.

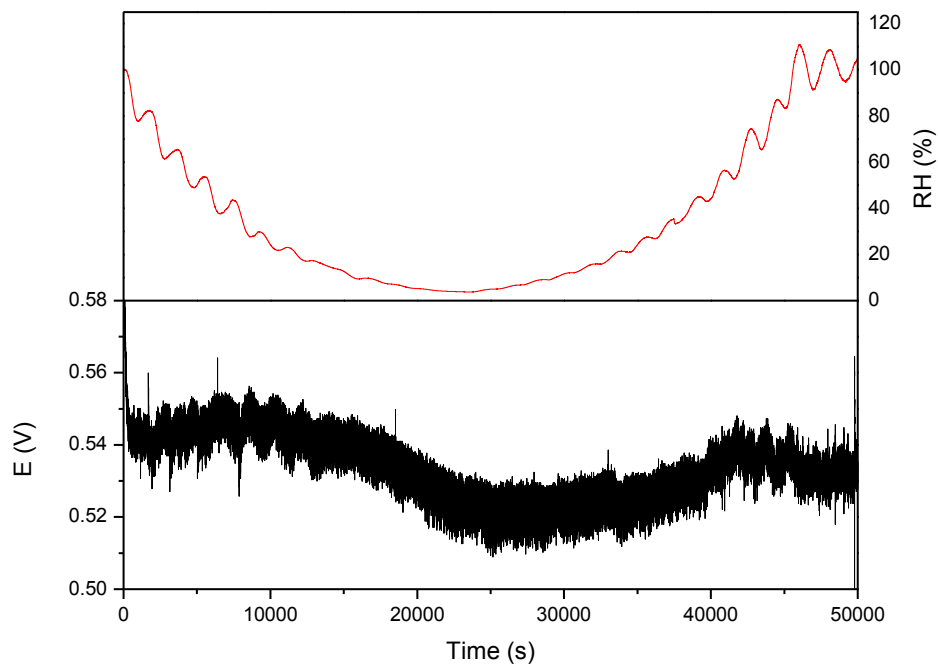


Figure 1-10 Voltage drop due to dehydration.

1.7.2.1 Diagnosis Techniques for Dehydration

Electrochemical diagnosis of dehydration is a very broad field and the reliability of the studies has increased over time. The main diagnosis tool was the polarization curve. The response signal is a voltage drop that is complicated to decouple from other failure modes, even though the timelines of the different failures can be different.

There are other methods to diagnose this dehydration failure: the measurement of the resistance directly [43, 138] or by means of Electrochemical Impedance Spectroscopy (*EIS*) [61, 106, 107]. The *EIS* technique is very accurate but increases the cost and adds extra equipment necessary to read and impose certain frequencies.

Ideally, for this failure mode, and all others, there should be a specific voltage response that can be associated with this failure. This can be done with the aid of sensing electrodes as they are more sensitive to local conditions.

1.7.3 Flooding

As previously mentioned, humidity is one of the most important parameters to control, as the ohmic resistances are inversely proportional to the water content. Flooding can appear when a cell is not well designed, when the inlets are over humidified, or when a high current density is required (i.e., high quantities of water are produced). This failure also depends on the characteristics of the gas diffusion layer, porous electrode, and the membrane. The formation of liquid water, especially in the cathode, leads to two-phase flow that can impede the reactant transport to the active catalyst sites (where the reaction actually takes place). This results in an increase of mass transport losses, but also some kinetic overpotential, as the three phase contact cannot be achieved.

Flooding is one of the most common failures in fuel cell stacks and one of the most complicated to diagnose. This is because the failure occurs suddenly and can be easily confused with dehydration (a voltage drop occurs), as shown in Figure 1-11 at a current density of 1 Acm^{-2} . To flood the MEA, water removal from the stack must be lower than water production. High water production is equivalent to high load currents; low water

removal occurs when the gas flow rates and temperatures are low. To achieve dehydration, the inverse procedure can be followed.

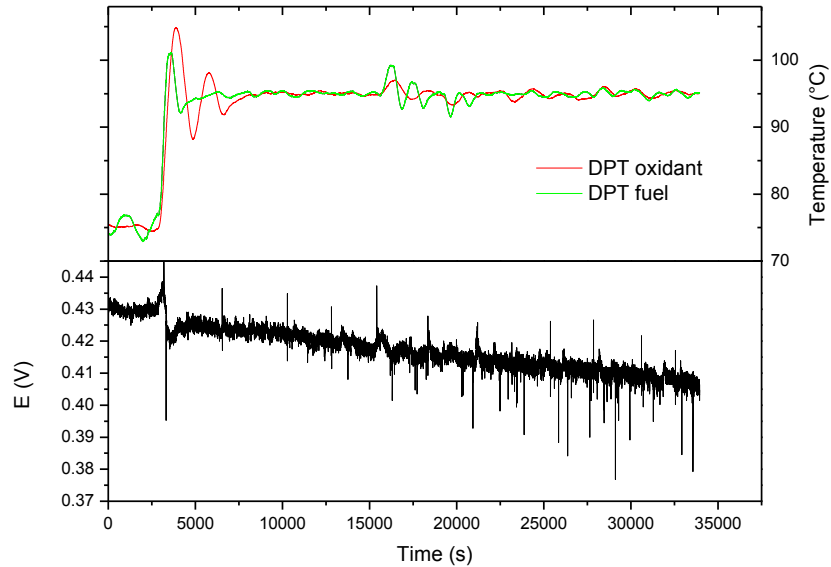


Figure 1-11 Voltage drop after RH is increased above 100% (from DPT = 75 °C to DPT = 95 °C). The cell and gas temperatures are maintained constant at 75 °C.

The performance decay is critical as shown in Figure 1-11 but if a purging system is used the effects can be mitigated. Nevertheless, there has been much effort to look for ways to prevent and/or correct this failure mode, especially from the fuel cells and car manufacturers [139-146]. As overall fuel cell performance is strongly associated with the water management of the fuel cell, it is imperative to understand the mechanisms, and prevent dehydration and flooding modes.

1.7.3.1 Diagnosis Techniques for Flooding

The difficult diagnosis of this failure mode through electrochemical methods (polarization curves) has led researchers to come up with different techniques that involve purging [147], the use of multicomponent gases, or pressure drop associated with voltage drop caused by flooding [97]. In this thesis reference electrodes are used to diagnose this failure, as the potential response is unique.

This failure can be decreased with the use of a purging system, as well as increasing the reactant flow rate. The complication of increasing the flow rate comes from the requirements of the external equipment (e.g., blowers, pumps, mass flow controllers) and drying effects with certain flow-field designs. It is of great importance to understand the water mechanisms throughout the fuel cell. That is why novel and advanced technology devices have been used to determine this behavior. These efforts include the use of neutron imaging [70-84], magnetotomography [148], Magnetic Resonance Imaging (*MRI*) [63-67], current distribution (associated with the water production) [132, 133, 149-151], and others.

With this knowledge, and the understanding of the water mechanisms that occur inside the fuel cell, it is possible to improve the design of the fuel cells and have sensing electrodes that are able to respond to more than one failure mode at a time (i.e., dehydration, flooding, starvation, etc.).

1.8 REFERENCE ELECTRODES

The electrochemical potential of a system or a reaction cannot be determined absolutely. It is referred to as a potential relative to a fixed and known electrode potential set up by a reference electrode in the same electrolyte [152, 153]. A reference electrode is a stable electrode with a known potential and independent of the current density of the system in study [137, 154]. The electrode potential of the electrode of interest or working electrode (*WE*) can then be measured with a high impedance instrument and a reference electrode (*RE*), as shown in Figure 1-12. The instrument for measuring the electrode potential must have a high impedance in order that it does not draw a significant current through the reference electrode (which would change the latter's potential) and sufficient accuracy and precision to measure a wide range of potentials [137].

In potentiostatic experiments (where potential is fixed), the potential between the working electrode and the reference electrode is controlled by a potentiostat, and as the reference half cell maintains a fixed potential, any change in applied potential to the cell appears directly across the working electrode-solution interface. The reference electrode serves the dual purpose of providing a thermodynamic reference and also isolates the

working electrode as the system under study. In practice, however, any measuring device must draw current to perform the measurement, so a good reference electrode should be able to maintain a constant potential even if a few microamperes are passed through its surface. This criterion will be satisfied if the exchange current density is high and hence the reaction is totally reversible [154].

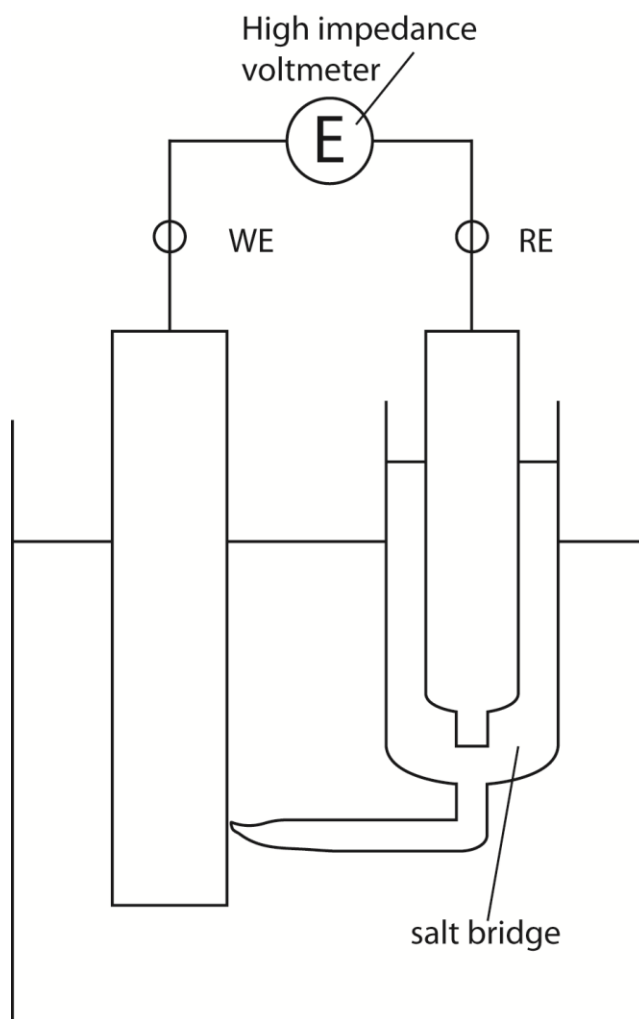


Figure 1-12 Measurement of an electrode potential with a reference electrode. The tube joining the reference electrode with the working electrode is called a Luggin capillary. It helps to reduce the inclusion of iR drop in the measurement.

In order to be able to measure overpotentials (i.e., when a current is applied) and the reference electrode cannot withstand the supplied current without modifying its potential, an auxiliary electrode, also called a counter electrode (*CE*) is used. The purpose of the counter electrode is to supply the current required by the working electrode without in any way limiting the measured response of the cell [154]. Therefore, the counter electrode usually has a larger active area and the half cell reaction of the selected counter electrode is also faster than that of the working electrode. A diagram of a typical three-electrode system is shown in Figure 1-12. The reference electrode has to be as close as possible to the working electrode (without touching it) to reduce the potential losses due to resistance (i.e., iR drop). In the case of liquid electrochemical systems, a Luggin capillary can be used.

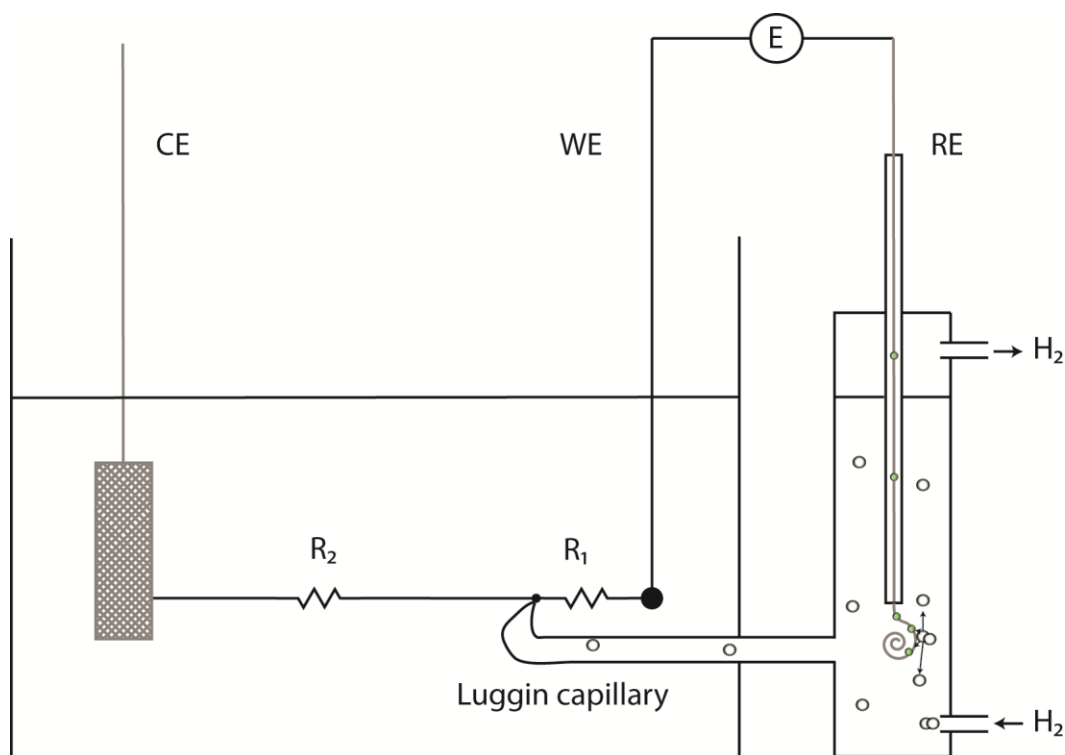


Figure 1-13 Three-electrode system required to measure electrode overpotentials, i.e., $\Delta E - \Delta E_e$. The potential between the working electrode and the reference electrode when both ΔE and ΔE_e correspond to the same reaction is equal to the overpotential η . The Luggin capillary reduces the distance between the RE and the WE and thus, reduces the iR drop.

The reference electrode shown in Figure 1-13 is a hydrogen electrode and supports the dynamic equilibrium:



This reversible reaction is usually established on a specially prepared catalytic surface of platinum black, i.e., a dispersed high area electrodeposit of platinum particles on a platinum substrate. Under standard conditions, i.e., using materials in their standard state, a hydrogen pressure of 1 atm and a proton activity of 1, the potential of the standard hydrogen electrode (SHE) is, by convention, taken as exactly zero for all temperatures.

Reference electrodes can also be used to separate the anodic and cathodic contributions in an electrochemical system. Reliable reference electrodes are critical for the understanding of electrochemical systems, but they can be difficult to implement. Even in standard aqueous systems, reference electrodes may provide inaccurate measurements if the ohmic drop is non-uniform in the electrolyte [155]. When this occurs, the reference electrode must be placed far from the active region of the working electrode [156] or a supporting electrolyte must be used to minimize the ohmic drop [137]. For solid systems positioning is further complicated by inaccuracies in the measurements due to the misalignment of the electrodes [27, 157-160], as shown in Figure 1-14. In these systems the reference electrode distance to the active area also plays an important role. According to Adler et al, when a flat geometry is used, the electrical potential lines become constant when the distance from the active region to the reference electrode is more than three times the thickness of the electrolyte [27]. Furthermore, Krishnan et al showed that even with perfect alignment there could be inaccuracies [161]. The results of these and other studies on solid oxide fuel cells [27, 157, 161, 162] have been corroborated on proton exchange membrane fuel cells (PEMFC) [110, 111, 114, 158-160, 163, 164].

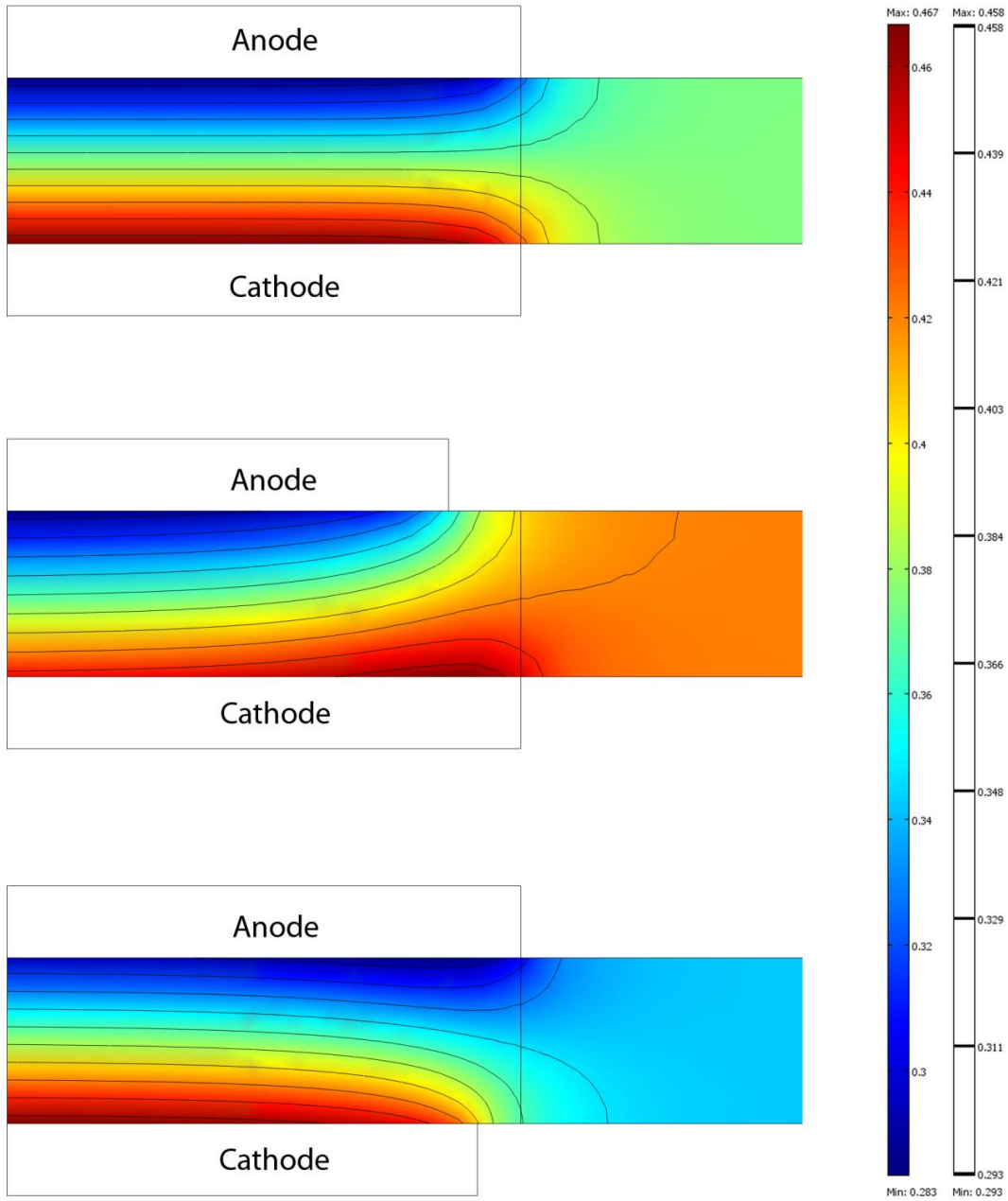


Figure 1-14 Effects to the potential profiles of the misalignment of the anode and cathode electrodes in a solid electrolyte. The figures were modeled with Comsol Multiphysics[®] software.

Despite these challenges, accurate results can be obtained [106, 165-169]. One approach is to have more than one reference electrode to validate the data as suggested by Liu, et al [160] and implemented by Li, et al[167] and the work in this thesis [111, 114]. Lauritzen, et al[110] used a Dynamic Hydrogen Electrode (DHE), which needs current to remain stable. Using a Reversible Hydrogen Electrode (RHE) is a better approach because it is possible to know its potential accurately and there is no need for an imposed external current. Springer, et al [41] used a disk of catalyzed electrode that was hot-pressed to the membrane exposed to the H₂ feed. This system provides stable and repeatable contact, but is complicated to implement in a regular fuel cell, as the electrodes are 3 mm in diameter and the MEA needs to be modified. Ticianelli et al[170] used a platinum mesh as an RHE, but only the cathode results were presented.

As mentioned previously, the rate-determining reaction for the PEMFC is the oxygen reduction reaction. Nevertheless, the anodic hydrogen oxidation reaction can have a significant overpotential affecting the overall fuel cell voltage loss [171, 172]. Therefore, it is essential to understand the individual electrode overpotentials with a reliable reference electrode in order to understand performance effects [158, 171]. A general reference electrode in contact with the electrolyte and electrically isolated to the plates is shown in Figure 1-15. This arrangement allows to measure the individual potential of the anode or the cathode.

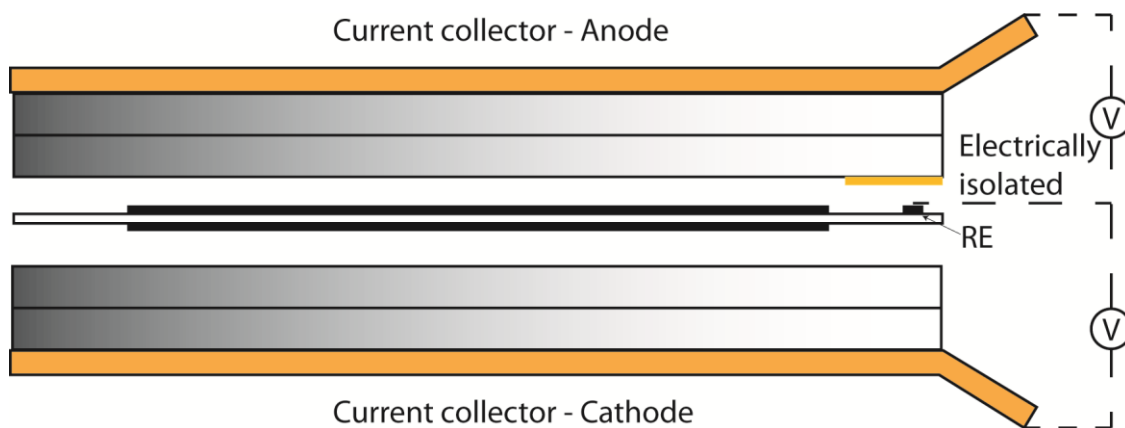


Figure 1-15 General electric connection and placement of reference electrodes in a fuel cell.

The performance of fuel cells is highly dependent on the local conditions over the active area. The levels of hydration, temperature, pressure, and reactant concentration play a major role in the uneven distribution of potential over the active area [133, 173-180]. Reference electrodes are also affected by these conditions. This was shown by Mitsuda et al for phosphoric acid fuel cells [181] and later by Siroma et al for the PEMFC [169]. Therefore, in order to have a reliable reference electrode, it is necessary to know and/or control the environmental variables that affect them. If the reference electrode is subject to the changing local conditions and it is affected by them, it is not a reference electrode by definition. For that reason, prior to the work that led to this thesis, there has never been reported a real reference electrode working inside a proton exchange membrane fuel cell (running with gases) under real operating conditions [111, 114]. However, electrodes at non-constant conditions can be used as a diagnostic system as they are very sensitive to local conditions [110-112]. These electrodes are able to sense different failure modes before they affect the whole fuel cell system, hence the name: sensing electrodes (*SE*).

2 RESEARCH OBJECTIVES

The objective of this research is to develop and test a sensing electrode system to diagnose failure modes; and a reference electrode system to accurately measure the individual anode and cathode potentials of a proton exchange membrane fuel cell. The project involves the following features:

- I. The development of a diagnostic system based on sensing electrodes for different failure modes. The related secondary objectives included:
 - To demonstrate and characterize the sensing electrodes for flooding.
 - To demonstrate and characterize the sensing electrodes for dehydration.
 - To demonstrate and characterize the sensing electrodes for low reactant flow or starvation.
- II. The development and characterization of a reference electrode system for PEMFC
 - Measure and characterize the anodic and cathodic individual potentials while fuel cell operates under normal operating conditions (i.e., RH = 100%, $v_{H_2} = 1.5$ and $v_{air} = 2$).
 - Measure and characterize the anodic and cathodic individual potentials while fuel cell operates under dehydrating conditions (i.e., RH = 0%, $v_{H_2} = 1.5$ and $v_{air} = 2$).
 - Measure and characterize the anodic and cathodic individual potentials while fuel cell operates under flooding conditions (i.e., RH > 100%, $v_{H_2} = 1.5$ and $v_{air} = 2$).
 - Measure and characterize the anodic and cathodic individual potentials while fuel cell operates under low reactant operating conditions (i.e., 100 % RH, $v_{H_2} < 1.5$ or $v_{air} < 2$).
- III. The development and characterization of a current mapping system for a PEMFC
 - Measure and characterize different failure modes over the active area
 - Obtain individual anodic and cathodic overpotentials and heat signatures under different conditions over the active area.

3 THESIS LAYOUT

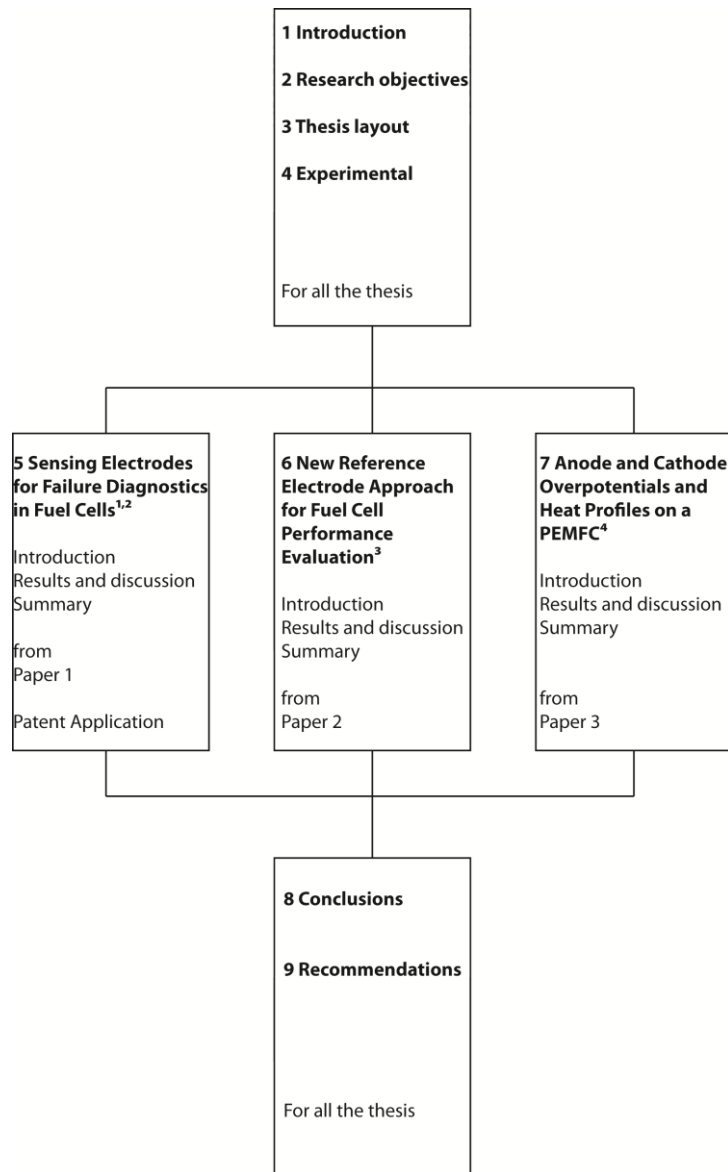


Figure 3-1 Thesis layout

¹Herrera, O., W. Mérida, and D.P. Wilkinson, *Sensing electrodes for failure diagnostics in fuel cells*. Journal of Power Sources, 2009. **190**(1): p. 103-109.

²Herrera, O.E., W. Merida, and D.P. Wilkinson, *Method and Apparatus for Sensing Failure Modes in a Fuel Cell*. 2008: US Patent Application.

³Herrera, O.E., W. Merida, and D.P. Wilkinson, *New Reference Electrode Approach for Fuel Cell Performance Evaluation*. ECS Transactions, 2008. **16**(2): p. 1915-1926.

⁴Herrera, O.E., W. Merida, and D.P. Wilkinson, *Anode and cathode overpotentials and heat profiles in PEMFC*. Submitted to the Journal of Power Sources.

In the following chapters, the results of a reference electrode (*RE*) approach to evaluate fuel cell performance are presented where all the conditions are monitored and controlled. The approach consists of using 6 platinized platinum electrode wires or catalyst patches at constant controlled conditions. With this approach one is able to accurately separate the voltage contributions from the anode and the cathode [111, 112, 114] and avoid errors in the potential measurements due to uneven resistance during dry experiments [164], as shown in Figure 3-1. In this system, the reference electrodes work as a Reversible Hydrogen Electrode (*RHE*) [153], under known conditions (pressure, temperature, and humidity). Hence, the resulting reference electrode potentials can be fully characterized and corrected against the Standard Hydrogen Electrode (*SHE*).

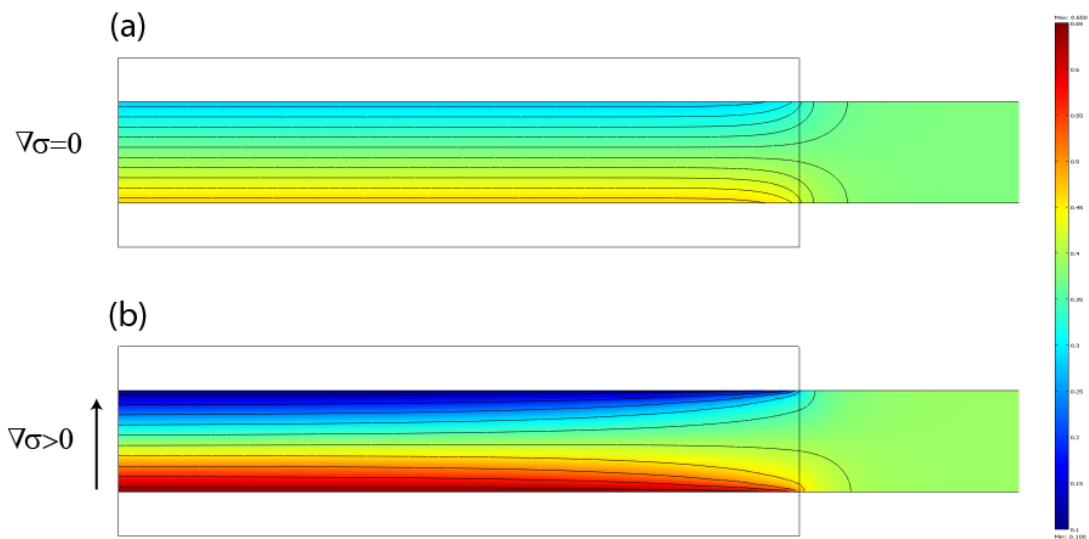


Figure 3-2 Effect on the potential of uneven membrane resistance. The conductivity is homogenous in (a) and it decreases from bottom to top in (b). The figures were modeled with Comsol Multiphysics® software.

Unlike the reference electrodes, the sensing electrodes (SE) are subject to different operating conditions that affect their potential values. These sensing electrodes can be used as diagnostic tools [111, 112]. The sensing electrodes provide a cost effective solution for fuel cell diagnostics, as they have a characteristic potential response to each individual failure. They are barely invasive and they can be easily monitored as only

potential measurements are needed. The SEs were selected due to their versatility of diagnosis, invasiveness and cost.

In Chapter 4, a description of all the hardware used is given: the fuel cell used, the test stations used, the sensing and reference electrodes, their location, the conditions used and the measurements done.

In Chapter 5, the results of a system for diagnosing failure modes are described. The failure modes studied were: flooding, dehydration and low fuel stoichiometry. The demonstration and characterization of the sensing electrodes was carried out at 348 K and 3.04 atm (normal operating conditions for a commercial fuel cell). The failure modes were then simulated by increasing the humidity levels into the fuel cell (flooding), reducing the humidity levels from 100% RH to bypassing the humidity system into the fuel cell (dehydration), and by systematically reducing the flow rate of the fuel into the fuel cell (starvation). The sensing electrodes have a characteristic potential response for each one of these failure modes. The material in this chapter has been published:

- Herrera, O., W. Mérida, and D.P. Wilkinson, *Sensing electrodes for failure diagnostics in fuel cells*. Journal of Power Sources, 2009. **190**(1): p. 103-109.

In Chapter 6, a reference electrode system, where the individual cathodic and anodic potentials can be measured, is described. The reference electrodes were tested while running the fuel cell in different conditions: normal, flooding, dehydration, low fuel stoichiometries and low oxidant stoichiometries. The reference electrodes reported a stable potential during all measurements. The material in this chapter has been published:

- Herrera, O.E., W. Merida, and D.P. Wilkinson, *New Reference Electrode Approach for Fuel Cell Performance Evaluation*. ECS Transactions, 2008. **16**(2): p. 1915-1926.

In Chapter 7, individual cathodic and anodic overpotentials of each segment in a segmented cell are measured by combining reference electrodes with current mapping and multiple gas analysis. The heat signatures are calculated for the different conditions

tested: normal, flooding and dehydration. The material in this chapter is being prepared for submission.

In Chapter 8, the conclusions of Chapters 5-7 are shown. The results are analyzed, suggesting future impact and significance.

In Chapter 9, further recommendations and possible routes to follow are shown.

4 EXPERIMENTAL

4.1 FUEL CELL AND MEASUREMENTS

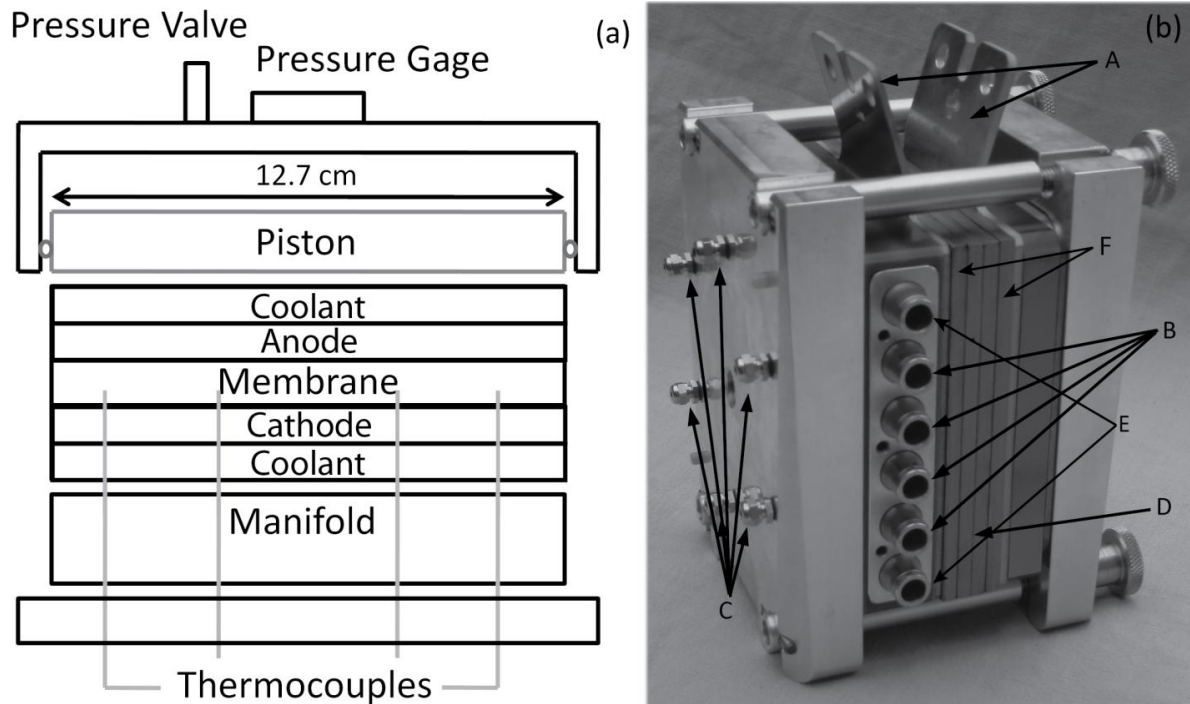


Figure 4-1 (a) Diagram of research fuel cell components (b) Picture of research fuel cell, with components identified: (A) current collectors, (B) gas ports, (C) thermocouple ports, (D) bipolar plates, (E) ports for the water coolant, and (F) coolant plates.

The fuel cell shown in Figure 4-1 was developed in collaboration with Tandem Technologies (the fuel cell diagrams are confidential, but pictures of the hardware and test station are shown in the Appendix A.1). The cell had thermocouple ports that were used to map the local temperature. It also had a pneumatic piston for compression that distributed the pressure evenly across the cell. A cross-flow configuration was used for the anode and cathode flow field of the fuel cell for the experiments of all chapters, except Chapter 7. A picture of the plates used with Kapton[®] pieces is shown in Figure 4-6 (i). The characteristics of the plates are shown in Table 4-1. The temperature of the fuel cell was controlled by water passing through a flow field (shown in Figure 4-2) on the backside of the anode and the cathode. All the experiments were done with custom made

49 cm² Ion Power MEA's described in Table 4-1 (For Chapter 5, custom made E-Tek MEA's were used with the same membrane and loading characteristics). These MEA's were selected because flooding and dehydration failures can be simulated easily. The experiments were carried out with a 500 W Arbin Instruments Fuel Cell Test Station. The test station controlled the flow rate (stoichiometry), humidity, temperature and pressure of the gases supplied. The gas inlet temperatures were maintained constant and the dew point temperatures (DPT) were modified to change the level of hydration in the fuel cell. Another Arbin 50 W test station was used to provide the constant conditions for the reference electrodes in the isolated chambers, as shown in Figure 4-5. The isolated chambers were supplied with a constant flow of fully humidified hydrogen at 75 °C and 1 atm.

Name and units (if needed)	Details
Catalyst loading anode 20% Pt/C (L_a , mg Pt)	0.3
Catalyst loading cathode 20% Pt/C (L_c , mg Pt)	0.7
Membrane	Nafion 115
Gas diffusion layer with microporous layer	SGL Carbon 25 BC
Active area (cm ²)	49
Number of channels	27
Channel length (mm)	176.8
Cathode channel width (mm)	1.575
Cathode channel depth (mm)	1.270
Cathode landing width (mm)	0.864
Anode channel width (mm)	1.270
Anode channel depth (mm)	0.508
Anode landing width (mm)	1.168

Table 4-1 Membrane Electrode Assembly and flow-field details

4.1.1 Operating conditions

The fuel cell was conditioned as described in Appendix A.1.1. The fuel cell was run under different loads (5-1200 mAcm⁻²) for 15 to 30 minutes to obtain the average potential values for the polarization curves. Each polarization curve was run at least 2 times in ascending order and 1 in descending order (for at least 6 of the selected current densities) in order to check for hysteresis (refer to Appendix A.1.2 for detail on the polarization curves protocol). The pressure drop for the anode and the cathode with respect to the flow and current density is shown in Figure 4-2. Table 4-2 summarizes the operating conditions for the normal, flooding, and dehydrating experiments. The temperature of the cell and of all the dry gases used (oxygen, heliox, air, and hydrogen) was maintained constant.

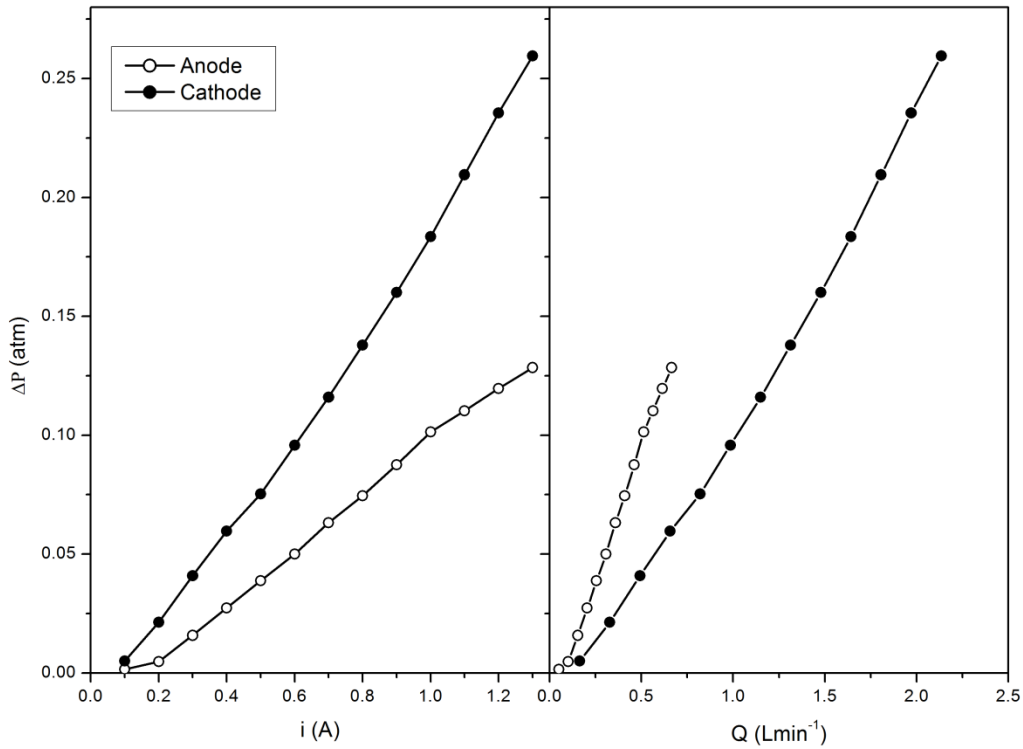


Figure 4-2 Pressure drop of fuel cell with Ion-Power MEA's at different flow rates (anode: pure hydrogen and cathode: air) and the equivalent current densities.

Test	Conditions	Value
Normal	DPT anode (°C)	75
	DPT cathode(°C)	75
Flooding	DPT anode (°C)	95
	DPT cathode(°C)	95
Dry	DPT anode (°C)	Bypass
	DPT cathode(°C)	Bypass
Fuel cell and gas temperatures are maintained constant (°C)		75
Absolute bladder pressure (atm)		8.15
Absolute back pressure (atm)		3.04
Stoichiometry of anode		1.5
Stoichiometry of cathode		2

Table 4-2 Operating conditions for normal, flooding and dry experiments. The stoichiometric flows, the inlet pressure, the temperature of the cell and the dry gases (oxygen, heliox, air and hydrogen) were maintained constant.

4.1.2 Segmented cell measurements

The cathode flow field was divided into 16 segments and used in a co-flow configuration with the anode flow-field. The anode and cathode plates had the same flow-field profile to enhance sealing and maintain good pressure distribution. The current collection of the segmented plate was done by a printed circuit board (PCB) with gold plating as shown in Figure 4-5 and Figure 4-4. The current was converted to voltage with resistors (c) and the signal was amplified before it is sent to the connector (e). Each of the segments current collectors (a) had a General Electric MC65F103B thermistor in the middle (b). The PCB also had 20 extra contacts for the connection of the reference electrodes (d). All the signals were sent to a National Instruments PXI 6255 card and the data was collected with a LabVIEW program. The coolant plate flow field was in cross flow compared to the adjacent flow field. Pictures of the flow fields can be seen in Appendix A.1. The design diagrams for the PCB are included in Appendix A.4.

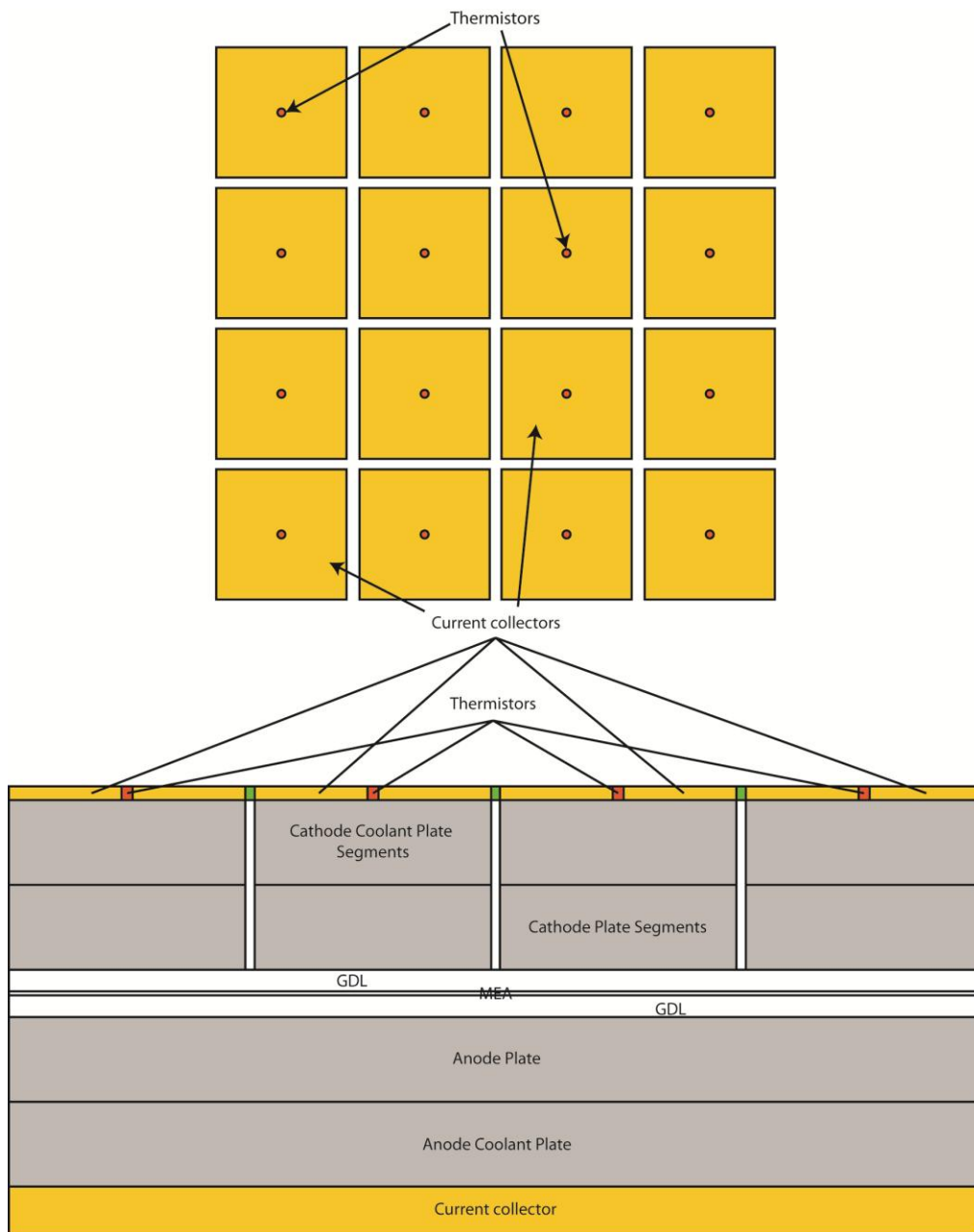


Figure 4-3 Location of the current collectors and thermistors of the PCB with respect to the flow fields.

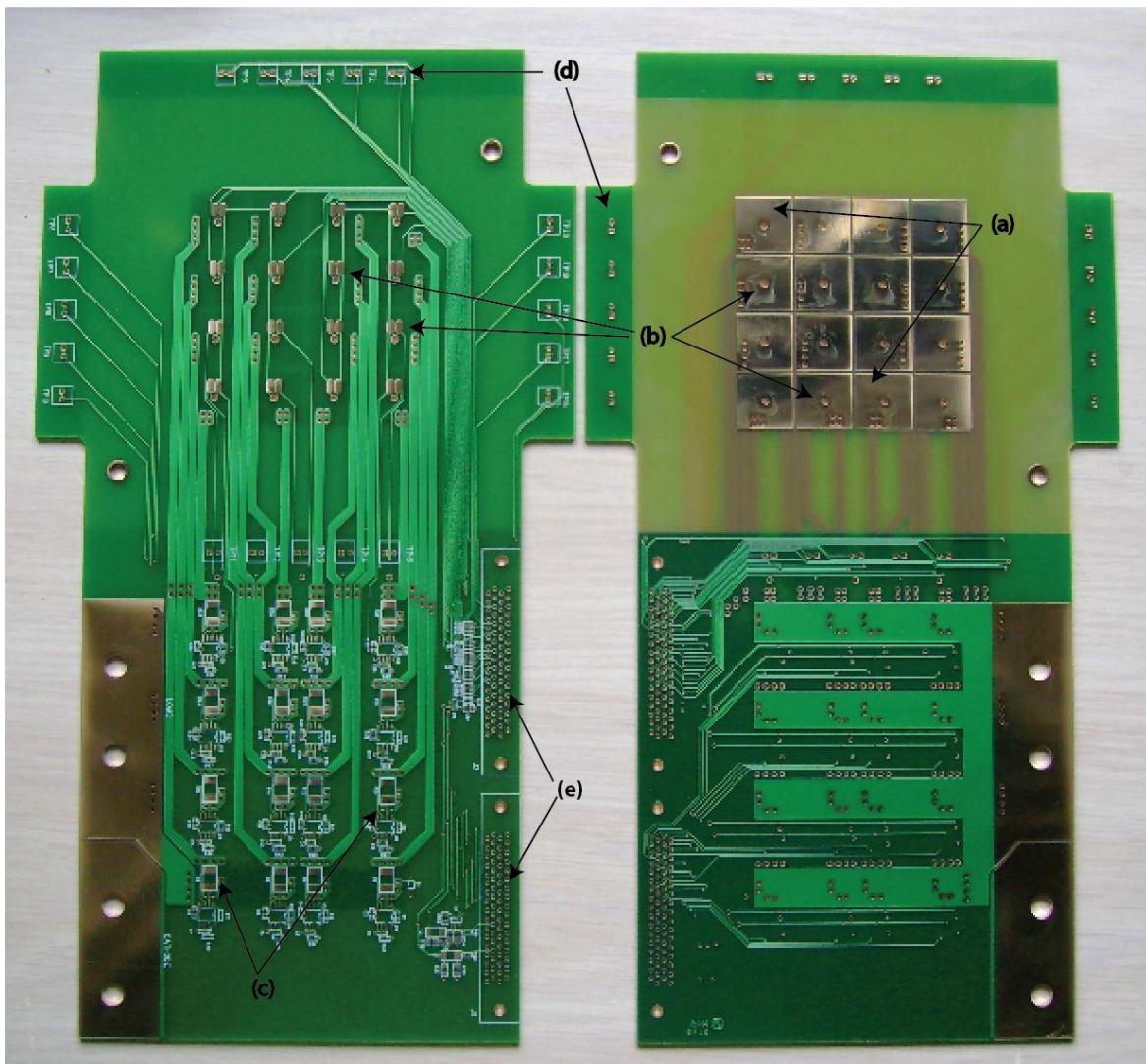
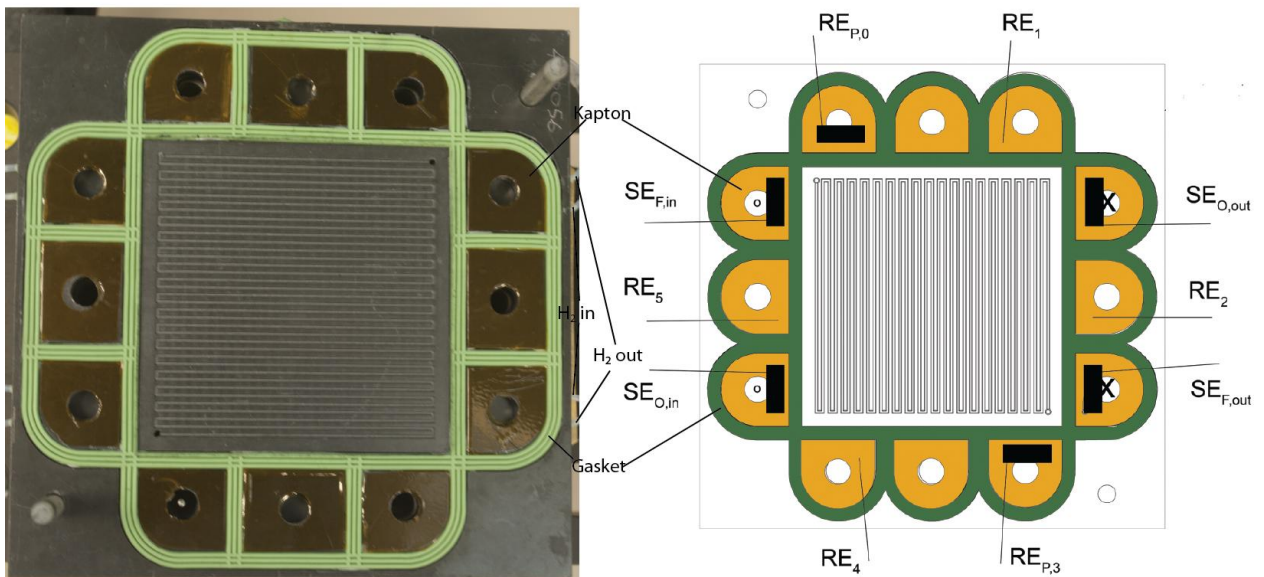


Figure 4-4 PCB with the current collectors (a), thermistors (b), resistors (c), and contact for the reference electrodes (d) for the segmented cathode plate.

4.2 SENSING AND REFERENCE ELECTRODES IN FUEL CELL

The sensing electrodes and reference electrodes consisted of a 50 μm platinum wire with a 25 μm Teflon[®] coating. The Teflon[®] was removed at the wire tip to expose 2 mm of platinum that was cleaned and then platinized according to the procedure described by Ives and Janz [153]. In this work 4 sensing electrodes and 6 reference electrodes were used, as shown in Figure 4-6: one SE in the inlet and outlet of the fuel stream ($\text{SE}_{\text{F,in}}$, $\text{SE}_{\text{F,out}}$, respectively) and one SE in the inlet and outlet of the oxidant stream ($\text{SE}_{\text{O,in}}$, $\text{SE}_{\text{O,out}}$, respectively); the reference electrodes (REs) were located in the other isolated chambers by a gasket, where the conditions of humidity, temperature and pressure were controlled and monitored. The reference electrodes were in contact with hydrogen to work as RHEs with stable potentials as long as the conditions of temperature, pressure and humidity are maintained constant, as shown in Figure 4-6 (iii). If these conditions are known, the real potentials versus the SHE can be calculated. A patch of the same catalyst as the anode was added to some of the sensing and reference electrodes to test the effect on their stability (see Figure 5-1 in Chapter 5 for the results).

(i)



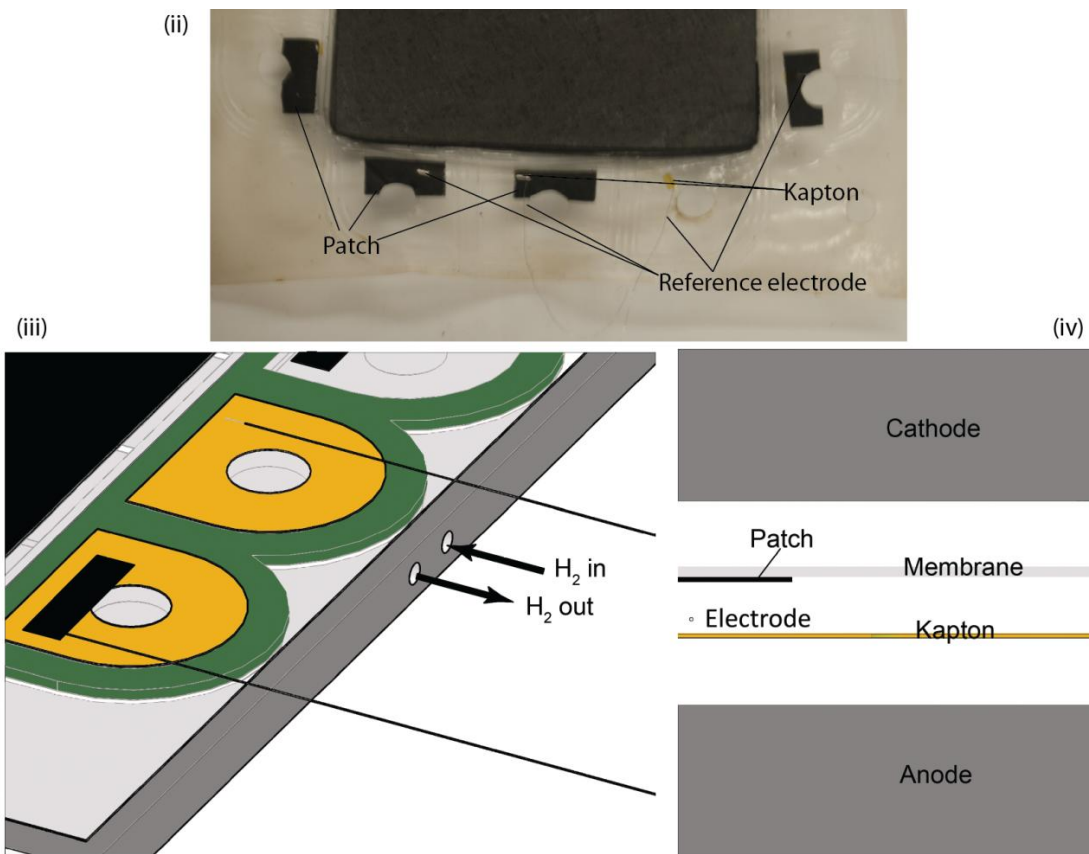


Figure 4-5 Placing of reference and sensing electrodes in isolated chambers.

The sensing electrodes were in contact with hydrogen or oxygen that entered and exited the cell through their respective ports. The electrodes were fixed in the chambers by placing them between a layer of Kapton[®] and the membrane, and then compressing the assembly to 120 psi, as shown in Figure 4-6 (ii and iv). These Kapton[®] layers prevented short-circuiting of the electrodes with the graphite plates. The patches were exposed to the conditions in the chamber. When only a wire was used as a sensing or reference electrode, the tip was exposed to the conditions. Our experimental results indicated that there was no change in the electrode potentials with positioning within the chambers. The potentials were recorded using a National Instruments PXI-6255 board and LabVIEW program. The reference electrodes and the sensing electrodes connections are described in Table 4-3 and shown in Figure 4-6.

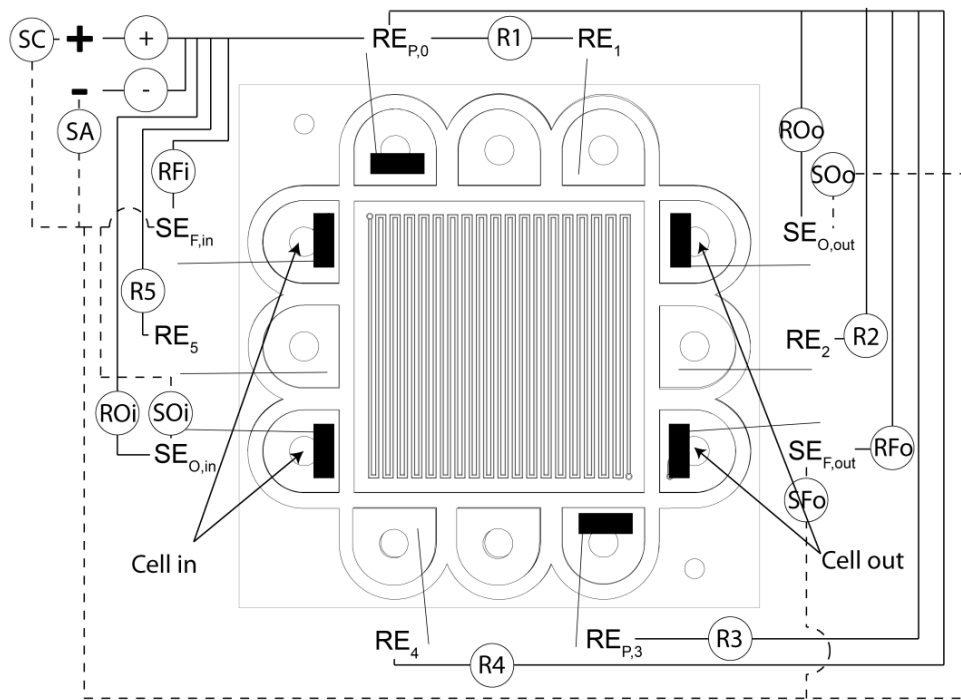


Figure 4-6 Potential connections of electrodes

Reference Potential	Measured Potential	Nomenclature
	Anode	+
	Cathode	-
	RE ₁	R1
	RE ₂	R2
	RE _{P,3}	R3
	RE ₄	R4
RE _{P,0}	RE ₅	R5
	SE _{F,in}	RFi
	SE _{F,out}	SFo
	SE _{O,in}	SOi
	SE _{O,out}	SOo
SE _{F,in}	Anode	SA
SE _{F,in}	Cathode	SC

Table 4-3 Nomenclature for potential connections of electrodes

4.2.1 Reference electrode potential correction

The reference electrode potentials were thermodynamically corrected for temperature, pressure and proton concentration using the Nernst equation as shown in equation (4-1). Ideal gas behavior was assumed for the conditions at which the experiment was carried out and p^0 and C^0 equal to 1.

$$E = E_T - \frac{RT}{nF} \ln \frac{p_{H_2}}{C_{H^+}^2} \quad (4-1)$$

where E_T is the temperature correction of the electrode potential, $C_{H^+}^2$ is the proton concentration, and p_{H_2} is the partial pressure of the hydrogen gas in the chamber.

In order to obtain the partial pressure of hydrogen, it is necessary to know the partial pressure of water vapor (p_w), as $p_{H_2} = P_{total} - p_w$, according to Dalton's law. The partial pressure of water vapor was calculated using Antoine's Equation (4-2). The constants for the dew point temperatures (T) of interest were obtained from the National Institute of Standards and Technology based on Bridgman and Aldrich data [182].

$$\log p_w = a - \frac{b}{T + c} \quad (4-2)$$

As the conditions for the reference electrodes were maintained constant, the proton concentration was assumed to be constant and calculated to be 1.586 mol/L based on the data provided by DuPont™ for fully hydrated Nafion® 115 (see Appendix A.6): equivalent weight of 1100, dry weight of 250 gm⁻², and a thickness of 0.127 mm. This value was used for Chapter 5 and Chapter 6. After the publication of the papers in 2008 and 2009, Spry and Frayer published the first measurement of the surface proton concentration of Nafion®, in 2009 [183]. They found that $[H^+] = 0.54$ M for fully saturated Nafion® and $[H^+] = 0.95$ M for dehydrated Nafion® membranes by using pyrene derivative photoacids and compared the results to HCl kinetics. The reference electrode potentials were corrected by substituting the calculated values for proton concentration, the hydrogen partial pressure, and the temperature into Equation (4-1).

4.2.2 High frequency resistance measurements

The high frequency resistances were measured by a Solartron 1250 Frequency Response Analyzer (frequencies of 1-100 kHz) to find the right frequency to use a GwINSTEK LCR-821 impedance meter at a constant frequency. The chosen frequency was 1 kHz. The resistances were measured between the anode and the cathode, anode against the reference electrode, and cathode against the reference electrode.

Previous works have shown that misalignment of electrodes [120, 166, 184] and even water concentration gradients through the membrane can affect the impedance measurements [164]. Both effects were reduced by locating the reference electrodes more than 10x the thickness of the membrane away from the active area and by humidifying both sides of the membrane where the reference electrode was located. The resistance measured between the reference electrode and the cathode includes the membrane resistance (B to P) as shown in Figure 4-7. The potential lines, created by the anode and cathode, remain constant all the way to P (where there reference electrode measurement is done).

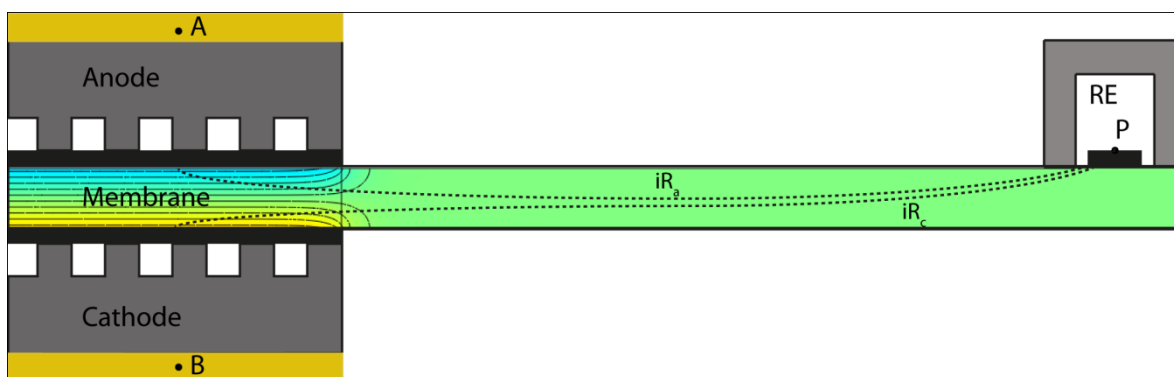


Figure 4-7 Reference electrode HFR measurements from node A to B and node B and P. The drawing is not to scale, but the potential line calculations remain constant up to the reference electrode as can be seen.

5 SENSING ELECTRODES FOR FAILURE DIAGNOSTICS IN FUEL CELLS⁴

5.1 INTRODUCTION

The durability and reliability of fuel cell products need to be improved. The lack of early diagnosis and failure-prevention techniques is one of the limiting factors. In this chapter, a non invasive method for the early diagnosis of flooding, dehydration and low fuel stoichiometry is presented. The method is based on micro sensing electrodes (SE) that are placed at appropriate locations in a single cell. These electrodes have a characteristic potential response to each of the failure modes, which enables detection prior to overall fuel cell failure. The specific features in the measured responses (or combinations thereof) can be used to discern between different failure modes, and initiate corrective actions.

5.2 RESULTS AND DISCUSSION

To test the stability of the electrodes, the fuel cell was operated at 3 different current densities (100, 500, and 800 mAcm⁻²) and at open circuit voltage for more than 10 hours (2h at each setting), as shown in Figure 5-1. The response of the sensing electrodes at normal conditions depended only on the operating point of the fuel cell without adding any noise, demonstrating their reliability and stability.

⁴ A version of Chapter 5 has been published. Herrera, O., W. Mérida, and D.P. Wilkinson, *Sensing electrodes for failure diagnostics in fuel cells*. Journal of Power Sources, 2009. **190**(1): p. 103-109.

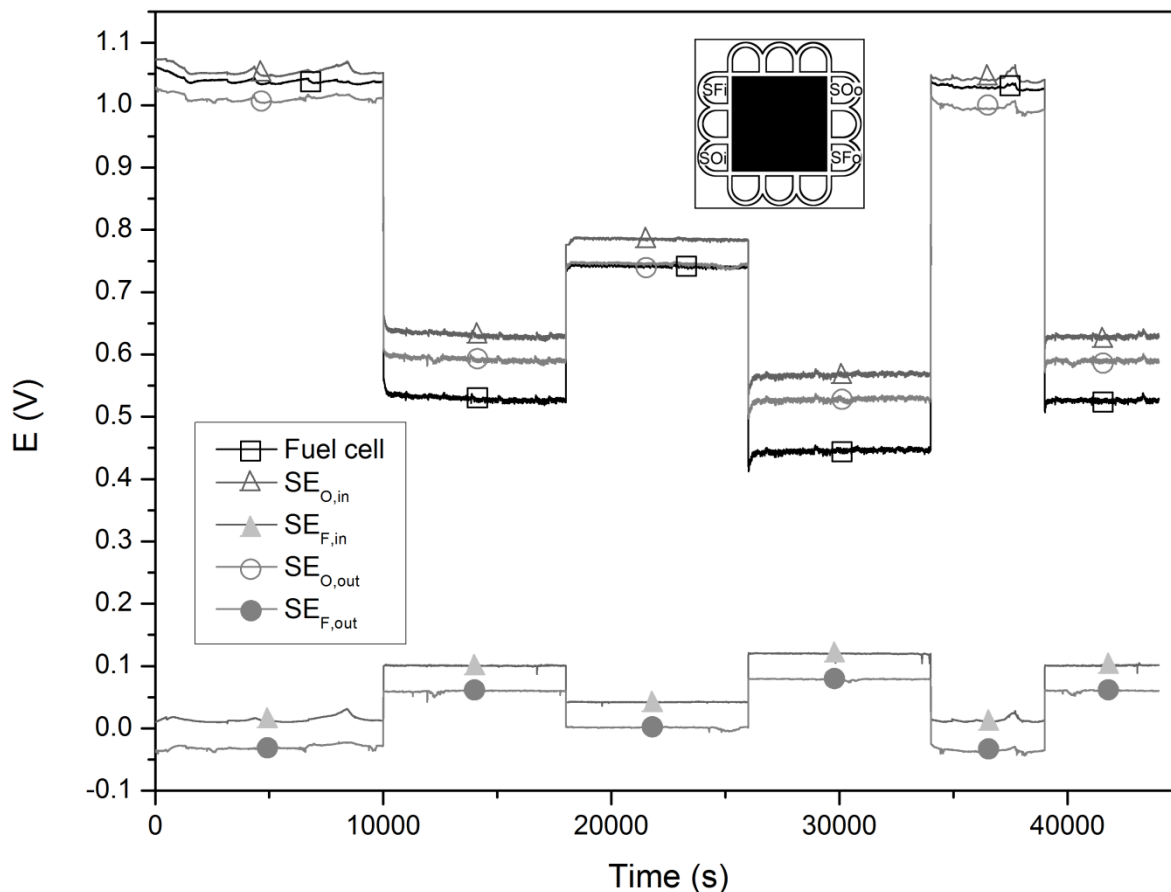


Figure 5-1 Stability of sensing electrodes in a fully humidified fuel cell at different current densities for more than 10 hours.

The potential response and standard deviations of the Cathode vs. the SEs at different conditions (normal, dehydration and flooding) are shown in Figure 5-2. For dehydration, the humidification was bypassed, an approximate RH of 4% was the lowest achieved. For flooding, the gas temperature (GST) was set at 75 °C and the DPT was set to 90 °C. In both cases the system ran for 1 hour at 500 mAcm⁻² at the given conditions of flooding and dehydration before recording the polarization curve points. Figure 5-2 shows the effect of relative humidity on the SE_{in} and the SE_{out}. The SE_{in} local conditions change the most for both the fuel and oxidant electrodes, affecting the potential response of the electrode. The anode vs. SE_{out} potential response has less than a 10 mV difference between points. The local conditions for that electrode do not vary during the experiment

because the fuel cell produces enough water to keep the exit conditions almost constant. The anode and cathode vs. SE_{in} change significantly with relative humidity. The anode vs. the SE_{in} changes less than the cathode vs. the SE_{in} , likely because as the membrane/ionomer dries, the proton concentration is reduced limiting the oxygen reduction reaction.

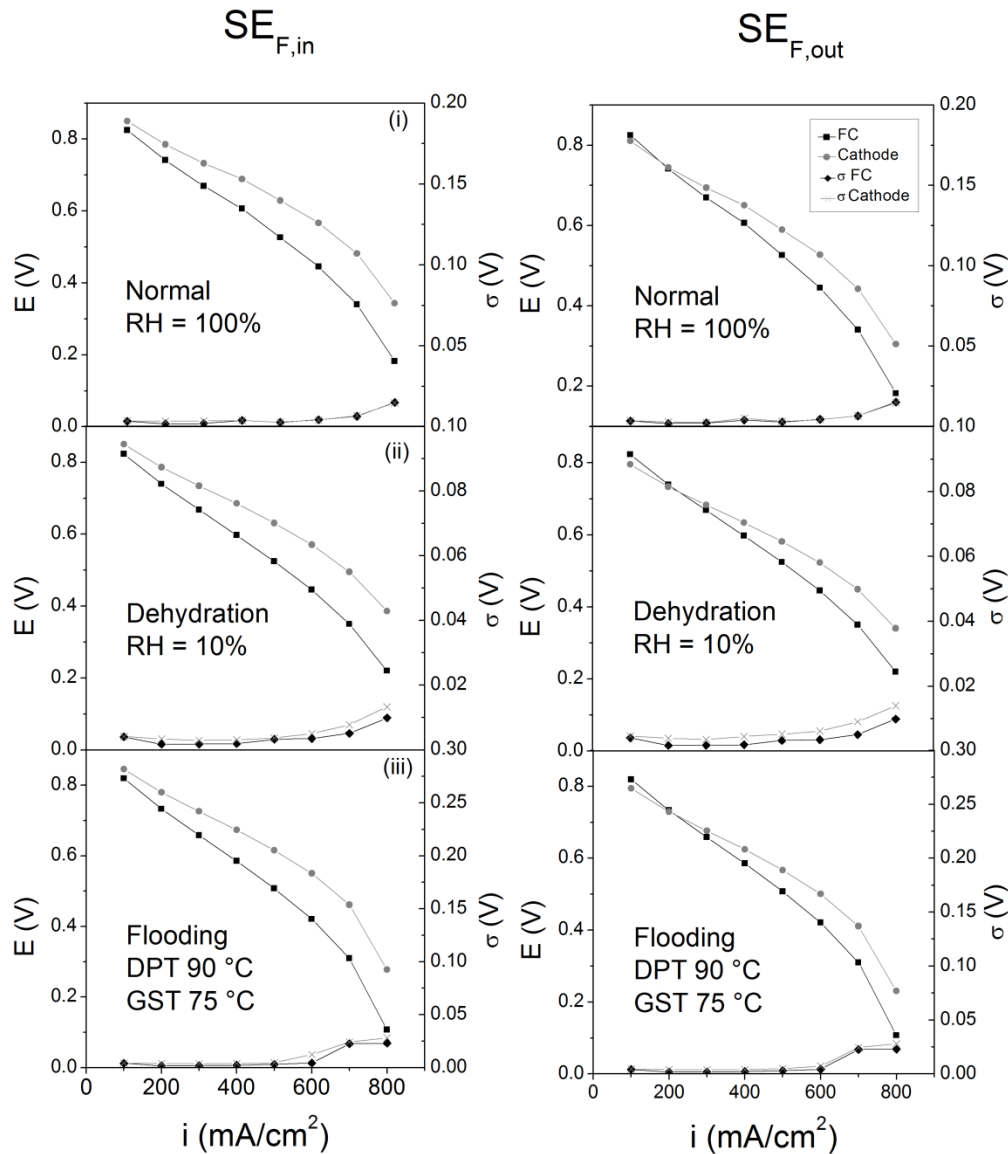


Figure 5-2 Potential responses and standard deviation of $SE_{F,in}$ and $SE_{F,out}$ at different conditions: normal (i), dehydration (ii), and flooding (iii).

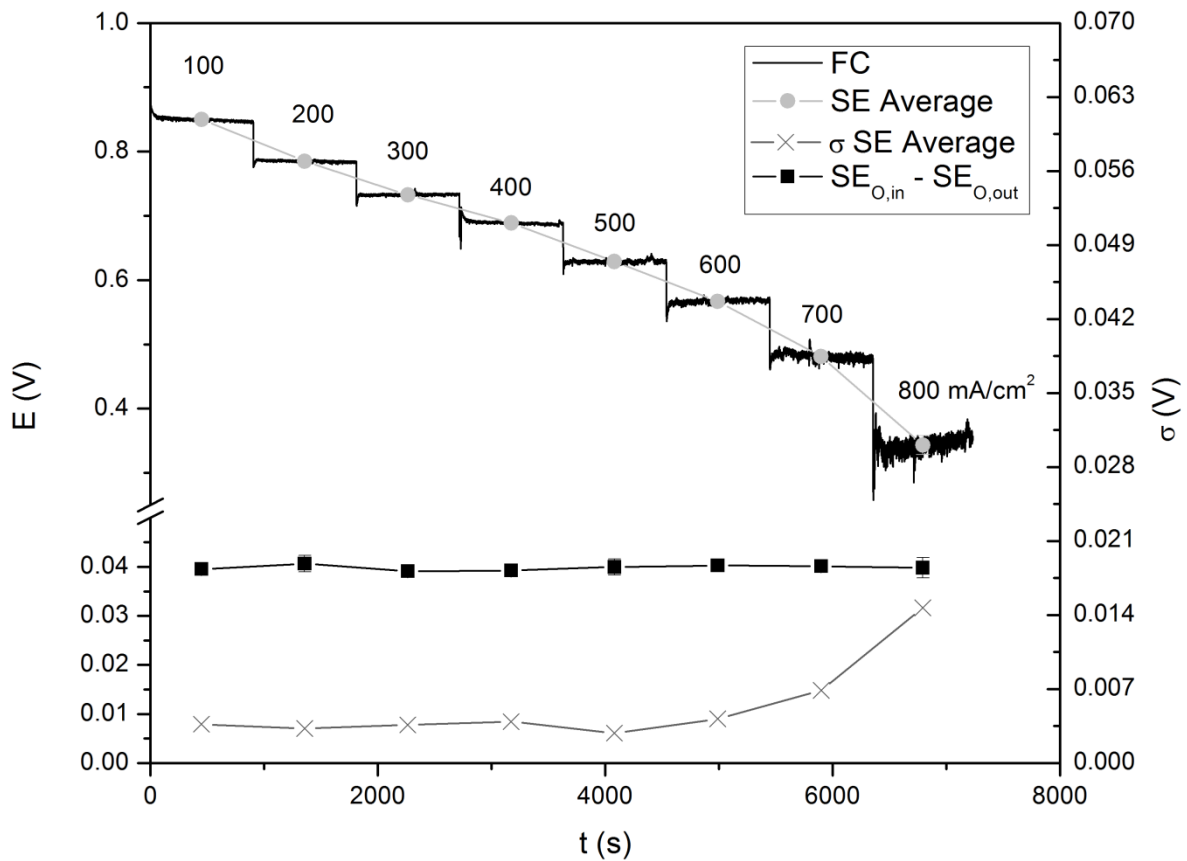


Figure 5-3 General treatment of the data obtained with SEs. The average and standard deviation of the data for at least 15 minutes per point was calculated. Also, the potential difference between SE_{in} and SE_{out}, on the cathode, is shown.

The potential difference between the SE_{in} and the SE_{out} was also constant at normal conditions, as shown in Figure 5-3. In this figure, the general treatment of the data is also shown. Each point on a voltage plateau is an average taken over at least 15 minutes at a given condition. The standard deviation for each point was also calculated and shown in Figure 5-2. These average potential responses and standard deviations are different during different operating conditions. During normal conditions, the standard deviations from the SEs and from the fuel cell are very similar. When a failure is induced, the standard deviations of the cathode vs. the SEs are larger than the standard deviation associated with the average cell voltage and depending on the failure; the standard deviation is smaller or larger.

As can be seen in Figure 5-4, the drying effects are irreversible and lead to hysteresis. After a 15 hour experiment where the dew point temperature was reduced 5 °C every 30 min down to a minimum of 5% RH and then increased at the same rate to the original level, the final fuel cell potential decreased by more than 20 mV over the experimental current density range. However, the fuel cell potential alone is not enough to diagnose the lack of humidification until it is too late. By using sensing electrodes in the inlet and outlet of the fuel side, the local effects of the dehydration are more evident. There are larger potential losses on the $SE_{F,in}$ than at the $SE_{F,out}$. Therefore, to diagnose dehydration, only the $SE_{F,in}$ is needed. However, this is only true for flow field geometries that create low humidity levels at the beginning of the active area, i.e., flow fields that are not in a cross-flow configuration or flow fields that are not in a counter-flow configuration. Flow fields with a cross-flow configuration have a 90° rotation between the anode and the cathode. Usually, the anode inlet is not where the cathode inlet is. For this thesis, the cathode inlet was at the end of the channel from the anode inlet. The cathode would humidify the anode inlet as the cathode would have been producing water from beginning to end with a rotation. In flow fields with a counter-flow configuration, the anode inlet is where the cathode outlet is and thus, the anode is well humidified as the cathode would have been producing and carrying water from beginning to end. Therefore, a better method to diagnose and ultimately prevent this failure is the potential difference between the sensing electrodes, SE_{in} and the SE_{out} can be used, as shown in Figure 5-4.

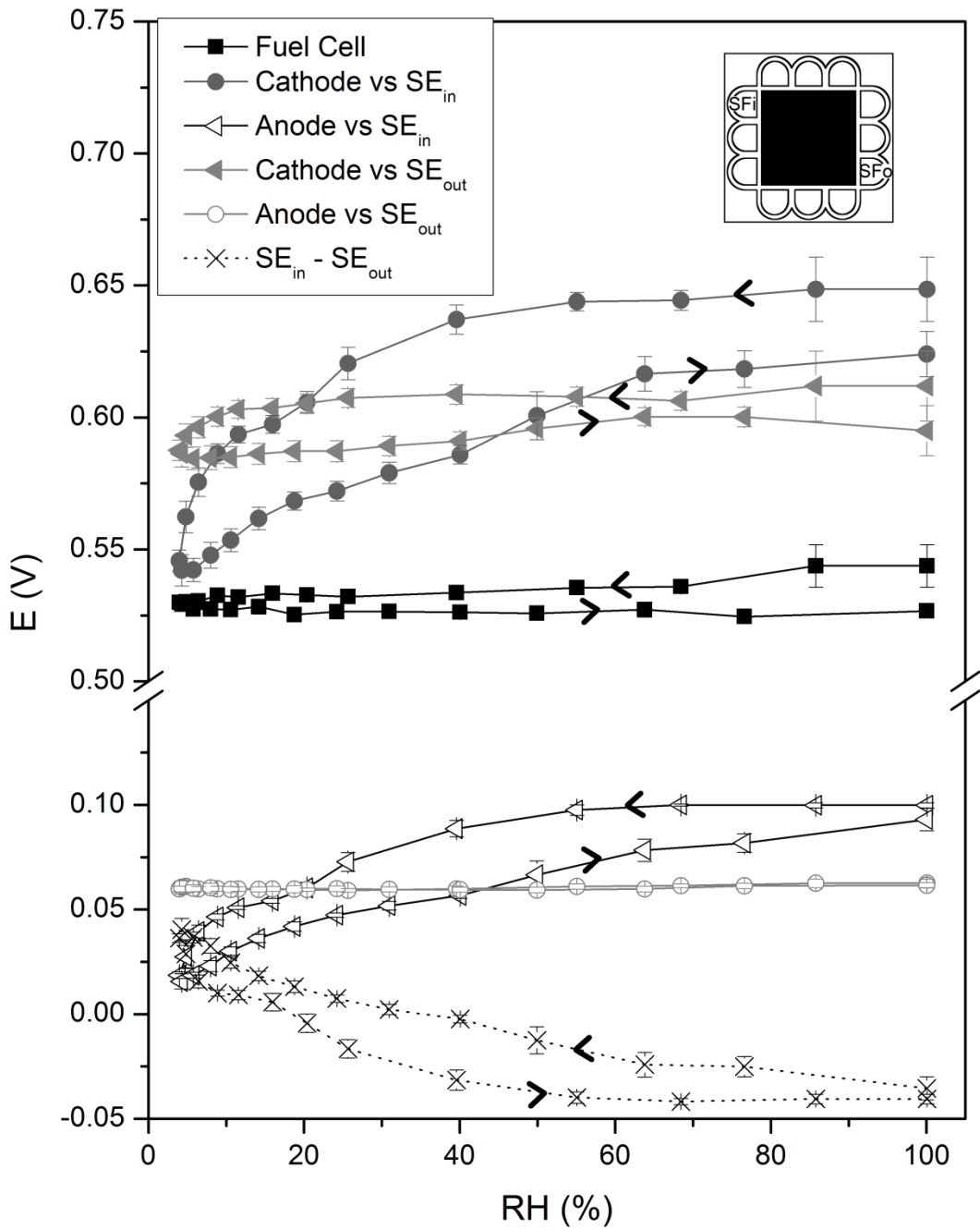


Figure 5-4 Potential response of SE_{in} and SE_{out} at different RH at a current density of 500 mAcm⁻². The RH is gradually reduced to a minimum of 5 % and then back to 100 %. Each point is an average over 30 minutes.

In Figure 5-5, the potential response to flooding of the $SE_{in} - SE_{out}$ is shown. In addition, the dew point temperature and the pressure difference between the inlet and outlet of the anode and the cathode are displayed. Flooding can also be diagnosed by the pressure difference between the anode inlet and the anode outlet. The $SE_{in} - SE_{out}$ shows that the potential oscillates with higher response when only the cathode is flooded, but the pressure fluctuation is not as significant as in the other case. In general, pressure difference monitoring is not as sensitive a diagnostic tool as the precise voltage monitoring from the SEs, unless the pressure sensors have a higher resolution than 0.1 psi (like the ones used in this study), which increases cost. The temperature resolution is 0.2 degrees and the voltage resolution is 10^{-6} V.

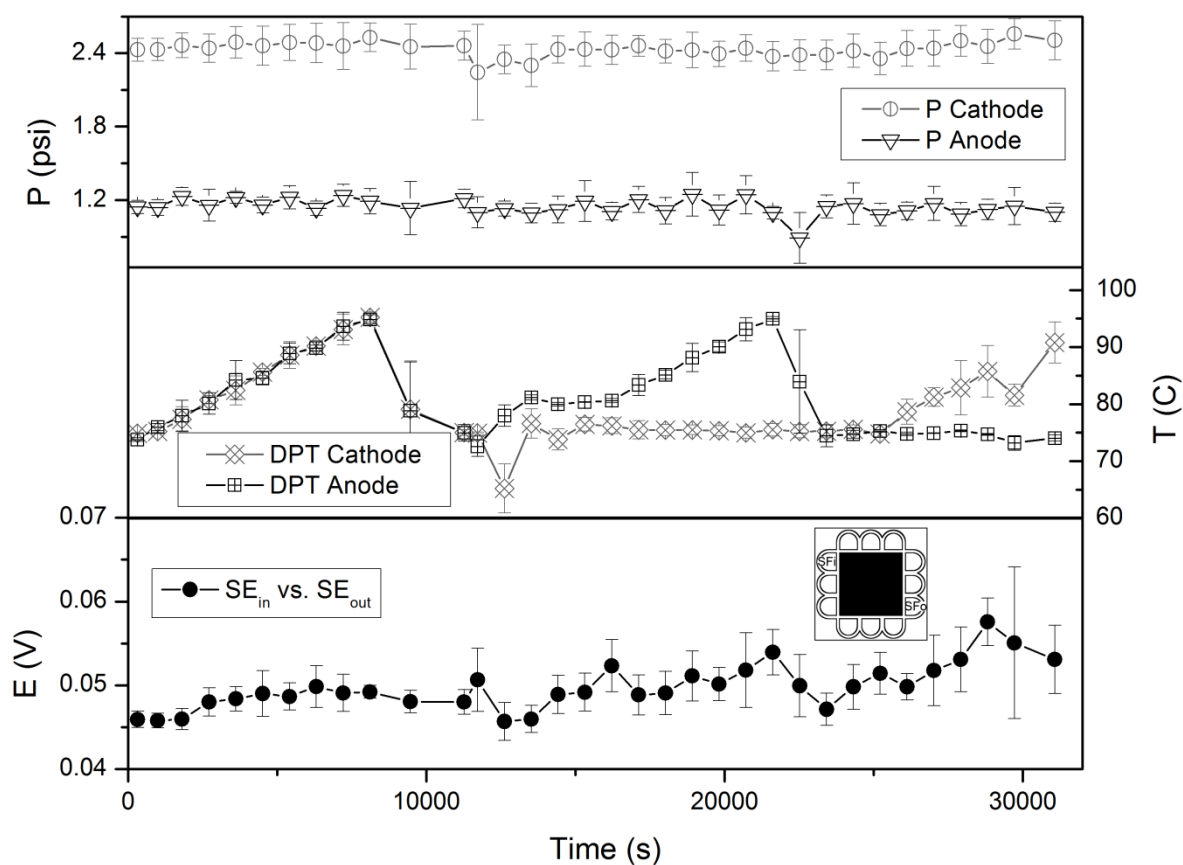


Figure 5-5 Potential response SE_{in} vs. SE_{out} during flooding conditions at a current density of 500 mAcm^{-2} . The pressure differences between the inlet and the outlet of both the anode and the cathode confirm the potential response results. Each point is an average of 30 minutes.

For low fuel stoichiometry, the faster potential response is even more evident as shown in Figure 5-6. The faster response of the SEs is due to their need for hydrogen to operate. The SE_{in} changes the most as the local conditions in that chamber are the first to be affected. It takes a change of stoichiometry of 0.03 from 1.15 to 1.12, in this case, more than one and a half hours, for the fuel cell to show a noticeable change in potential. The standard deviation is also constant until the potential change occurs. This failure is one of the most damaging ones, as the potential drops to zero as soon as there is a lack of hydrogen. If the lack of hydrogen persists, it can lead to fuel cell reversal (production of hydrogen with power consumption instead of consumption hydrogen and power generation). If the failure continues, the catalyst can be corroded and even the graphite plates can be damaged.

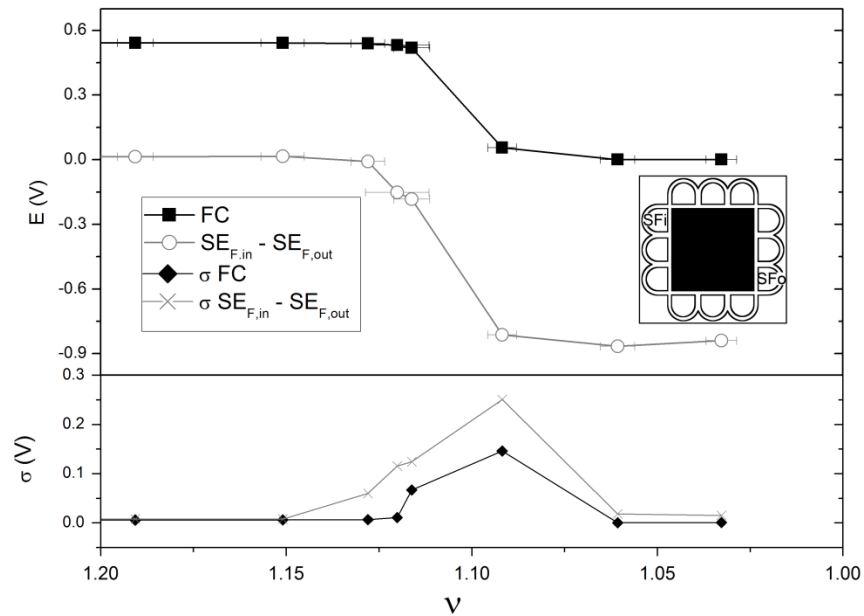


Figure 5-6 Potential response of SE_{in} vs. E_{out} to gradual reduction of fuel stoichiometry at a current density of 500 mAcm^{-2} . This potential difference shows an earlier response than the fuel cell. Each point is an average of 30 minutes.

The SEs can prevent permanent damage to the fuel cell by diagnosing the failure before it affects the fuel cell, and providing sufficient time for corrective measures (at least 30 minutes according to these results). If the potential of the SE_{in} vs. SE_{out} (E) is

divided by the electrode potential difference at normal conditions (E^0 , $t = 0$), the SEs diagnosis can be done in 5 minutes for this experimental setup. It only requires averages of 100s of data points where the standard deviation is also calculated to corroborate the diagnosis. Figure 5-7 illustrates the effects of low fuel stoichiometry, dehydration, and flooding. If the potential difference between the SE_{in} and the SE_{out} is considerably negative with a high σ , then there is low fuel stoichiometry. If the potential difference between the SE_{in} and the SE_{out} is negative and the σ is practically constant, then there is drying. For flooding, the potential difference has to be positive and show peaks and the standard deviation (σ) must also present positive peaks. This information can be easily incorporated into the logic of a real time diagnosis system. The faster response of the sensing electrodes to the different failure modes can also be seen on the repetition of the experiments for flooding (Figure 5-8), dehydration (Figure 5-9), and low stoichiometry (Figure 5-10). The standard deviation, in this case, represents the change of the potential response from experimental run to other experimental run(s). The standard deviations of the different experimental runs show good response and reproducibility of the sensing electrodes. Two or more undesired conditions at the same time were not tested. However, based on the characteristic responses of the sensing electrodes in combination with the standard deviations, it is possible to speculate that the identification of the individual failure modes can be achieved even if two or more failure conditions are affecting the cell.

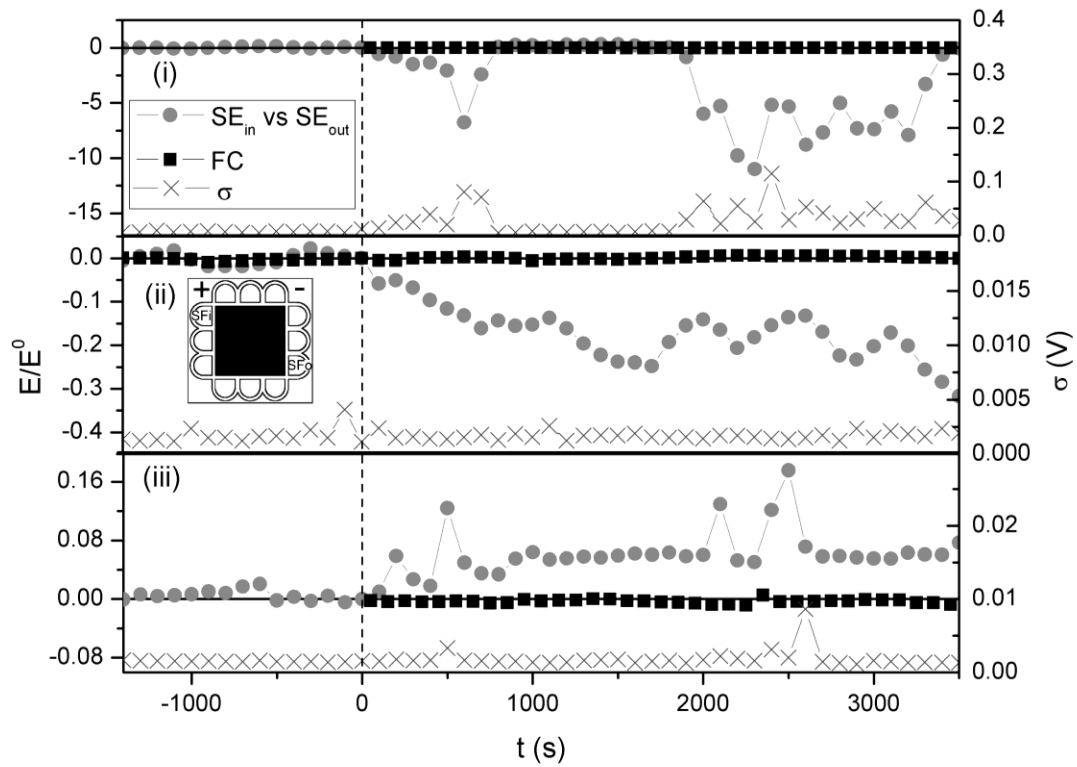


Figure 5-7 Characteristic response under simulated low fuel stoichiometry (i), drying (ii) and flooding (iii) at a current density of 500 mAcm^{-2} . Time 0 is when the undesired conditions are detected by the SEs ($v=1.15$, $\text{RH} < 60 \%$, and dew point temperature 5° higher than the cell temperature). The fuel cell potential shows little variation while the potential difference between SE_{in} and SE_{out} is changing.

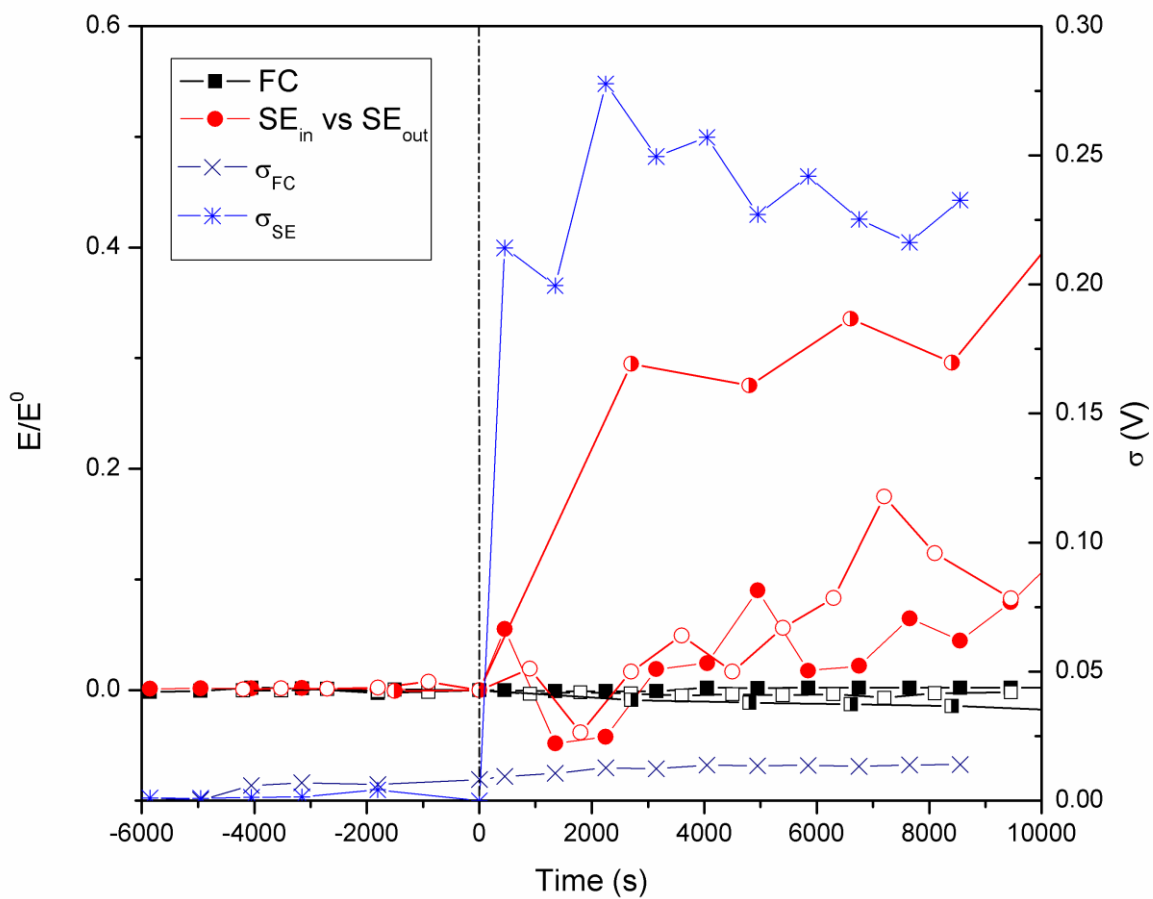


Figure 5-8 Early potential response of sensing electrodes to flooding conditions. Time 0 is when the undesired conditions are detected by the SEs (dew point temperature 5° higher than the cell temperature). The fuel cell potential shows little variation while the potential difference between SE_{in} and SE_{out} is changing. The standard deviations of the different experimental runs show good response and reproducibility of the sensing electrodes.

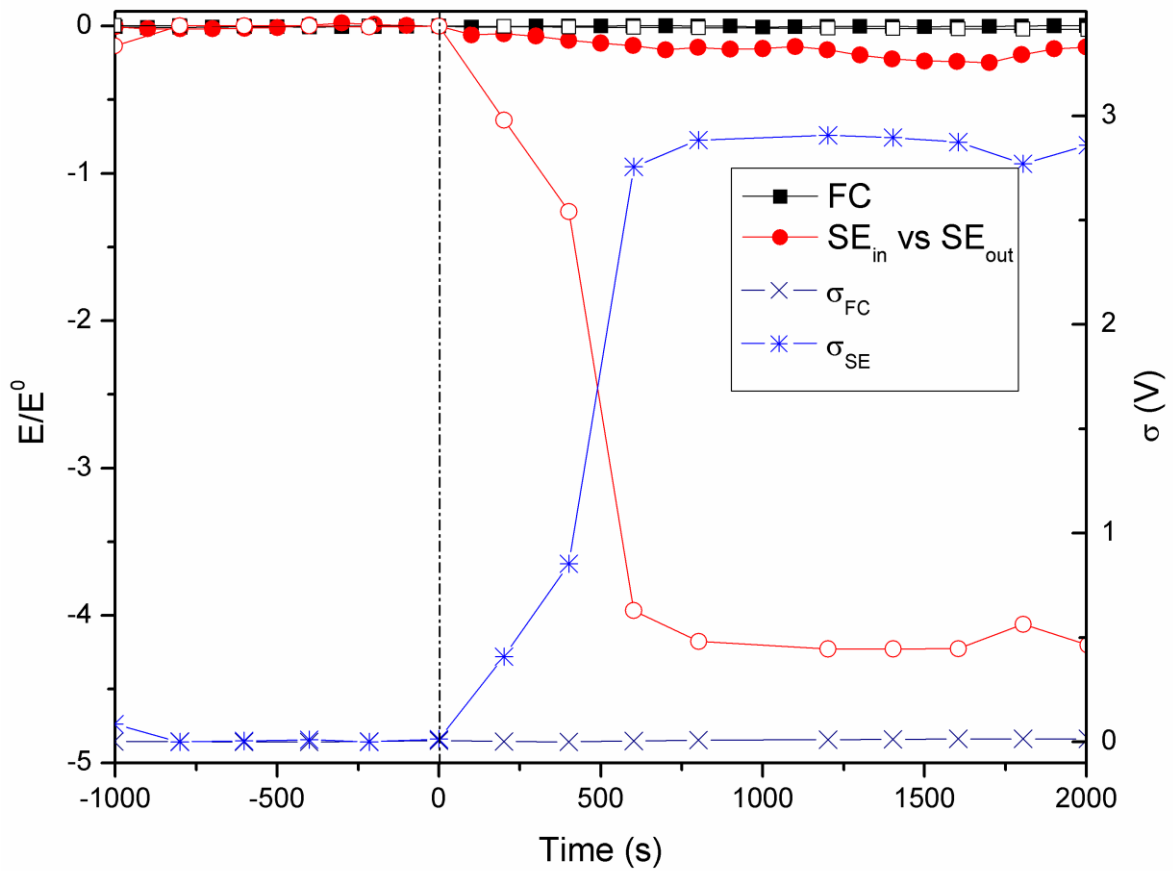


Figure 5-9 Early potential response of the sensing electrodes to drying conditions. Time 0 is when the undesired conditions are detected by the SEs ($RH < 60$). The fuel cell potential shows little variation while the potential difference between SE_{in} and SE_{out} is changing. The standard deviations of the different experimental runs show good response and reproducibility of the sensing electrodes.

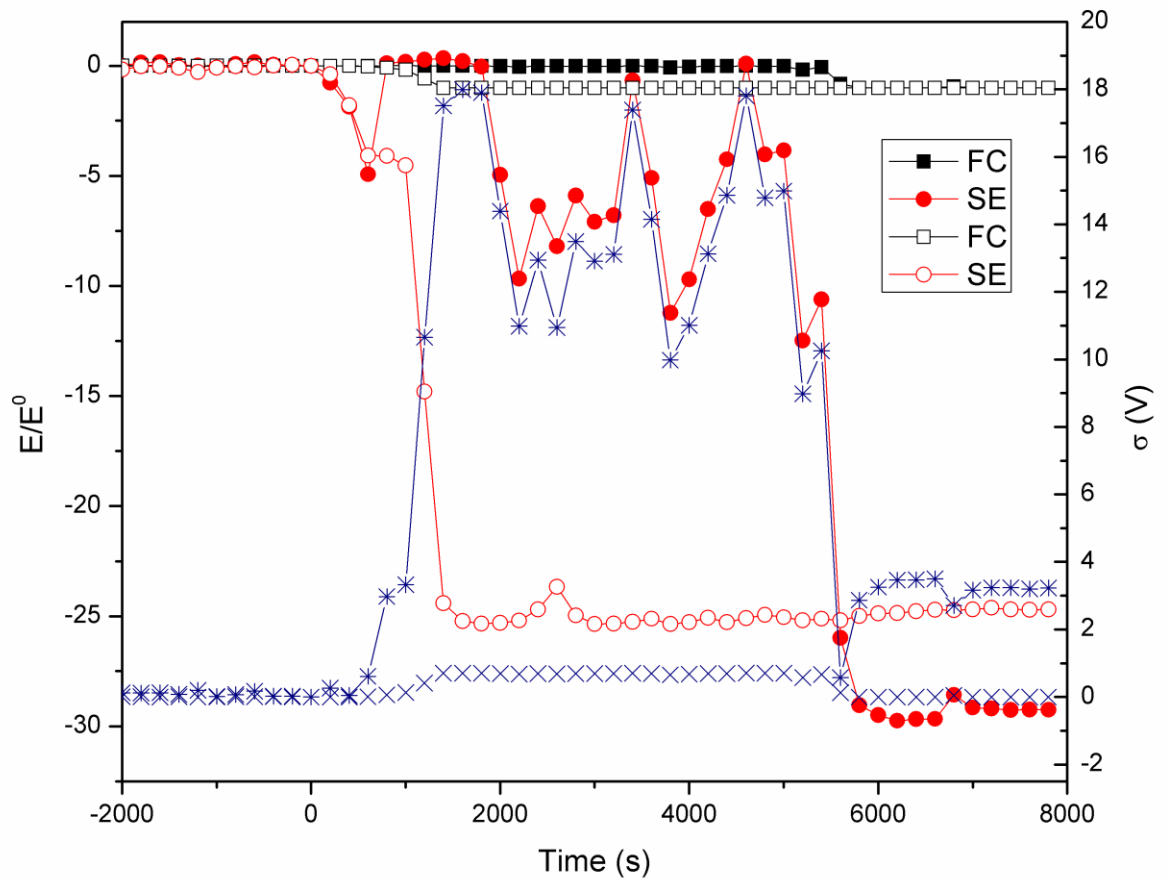


Figure 5-10 Early potential response of the sensing electrodes to low stoichiometric flows. Time 0 is when the undesired conditions are detected by the SEs ($\nu=1.15$). The fuel cell potential shows little variation while the potential difference between SE_{in} and SE_{out} is changing. The standard deviations of the different experimental runs show good response and reproducibility of the sensing electrodes.

5.3 SUMMARY

In this Chapter three examples were examined: flooding, dehydration and low fuel stoichiometry. Each failure mode had a characteristic potential response based on sensing electrode measurements prior to any changes in the overall cell voltage. Sensing electrodes can be used for early detection of many different types of failure modes. The SEs are sensitive to the local cell conditions, so their positioning in the cell is important. If the local conditions for the sensing electrode change with respect to the fuel cell operating conditions and have an associated failure mode, the sensing electrodes will have a potential response characteristic to that failure.

These electrodes can also be used as a quasi-reference to determine the anodic and cathodic contributions in a fuel cell, as well. In order for these sensing electrodes to act as a real reference electrode, the resistances need to be taken into account and the conditions for the electrode need to be kept constant.

6 NEW REFERENCE ELECTRODE APPROACH FOR FUEL CELL PERFORMANCE EVALUATION⁵

6.1 INTRODUCTION

The separation of anodic and cathodic potentials in a working fuel cell via reference electrodes at constant conditions is reported in this section. The reference electrodes consisted of four platinized platinum electrode wires and two patches of the same catalyst layer used in the anode. All the reference electrodes were unaffected by the operating conditions of the fuel cell and those with patches provided the most stable potentials ($\sigma = 0.005$ V for patch and $\sigma = 0.010$ V for platinized wire). Additional sensing electrodes were placed at the fuel and oxidant inlet and outlet to provide localized information on the operating conditions and the state of the MEA.

6.2 RESULTS AND DISCUSSION

The stability of sensing electrodes was tested at different conditions of humidity as shown in Figure 6-1. The potential differences are all versus the reference electrode RE_{P,0} that is located in a chamber near the fuel inlet chamber (see Figure 4-1 and Figure 4-2). The sensing electrodes potentials change with the different environmental conditions, while the reference electrodes potentials remain constant. However, the oscillations are greater for those reference electrodes without a catalyst patch. The catalyst patch reduces dimensional change/wrinkling of the membrane and decreases the contact resistance, improving the potential response of the reference electrodes.

⁵ A version of Chapter 6 has been published. Herrera, O.E., W. Merida, and D.P. Wilkinson, New Reference Electrode Approach for Fuel Cell Performance Evaluation. ECS Transactions, 2008. 16(2): p. 1915-1926.

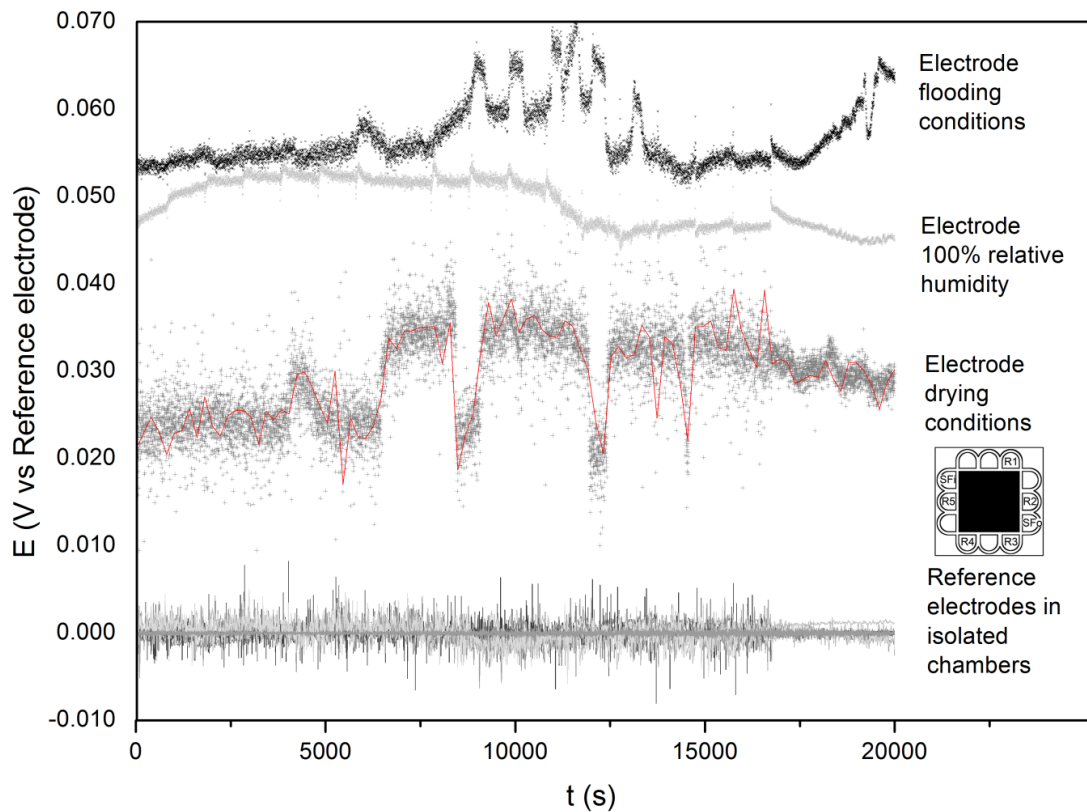


Figure 6-1 Stability of sensing electrodes at different humidity conditions and the reference electrodes at constant conditions.

The average potential from all the reference electrodes was used to acquire the anodic and cathodic potentials. In Figure 6-2 the anode, cathode and fuel cell polarizations at different humidity conditions are shown (i.e., normal, flooding and dehydration conditions). These polarization curves show the average potential values at different current densities. At normal conditions, the potential of the anode increases constantly with the same slope. When flooding is induced, the potential of the anode changes slope at around 600 mAcm^{-2} , due to reduced mass transport. During dehydration, the overpotential of the anode and cathode increases significantly due to higher resistance and reduced mass transport, as will be described in Chapter 7. The limiting cell current density is achieved at 1200 mAcm^{-2} , less than when operating at normal or flooding conditions ($1300 - 1350 \text{ mAcm}^{-2}$). The cell and electrode polarization results using a

reference electrode provide useful spatially averaged performance information, but not localized information.

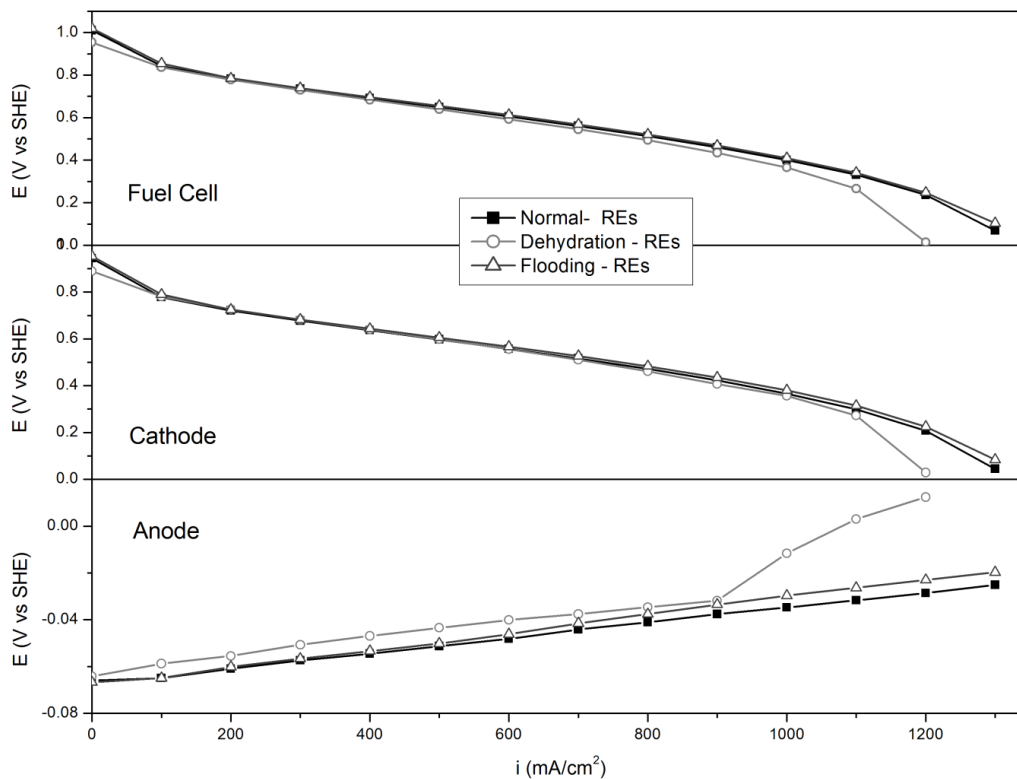


Figure 6-2 Anodic, cathodic and fuel cell potentials at different humidity conditions and current densities.

In Figure 6-3, where the relative humidity (RH) is reduced from 100 % to around 5 % and then increased back to 100 %, the standard deviation of the reference electrodes without a patch increases after being subject to the failure mode. Even though the potential can oscillate, the average potential of the reference electrodes is within a 5 mV range. The sensing electrode overpotential increases as the membrane is dehydrated. This occurs because as the membrane is dehydrated, the ionic and contact resistances increase. As the dew point temperature (DPT) changes, the hydrogen partial pressure changes (i.e., the hydrogen partial pressure is the difference between the total pressure minus the partial pressure of the water vapor, as established by Dalton's law), affecting the sensing electrodes potential. The dehydration effects are irreversible and even after rehydration

the ionic and contact resistances remain high, leading to higher overpotentials of the sensing electrodes and higher standard deviation (σ). It is clear that dehydration affects both the sensing electrodes and the reference electrodes without a catalyst patch. However, the sensing electrodes would be even more sensitive to the dehydration effects if no catalyst patch was present, as shown in Chapter 5, as the patches improve the contact resistances and retain moisture.

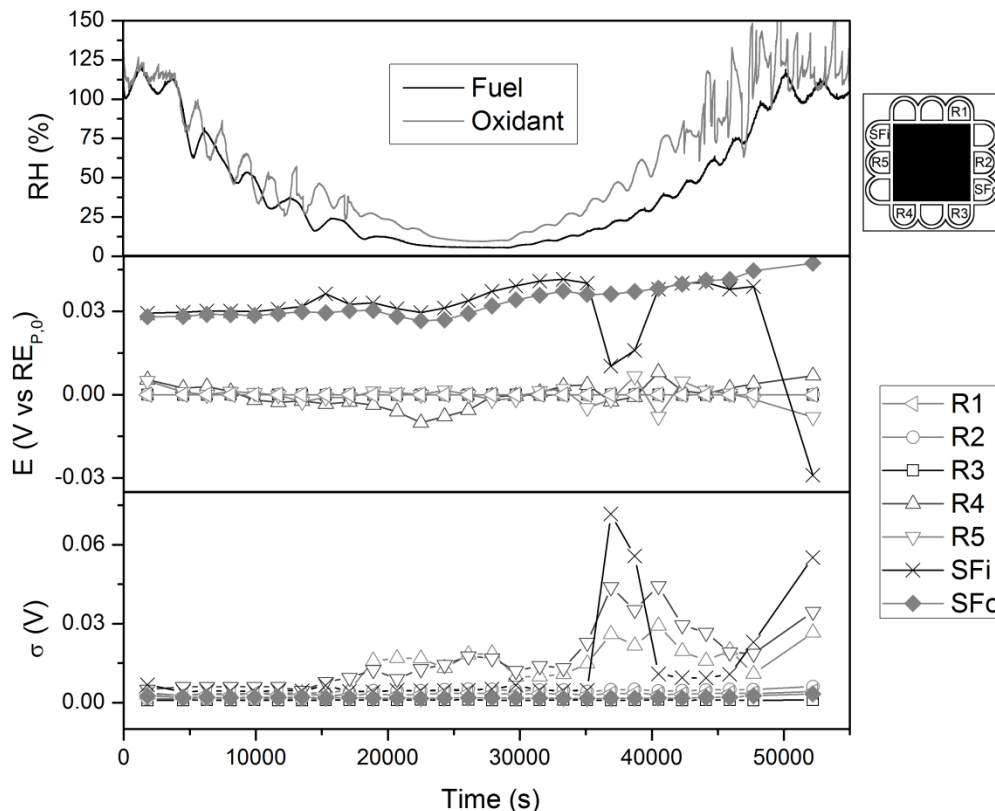


Figure 6-3 Effects of dehydration over the different electrodes. RH was reduced to 4% and then increased to 100% at a constant current of 500 mAcm^{-2} .

In Figure 6-4 the potential response of the reference electrodes and the sensing electrodes to a change of dew point temperature (DPT) from normal conditions (348 K) to flooding conditions (368 K) is shown. The current density was maintained constant at 1000 mAcm^{-2} , a current density close to the mass transport region (where flooding is more prominent). During flooding conditions the potential response of the sensing

electrodes and the reference electrodes do not change but the standard deviation of the potentials recorded increases significantly for some electrodes. The only reference electrode that changed (R1) was because it is the one closest to the oxidant and that's where the temperature gradients are the largest because of the water content. The effect of flooding (temperature and pressure change) is more noticeable with the sensing electrode placed at the fuel outlet ($SE_{F,out}$) and at the oxidant outlet ($SE_{O,out}$, not shown here) and also with the reference electrodes that have no patch. This is mostly due to the change of temperature that the liquid water creates. It was observed that a temperature difference across the membrane can generate wrinkles, altering the contact resistance of the electrodes and making the potential less stable. This could be corrected by adding a spring the sensing electrode.

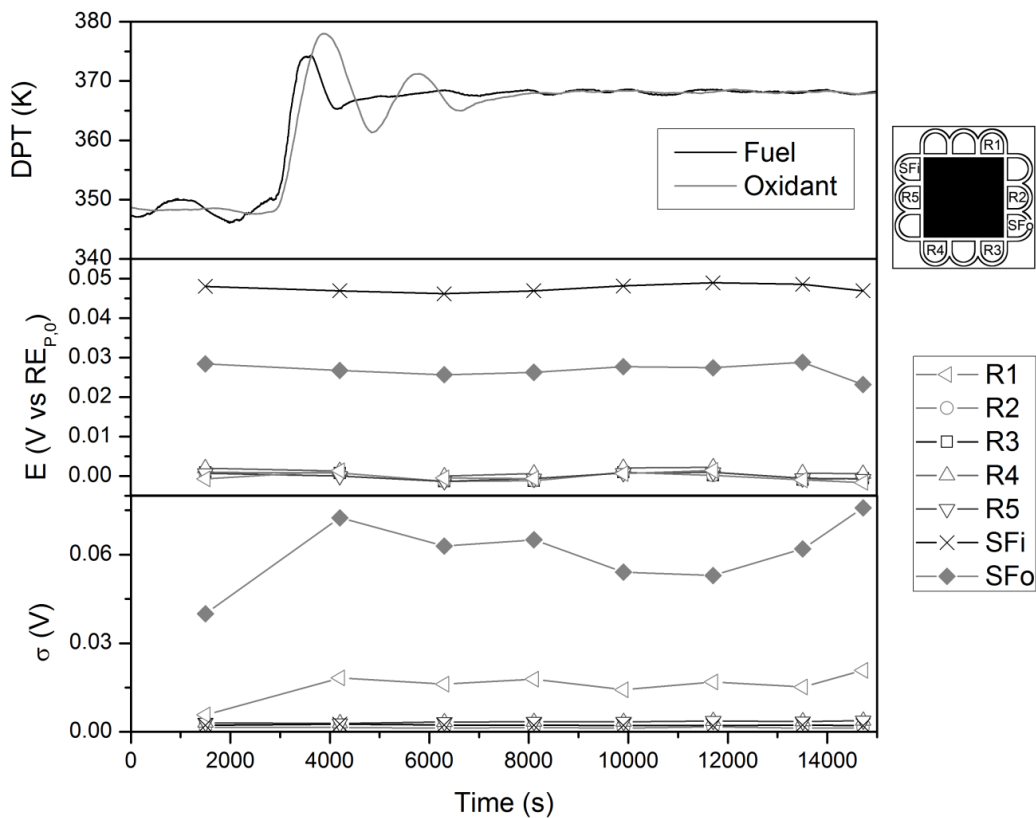


Figure 6-4 Reference electrode and sensing electrode response to flooding conditions at 1000 mAcm^{-2} . The DPT was increased from 348 K to 368 K, increasing the potential oscillations of the sensing electrodes.

In Figure 6-5(i), the oxidant flow rate is reduced from a stoichiometry of 2 to 1.05. If the oxidant flow rate is reduced sufficiently, the cathode potential decreases, decreasing the overall fuel cell potential, while the anode potential remains constant as shown in Figure 6-5(ii) for a current density of 1000 mAcm^{-2} . Figure 6-5(iii) shows the average voltage value at each stoichiometric point while Figure 6-5(iv) shows the potential difference ($\Delta\mu$) between the potential at different stoichiometric values (μ_T) and the normal stoichiometry of 2 (μ_0). With this data treatment, it is clear how the potential of the sensing electrode changes before any change in the anode, cathode and cell potential.

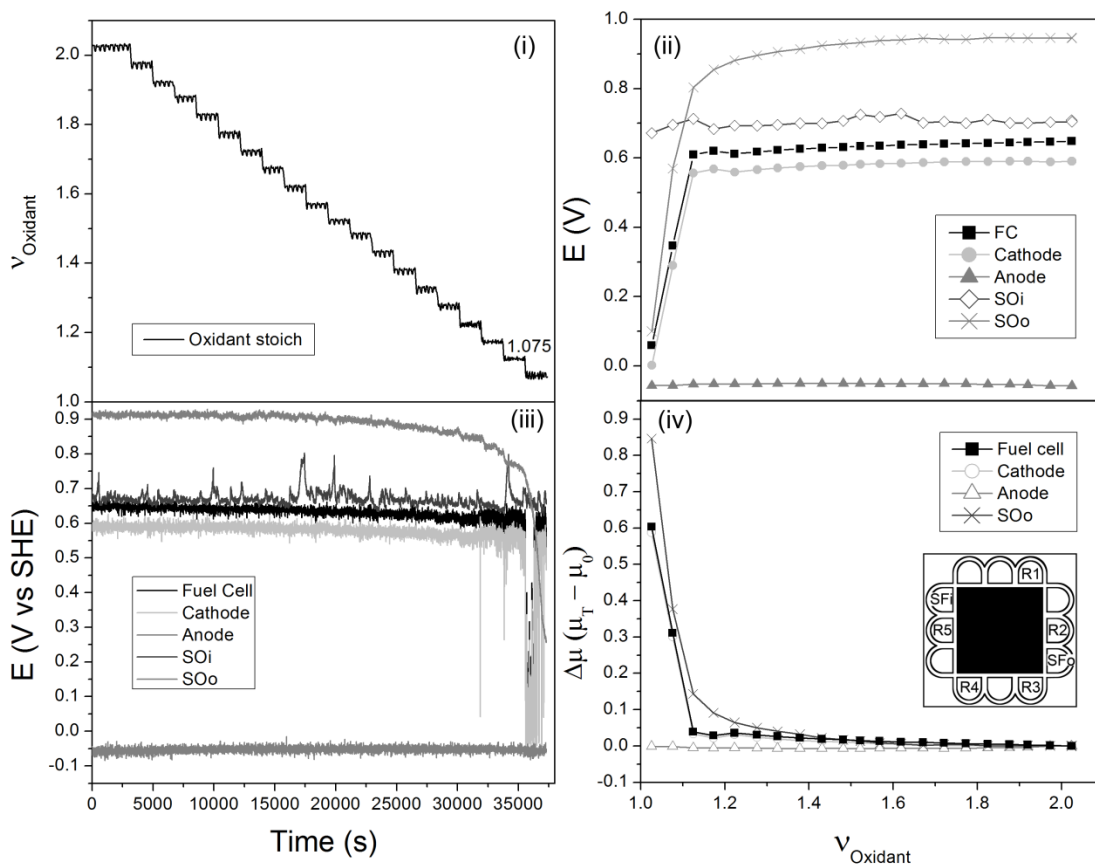


Figure 6-5 Potential response of the anode, cathode, fuel cell and the sensing electrodes (SEO,out, SEO,in) to low oxidant stoichiometry at 500 mAcm^{-2} : (i) oxidant stoichiometry as a function of time, (ii) voltage response as a function of time, (iii) voltage response at each stoichiometric point, and (iv) potential difference between stoichiometry at normal conditions ($v_c = 2$) and different stoichiometric values.

If the fuel flow rate is reduced enough, the anode overpotential increases as there is not sufficient hydrogen to react, as shown in Figure 6-6 (i). The potential of the cathode also decreases because there are insufficient protons for the oxygen to react. The sensing electrode placed at the fuel outlet is the most sensitive to the low fuel stoichiometry as the hydrogen depletes first at this end of the flow-field.

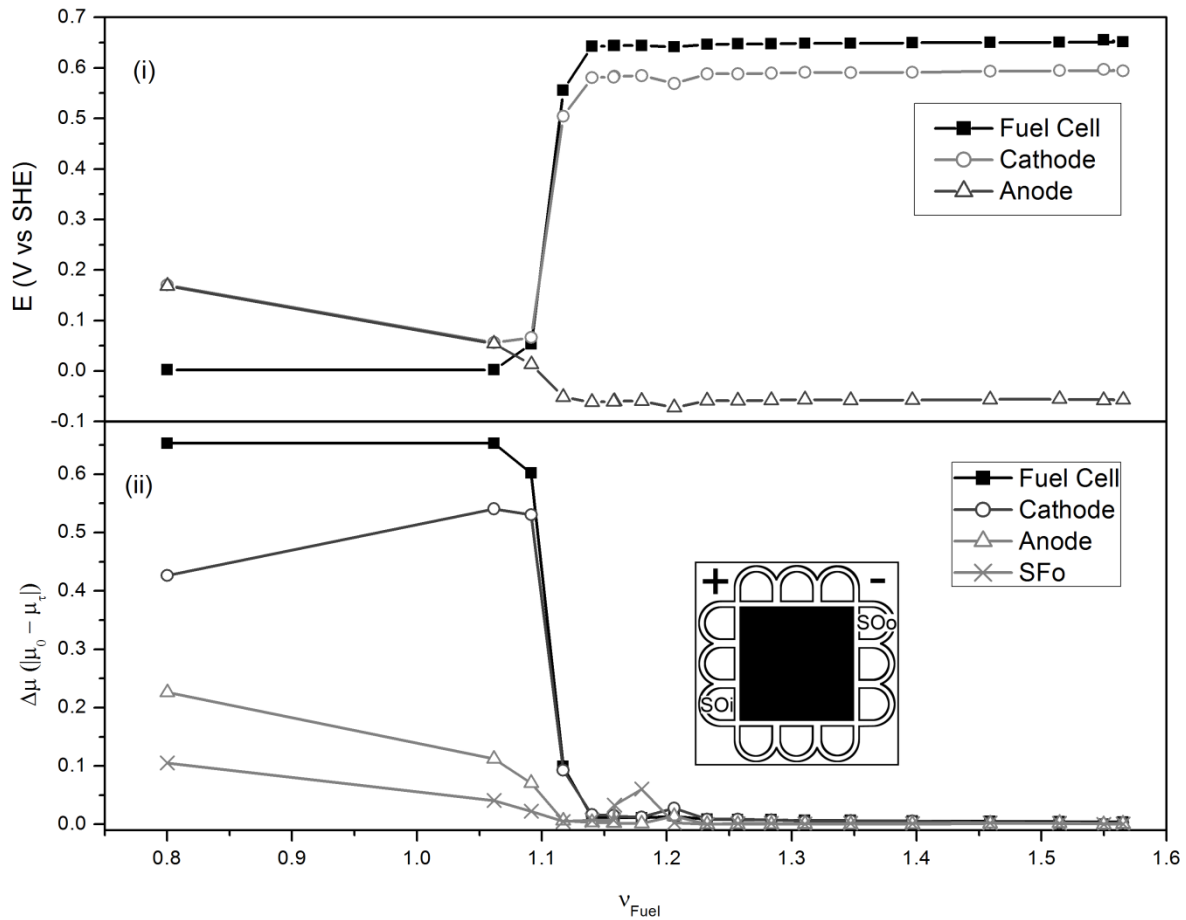


Figure 6-6 Potential response of the anode, cathode, fuel cell and the sensing electrode ($SE_{F,out}$) to low oxidant stoichiometry at 500 mAcm^{-2} : (i) voltage response at each stoichiometric point, and (ii) potential difference between stoichiometry at normal conditions ($v_a = 1.5$) and different stoichiometric values.

6.3 SUMMARY

In order to have a reliable reference electrode, it is necessary to at least know the conditions of the electrode. In the approach used here, the conditions for the reference electrode were kept constant so that the potential didn't drift and oscillated less during different fuel cell operating conditions (e.g., low stoichiometry, flooding, and dehydration). Furthermore, to improve the reference electrode response and reduce the potential oscillation, a catalyst patch was found to be better than a platinum wire contact. The catalyst patch reinforces the membrane (i.e., reduces the dimensional change/wrinkling) and averages the potential value over a larger area, hence providing more accurate results. By using several reference electrodes around the perimeter of the active area it was found that all the reference electrodes gave essentially the same potential regardless of position for a variety of fuel cell operating conditions.

The sensing electrodes that were placed in direct contact with the fuel cell environment were found to be sensitive to the local conditions of the fuel cell. As has been discussed previously, the sensing electrodes are sensitive to the local conditions and can be used as a diagnostic tool. These sensing electrodes were able to diagnose flooding, dehydration, low fuel stoichiometry and low oxidant stoichiometry. In this case, a smaller contact area for the sensing electrodes, such as a wire contact instead of the catalyst patch will increase the sensitivity to the different failure modes at the expense of reproducibility.

7 ANODE AND CATHODE OVERPOTENTIALS AND HEAT PROFILES ON A PEMFC

7.1 INTRODUCTION

Anodic and cathodic individual overpotentials (activation, ohmic, concentration and mass transport) were obtained in a segmented and un-segmented fuel cell by using an arrangement of reference electrodes and different gases with different diffusion coefficients. These isolated anodic and cathodic performance losses have never been reported. The results show that the anodic overpotentials cannot be ignored, even if the only conditions changed are at the cathode. The oxygen concentration has an effect on the anode's potential, hydrogen oxidation and proton flux.

Under dry conditions the difference in the current density between the inlet and the outlet create heat in-plane gradients thermal that are very large due to the half-cell reactions and the water vaporization. As a result, the catalyst layers have an uneven temperature distribution that can result in membrane damage.

The combination of reference electrodes and multi-component gas analysis, allows the measurement and calculation of kinetic and diffusion parameters that can be used for modeling and to better understand the behavior of the different layers of a fuel cell.

7.2 RESULTS AND DISCUSSION

7.2.1 Fuel Cell Overpotentials

Fuel cell performance losses for the anode and the cathode were isolated as shown in Figure 7-1. The values were obtained by taking the ideal equilibrium potential and subtracting the iR corrected performance responses of running the fuel cell with pure oxygen for the activation losses. The concentration losses are the difference between the iR corrected potential response of oxygen and the iR corrected potential response of heliox. The mass transport losses are the difference between the iR corrected potential response of heliox and the iR corrected potential response of air. The resistances were measured by EIS as described in Chapter 3. These measured overpotentials and their calculated constants are summarized in Table 7-1. Sample calculations for the values in Table 7-1 and Figure 7-1 are shown in Appendix A.3. The calculated limiting current values are low compared to the actual measured limiting current. That is because a 10-20 mV difference on the overpotential has an important impact on the value of the limiting current and in exponential expressions the errors are magnified. 10-20 mV potential difference is inside the error range, as the voltage difference between the measured potential from one MEA and the measured potential of a different MEA has a $\sigma = 15$ mV.

Expression	Parameters	Anode	Cathode	Units	Measurement method
$\eta_A = b \ln \frac{i}{i_o}$	{b} (i_o)	{0.006} (7.70×10^{-5})	{0.073} (1.13×10^{-9})	{V} ($A \text{ cm}^{-2}$)	Tafel diagram
$E_\Omega = iR$	R	0.0411	0.0749	$\Omega \text{ cm}^2$	HFR measurement
$\eta_d = \frac{RT}{nF} \ln \left(1 - \frac{i}{i_L} \right)$	i_L	1106.62	1000.42	$A \text{ cm}^{-2}$	From η_{MT} and η_{conc}

Table 7-1 Measured values for the potential losses obtained from Figure 7-1 and their values at a current density of 1 Acm^{-2} . $I_x = 2.8 \text{ mAcm}^{-2}$ at 2.04 atm, 298 K, and a fully humidified membrane.

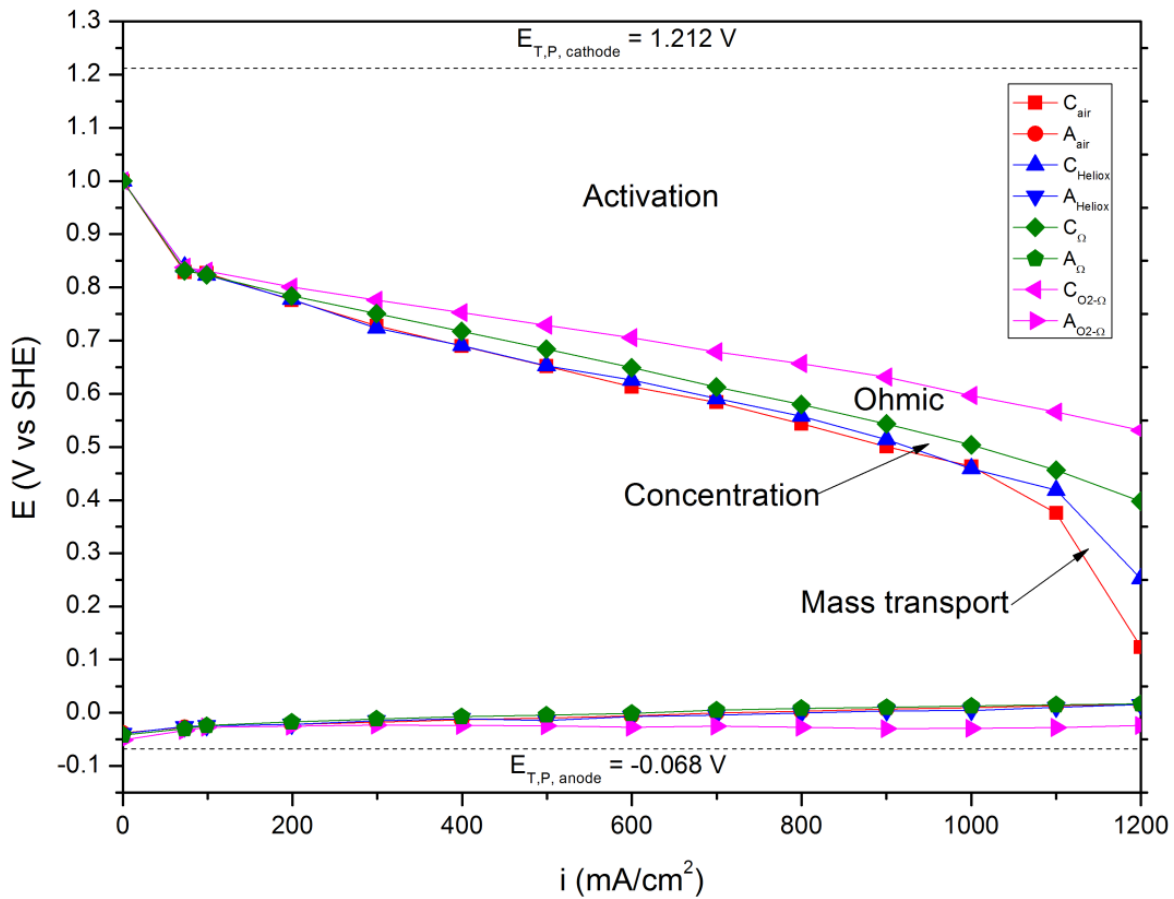


Figure 7-1 Measured anodic and cathodic losses obtained from using different gases with different diffusion coefficients in the cathode and the ohmic losses obtained from high frequency impedance measurements.

Under all conditions, the highest contributions are from the cathodic activation losses. This loss is still the limiting performance factor for state of the art MEA's and a constant focus of research [185, 186]. This loss is mainly due to the poor kinetics of the oxygen reduction reaction. The electrodes used in this work have not been optimized and therefore, the difference between the potential response while using pure oxygen and the potential response while using air is not equal to the theoretical calculated value shown in equation (7-1), where m is a constant ranging from 0.85 to 1 [14, 28].

$$\Delta E_{O_2/air} = E_{O_2} - E_{air} = m \frac{RT}{F} \ln \left(\frac{p_{O_2}}{p_{air}} \right) \quad (7-1)$$

For operation under normal conditions, the anodic contributions represent 5-18.5 % of the total cell potential losses, depending on the current density. The anode activation losses are the most significant anodic contribution. However, diffusion and concentration also play a major role in the anode related losses accounting for up to 30% of the total anodic losses. This can be due to the inability of protons to react on the cathode side as there is less oxygen available when using air or heliox, increasing the anodic mass transport and concentration overpotentials. In other words, the protons produced cannot move from the anodic catalyst sites towards the cathodic catalyst sites, thus increasing all of the anodic overpotentials.

Figure 7-2 shows the polarization curves of the three different humidity conditions with air in the cathode. This figure shows the performance loss ratios of anode and cathode during flooding and drying conditions compared to the normal conditions. The anode overpotential is divided by the sum of the cathode and anode overpotentials. This ratio is compared to the ratio of the cathode overpotential over the sum of the anode and cathode overpotentials. The anodic overpotential contributions increase when there is a deviation from the optimal conditions of 100% RH. During flooding, the anodic ratio increases as the current density increases, since there is more water production and more water being pushed towards the anode and carried into the flow-field. The water blocks the active sites on the catalyst layer decreasing both, the oxidation and the reduction, reactions. The reduced active sites in conjunction with the lower concentration of reactants result in an overall lower fuel cell performance. For the drying condition case, the anodic contributions are larger. The anodic overpotentials start to increase rapidly as soon as the overall fuel cell potential starts to deviate from the normal condition case. As the flow rates increase, the membrane gets drier increasing the resistances and limiting the proton transport, particularly on the anode, as shown in Figure 7-3. The results, in Figure 7-3, show that overpotentials increase more for the anode, reinforcing the importance of not neglecting the anodic losses, especially when there is a deviation from the optimal conditions. During flooding conditions, the anodic overpotentials increase to

10-23% of the total potential loss contributions (proportionally increasing with current density), mainly due to water accumulation. During dry conditions, the anodic overpotentials contribute up to the 30% of the total performance losses, mainly due to the lack of proton mobility.

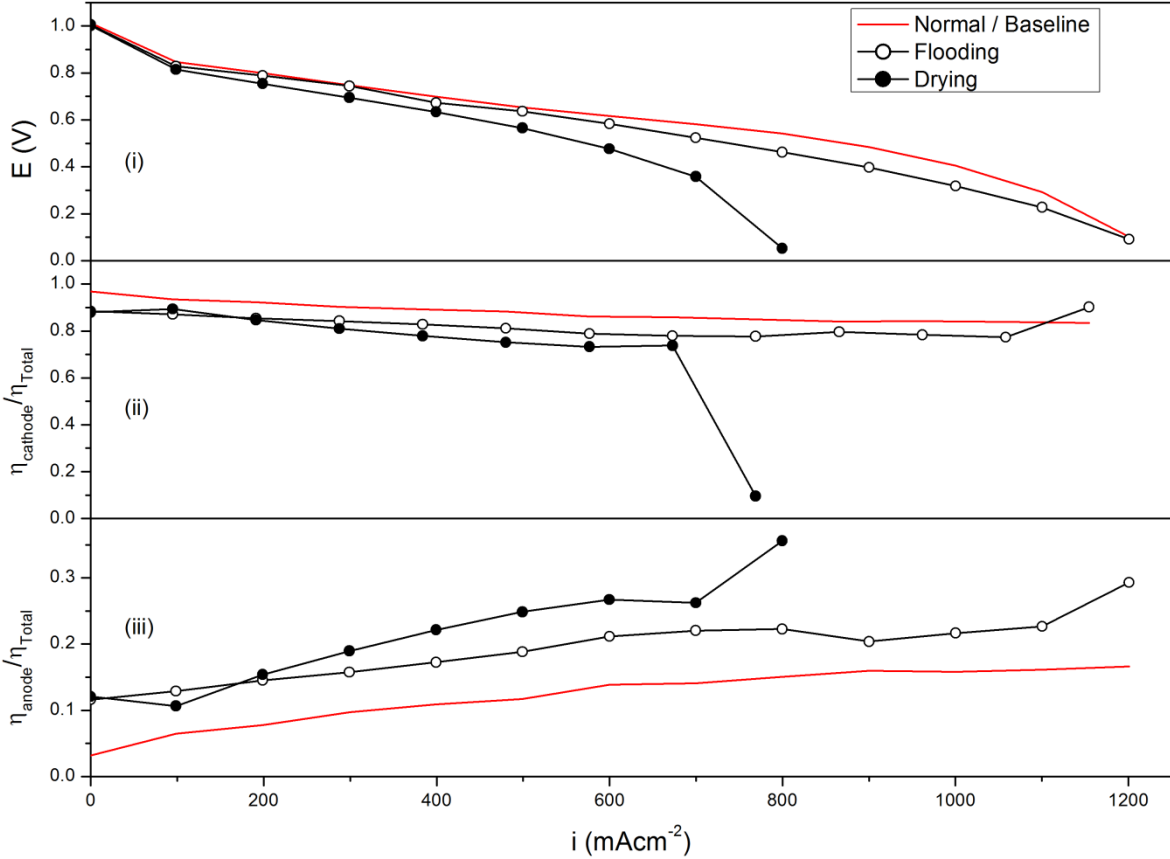


Figure 7-2 (i) Polarization curves for all humidity conditions (Cathode: Air). (ii) Cathode overpotential divided by the total overpotential. (iii) The anode overpotential divided by the total overpotential. In (ii) and (iii), the red line shows the cathode and anode behaviour during normal conditions, respectively.

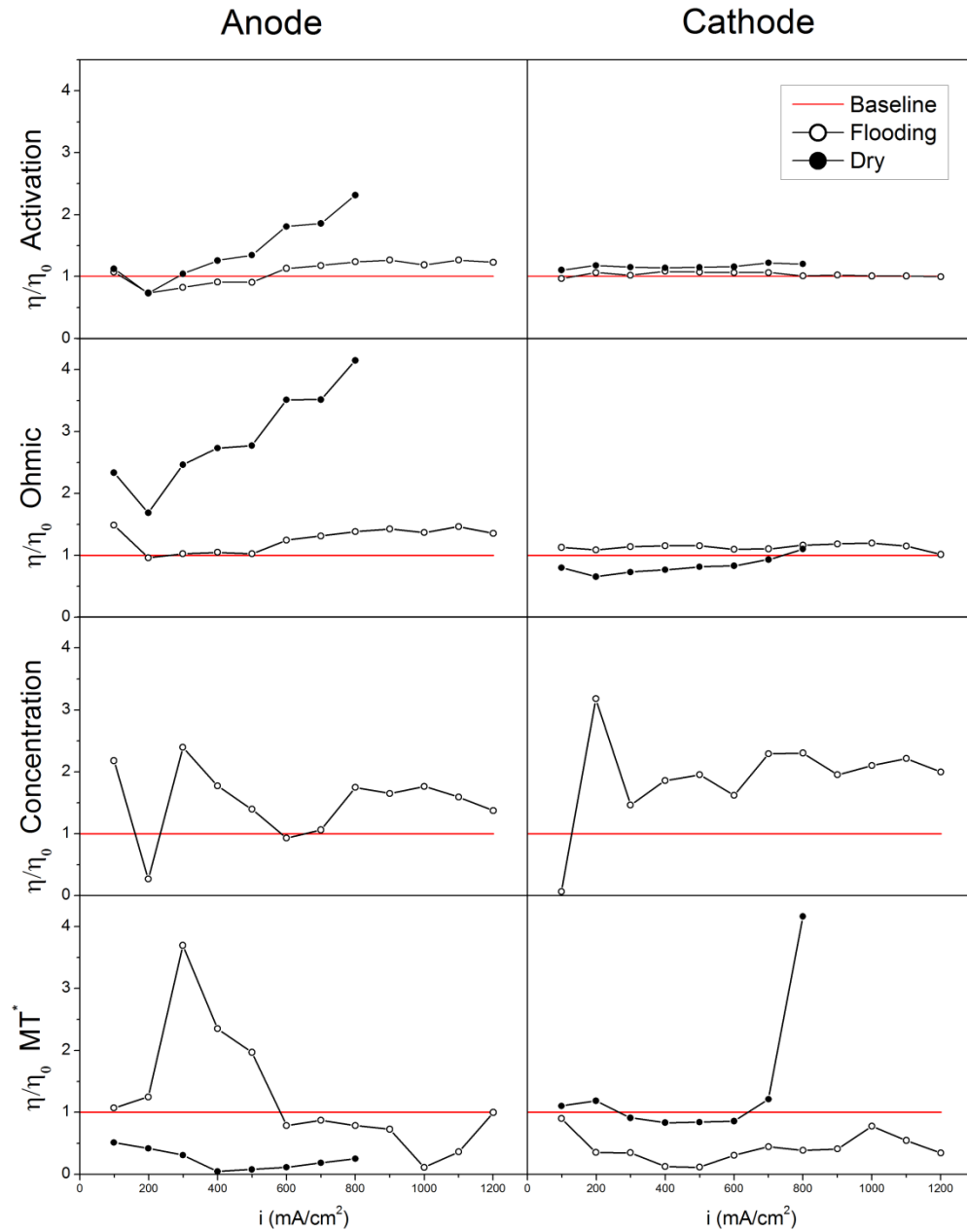


Figure 7-3 Anodic and cathodic overpotentials of dry and flooding conditions normalized against normal conditions (baseline). $\eta/\eta_0 MT$ includes concentration losses for dry conditions as heliox dries the cell faster and the potential response is lower than the potential response when using air.

The calculated activation losses remain practically constant for the cathode, but they increase in the anode, particularly for dry conditions, suggesting, that the hydrogen

oxidation reaction is affected, as noted by Weng [121]. During dry conditions, there is a limited amount of sulfonic sites available in the membrane. The limited sulfonic sites reduce the proton flux, increasing the ohmic resistance and the activation overpotentials. During flooding conditions, as water diffuses through the membrane to the already flooded anode side, reducing the amount of accessible active sites for the hydrogen to react is reduced, thus increasing the anode activation overpotential. Table 7-2 shows the calculated experimental kinetic parameters based on the Tafel equation (see Appendix A.3 for a sample calculation). The exchange current density presented takes into account the partial pressure of the gas, the loading and the mass-specific surface area (this value was estimated to be $60 \text{ m}^2\text{Ptg}^{-1}$ from literature [14]). The values of both, the exchange current density and the Tafel for the cathode slope are in good agreement with the literature ($0.8\text{-}8.7 \times 10^{-9} \text{ Acm}^{-2}$ and $0.053\text{-}0.066 \text{ Vdec}^{-1}$, respectively) [14]. The total value shown in Table 7-2 refers to the sum of anode and cathode contributions and assuming that the anode losses are negligible. This assumption is not valid for drying conditions.

		b (Vdec⁻¹)			i₀ (mAcm⁻²)		
		Anode	Cathode	Total	Anode	Cathode	Total
Baseline	Oxygen	0.008	0.068	0.069	5.54E-05	0.66E-09	0.66E-09
	Heliox	0.011	0.076	0.076	3.99E-05	1.73E-09	1.15E-09
	Air	0.006	0.073	0.073	7.70E-05	1.13E-09	0.92E-09
Flooding	Oxygen	0.019	0.067	0.073	2.05E-04	0.18E-09	0.51E-09
	Heliox	0.025	0.060	0.071	1.73E-04	0.04E-09	0.12E-09
	Air	0.005	0.069	0.069	5.66E-05	0.21E-09	0.17E-09
Drying	Oxygen	0.004	0.068	0.060	7.13E-11	0.23E-09	0.02E-09
	Heliox	0.004	0.147	0.085	6.68E-06	53.0E-09	0.03E-09
	Air	0.004	0.068	0.060	7.13E-11	0.23E-09	0.02E-09

Table 7-2 Tafel kinetic parameters for the anode and cathode for different conditions. The exchange current densities were corrected for the partial pressure of oxygen as described in Chapter 1.

Considering the limitations of the Butler-Erdy-Grutz-Volmer equation and those of the Tafel approximation it is evident that the anode kinetics are fast compared to the cathode kinetics. However, the exchange current densities of the anode under dry conditions are as low as the cathodic ones, when using oxygen and air as oxidant. These values indicate that the anodic contributions should not be neglected; especially during dry conditions, and most likely the Tafel approximation is not valid under these conditions. Heliox values during dry conditions are not in agreement with the values of air and oxygen. This is due to the increased dehydration while using helium as the supporting gas, as water diffuses at a higher rate in helium than in nitrogen (about 10 times faster) and helium has a higher thermal conductivity as shown in Table 7-3, thus carrying more water and drying the MEA faster.

T (K)	K (mWm ⁻¹ K ⁻¹)						D (m ² s ⁻¹)
	100	200	300	400	500	600	298
Air	9.4	18.4	26.2	33.3	39.7	45.7	2.51 x 10 ⁻⁵
Helium	75.5	119.3	156.7	190.6	222.3	252.4	3.14 x 10 ⁻⁴
Nitrogen	9.8	18.7	26	32.3	38.3	44	3.90 x 10 ⁻⁵

Table 7-3 Diffusion coefficient for water in the respective gases and thermal conductivity of air, helium and nitrogen.

As shown in Figure 7-3, the concentration losses during flooding conditions increase by up to 3 times the values for the cathode and up to 2.5 times, for the anode compared to normal conditions. The gas partial pressure is severely reduced by the total pressure change created by the liquid water, limiting the access to the active sites of both electrodes. The presence of liquid water in the flow field channels during flooding creates greater pressure drops for both the anode and the cathode, as shown in Table 7-3. For the cathode, the pressure drop is highest when using air, then heliox and finally pure oxygen, due to the different mass flow rates. The different gases in the cathode also affect the anode because the water concentration increases, changing the diffusion flux from the cathode to the anode. This is reflected in the pressure drop of the anode that is highest when using oxygen, then heliox and finally air; implying that there is a higher concentration of liquid water in the flow-fields and probably in the MEA when running

the fuel cell with pure oxygen, affecting all overpotentials. During flooding conditions, there is a higher pressure difference between the inlet (kept constant at 3.04 atm) and the outlet, as shown in Table 7-3. As both sides are flooded, most likely, the water diffusion from the cathode to the anode is still the predominant mechanism of water transport through the membrane. The pressure drop is less during dry conditions on both the anode and the cathode, indicating the lack of liquid water and probably only one phase flow in agreement with the work of Basu, et al [187].

Condition	Gas	ΔP_c (atm)	ΔP_a (atm)
Normal	Air	0.231	0.145
	Heliox	0.141	0.141
	Oxygen	0.029	0.15
Flooding	Air	0.247	0.17
	Heliox	0.154	0.176
	Oxygen	0.045	0.179
Drying	Air	0.124	0.104
	Oxygen	0.021	0.152

Table 7-4 Pressure drop values at the inlet and outlet of the fuel cell for all gases and conditions at 800 mAcm⁻².

The mass transport overpotential decreased during flooding conditions for all current densities for the cathode, and for current densities above 300 mAcm⁻², for the anode, as shown in Figure 7-3. This is possibly due to the water diffusivity in helium ($3.14 \times 10^{-4} \text{ m}^2\text{s}^{-1}$), which is roughly ten times larger than that in nitrogen ($3.90 \times 10^{-5} \text{ m}^2\text{s}^{-1}$), the higher thermal conductivity of helium and the larger mass flow rate. In other words, helium can carry larger quantities of water through the electrodes due to higher temperatures. The diffusivity assumption is only valid when the gas is not completely saturated (i.e., if the gas is saturated, the water content in the gas only depends on the temperature). Under dry conditions, the mass transport and concentration losses cannot be isolated; as the heliox dries the MEA's faster than air due to the larger diffusivity of water in helium [14, 120]. Therefore, the limiting current is smaller when heliox is used. The mass transport and concentration overpotentials for the dry case increase by 4 times on the cathode closer to the limiting current, mainly due to the lack of ionic movement

through the dehydrated MEA. For the anode, the highest mass transport and concentration losses occur at low current densities, only reducing after larger amounts of water are produced.

Average ohmic resistances are shown for the 3 gases in Figure 7-4. The ohmic losses remain fairly constant for the cathode. However, the anodic losses increase, especially under dry conditions. During flooding conditions while using oxygen, the presence of liquid water limits the reaction, reducing the proton production and increasing the ionic resistances. During dry conditions, the proton conductivity through the ionomer is reduced, increasing the anodic ionic resistances. During flooding conditions, the increase in resistance is low for the cathode, and higher for the anode, increasing with increasing current density and thus, with the amount of liquid water. The highest resistances occur, under dry conditions. Under these conditions, the anodic resistances increase above the cathodic resistance; also increasing with increasing current densities, as previously shown in Figure 7-3. The average temperature of the fuel cell segments, measured by the thermistors in the middle of the current collectors in the PCB, slightly increases with current density (3-5° from 5 to 800 mAcm⁻²). It is lower under dry conditions, especially for oxygen, as shown in Figure 7-4. As evaporation is endothermic, drying conditions also provide cooling conditions. The enthalpy of evaporation at 75 °C is 41.06 kJmol⁻¹, so this is a strong effect. The local cooling is masked by the constant temperature provided by the heating plates. In order to have more reliable results and to understand the different processes that occur in a fuel cell, it is necessary to measure both the resistances and temperatures on the different layers of the MEA.

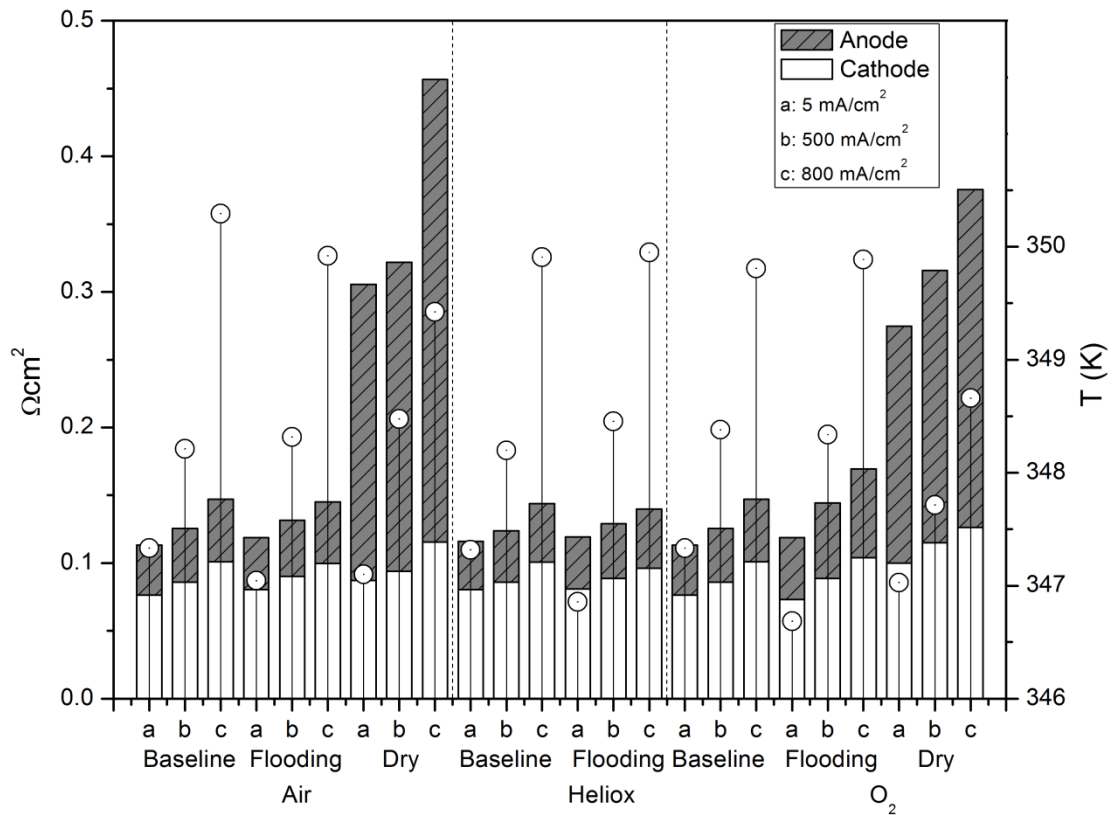


Figure 7-4 Average ohmic resistances (stacked) and temperature averages (white open circles) for anode and cathode during normal, flooding, and dry conditions for the air and oxygen. Only normal and flooding conditions are presented for heliox.

7.2.2 Overpotential Distribution

To understand the effect of the in-plane gradients on the losses in the fuel cell, a segmented cell was used to monitor the current distribution. In Figure 7-5, the current in-plane response to different inlet relative humidity conditions is shown: (a) where the reactants are at 100% RH, (b) where the relative humidity is 50 % and (c) where the gases are dry. The temperature profiles are also shown in b and c. As it is displayed, the temperature remains fairly constant throughout the active area (± 2 °C), indicating even cooling and that the temperature is not affecting the current measurements. The overall current for the fuel cell was held constant at 25 A (522 mAcm^{-2}). The segment 1-1 is

where the gases enter and segment 4-4 is where the gases exit. The segments start with a uniform current density between 1.3 – 1.8 A per segment or $0.425 - 0.588 \text{ A cm}^{-2}$. As can be seen in this figure, as the membrane starts to dehydrate, the segments closer to the inlet (row 1) start producing less current and the middle segments compensate for this current loss. The anode overpotential at row 1 is low compared to the other rows at 50% RH because the anodic overall average resistance is just starting to increase ($0.119 \text{ } \Omega\text{cm}^2$). However, considering that the ohmic losses are a function of the current, the value still suggests an increment in the anodic overpotentials. Also, the cathode overpotentials start to increase creating current and potential gradients that increase as the MEA dries. When the membrane is completely dehydrated, the highest current density is produced by the segments of row 3 and the segments closer to the outlet (row 4), while the segments closest to the inlet barely produce any current. As the MEA dehydrates, the current in-plane gradients are larger and they create large heat differences in the catalyst layer. However, the coolant in this fuel cell transfers enough energy to maintain an approximate homogeneous temperature distribution in the graphite plates.

a)

	1	2	3	4
In	1.54 A 74.99 °C $\eta_a = 0.089 \text{ V}$ $\eta_c = 0.474 \text{ V}$	1.60 A 74.70 °C $\eta_a = 0.088 \text{ V}$ $\eta_c = 0.474 \text{ V}$	1.63 A 75.24 °C $\eta_a = 0.089 \text{ V}$ $\eta_c = 0.474 \text{ V}$	1.64 A 74.88 °C $\eta_a = 0.089 \text{ V}$ $\eta_c = 0.474 \text{ V}$
	1.59 A 75.19 °C $\eta_a = 0.088 \text{ V}$ $\eta_c = 0.474 \text{ V}$	1.72 A 75.23 °C $\eta_a = 0.088 \text{ V}$ $\eta_c = 0.474 \text{ V}$	1.76 A 75.29 °C $\eta_a = 0.088 \text{ V}$ $\eta_c = 0.474 \text{ V}$	1.77 A 75.30 °C $\eta_a = 0.089 \text{ V}$ $\eta_c = 0.474 \text{ V}$
	1.52 A 74.96 °C $\eta_a = 0.088 \text{ V}$ $\eta_c = 0.475 \text{ V}$	1.66 A 75.11 °C $\eta_a = 0.088 \text{ V}$ $\eta_c = 0.474 \text{ V}$	1.70 A 75.16 °C $\eta_a = 0.088 \text{ V}$ $\eta_c = 0.474 \text{ V}$	1.69 A 75.26 °C $\eta_a = 0.089 \text{ V}$ $\eta_c = 0.474 \text{ V}$
	1.28 A 74.81 °C $\eta_a = 0.087 \text{ V}$ $\eta_c = 0.475 \text{ V}$	1.39 A 75.02 °C $\eta_a = 0.087 \text{ V}$ $\eta_c = 0.475 \text{ V}$	1.41 A 75.13 °C $\eta_a = 0.087 \text{ V}$ $\eta_c = 0.475 \text{ V}$	1.47 A 74.71 °C $\eta_a = 0.088 \text{ V}$ $\eta_c = 0.475 \text{ V}$
				Out

b)

	1	2	3	4
In				
1	1.12 A 74.83 °C $\eta_a = 0.110$ V $\eta_c = 0.481$ V	1.19 A 74.10 °C $\eta_a = 0.111$ V $\eta_c = 0.482$ V	1.27 A 74.94 °C $\eta_a = 0.110$ V $\eta_c = 0.482$ V	1.26 A 74.53 °C $\eta_a = 0.113$ V $\eta_c = 0.481$ V
2	1.67 A 75.12 °C $\eta_a = 0.120$ V $\eta_c = 0.477$ V	1.80 A 75.06 °C $\eta_a = 0.122$ V $\eta_c = 0.477$ V	1.85 A 75.05 °C $\eta_a = 0.123$ V $\eta_c = 0.477$ V	1.84 A 74.83 °C $\eta_a = 0.117$ V $\eta_c = 0.477$ V
3	1.69 A 74.89 °C $\eta_a = 0.124$ V $\eta_c = 0.470$ V	1.82 A 74.87 °C $\eta_a = 0.129$ V $\eta_c = 0.469$ V	1.88 A 74.83 °C $\eta_a = 0.129$ V $\eta_c = 0.468$ V	1.85 A 74.99 °C $\eta_a = 0.124$ V $\eta_c = 0.469$ V
4	1.44 A 74.86 °C $\eta_a = 0.118$ V $\eta_c = 0.470$ V	1.53 A 74.94 °C $\eta_a = 0.121$ V $\eta_c = 0.470$ V	1.56 A 75.09 °C $\eta_a = 0.121$ V $\eta_c = 0.470$ V	1.55 A 74.41 °C $\eta_a = 0.119$ V $\eta_c = 0.470$ V
				Out

c)

	2	3	4	
In				
1	0.34 A 74.38 °C $\eta_a = 0.149$ V $\eta_c = 0.484$ V	0.23 A 73.62 °C $\eta_a = 0.142$ V $\eta_c = 0.484$ V	0.23 A 74.49 °C $\eta_a = 0.144$ V $\eta_c = 0.484$ V	0.33 A 74.10 °C $\eta_a = 0.150$ V $\eta_c = 0.484$ V
2	1.12 A 74.67 °C $\eta_a = 0.133$ V $\eta_c = 0.479$ V	1.15 A 74.59 °C $\eta_a = 0.136$ V $\eta_c = 0.479$ V	1.18 A 74.57 °C $\eta_a = 0.139$ V $\eta_c = 0.479$ V	1.27 A 74.74 °C $\eta_a = 0.140$ V $\eta_c = 0.479$ V
3	2.12 A 74.58 °C $\eta_a = 0.120$ V $\eta_c = 0.472$ V	2.28 A 74.56 °C $\eta_a = 0.124$ V $\eta_c = 0.471$ V	2.34 A 74.55 °C $\eta_a = 0.122$ V $\eta_c = 0.470$ V	2.31 A 74.71 °C $\eta_a = 0.123$ V $\eta_c = 0.471$ V
4	2.41 A 74.60 °C $\eta_a = 0.112$ V $\eta_c = 0.471$ V	2.65 A 74.65 °C $\eta_a = 0.108$ V $\eta_c = 0.469$ V	2.74 A 74.83 °C $\eta_a = 0.109$ V $\eta_c = 0.469$ V	2.64 A 74.16 °C $\eta_a = 0.116$ V $\eta_c = 0.469$ V
				Out

Figure 7-5 Current distribution of air/H₂ for different operating conditions (a) 100 % RH (b) 50 % RH and (c) 0 % RH. The current was kept constant at 25 A (522 mAcm⁻²). Segment 1-1 and segment 4-4 are the segments where the inlet and outlet are located, respectively.

The fuel cell potential depends on the overpotential values from the anode and the cathode as shown in Figure 7-6. Assuming that all the water produced is vaporized under dry conditions, the heat profiles in the MEA change in accordance with the current and water produced. Figure 7-7 shows these profiles of heat flux (in Watts) over the active area for both the anode and the cathode under dry conditions. The heat profiles were only calculated for the dry condition, as for normal and flooding conditions it is not valid to assume complete water evaporation. The power profiles were calculated based on the enthalpy of reaction for the anodic half-cell endothermic reaction (440.487 kJmol⁻¹ @ 343 K), the enthalpy of reaction for the cathodic half-cell exothermic reaction (-683.371 kJmol⁻¹ @ 343 K), the enthalpy of vaporization of water (41.787 kJmol⁻¹ @ 343 K) using Equations (7-2), (7-3), and (7-4), for the fuel cell. The values for the enthalpy of reaction were calculated with the bond energies of the atoms and molecules. The total heat released by the fuel cell is defined by the heat of reactions for the fuel cell (cathode and anode) minus the fuel cell potential (work).

$$Q_{total} = Q_{cathode} + Q_{anode} - Work \text{ (Fuel cell potential)} \quad (7-2)$$

$$Q_{cathode} = \Delta H_{343,cathode} - \Delta G_{343,cathode} - nF \sum \eta_{cathode} + \Delta H_{vap} \quad (7-3)$$

$$Q_{anode} = \Delta H_{343,anode} - \Delta G_{343,anode} - nF \sum \eta_{anode} \quad (7-4)$$

After calculating the heat sources, they are then multiplied by the molar flow-rate to obtain the power profiles. As expected, the maximum heat production occurs where the largest current densities are, but the largest usable work is in row 3 for the dry conditions. The energy difference is lower in the final row (closer to the outlets) because as the current density increases, the water production increases; there are less losses that generate heat. These localized heat differences can create stresses that may damage the MEA, as discussed by Gasteiger, et.al. [14] based on the overpotentials and Pharoah, et.al. [188] based on the temperature and heat distribution.

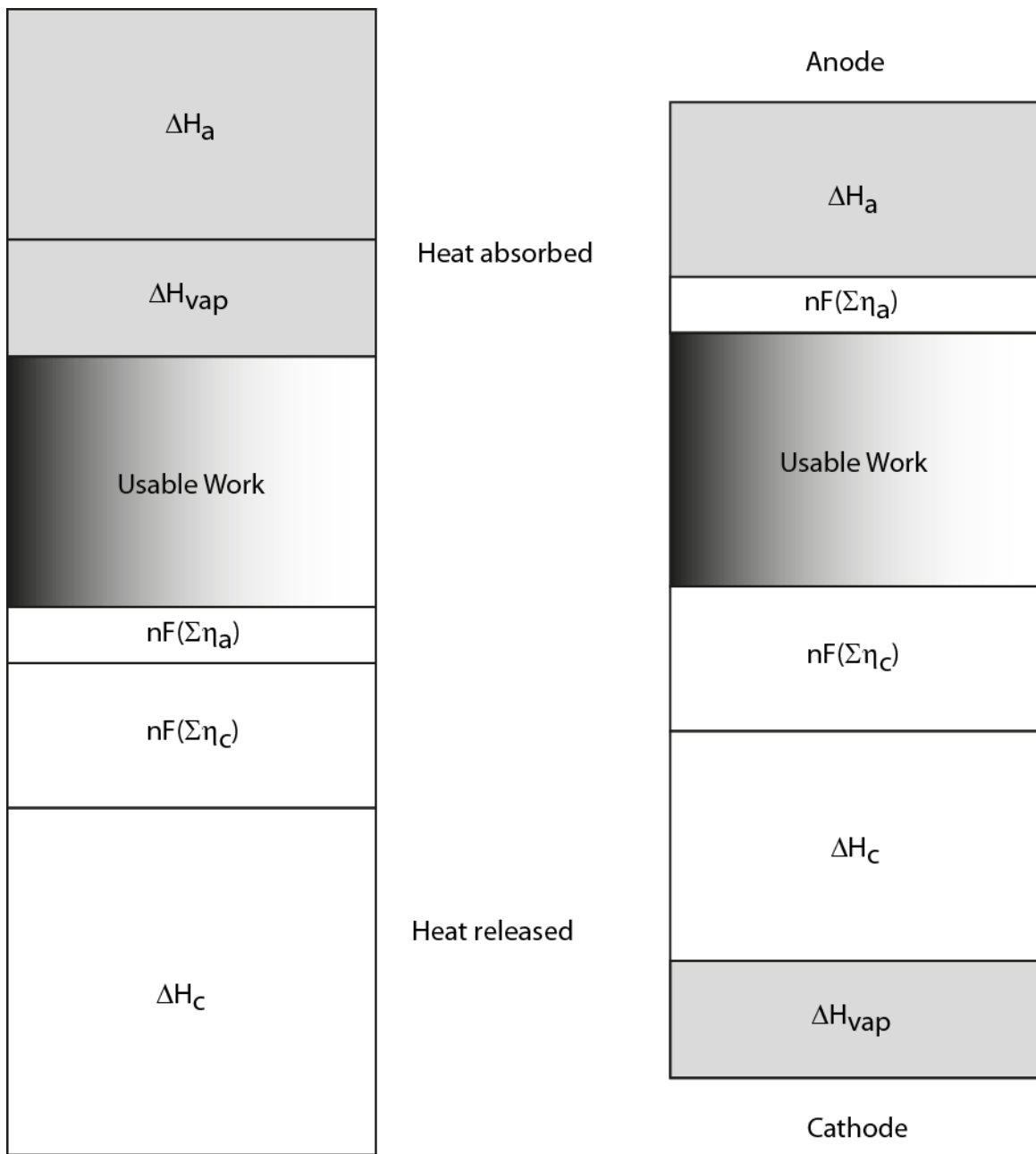


Figure 7-6 Fuel cell's energy profiles. The gray area is the heat of vaporization in the cathode, which consumes energy from the heat of reaction of the cathode.

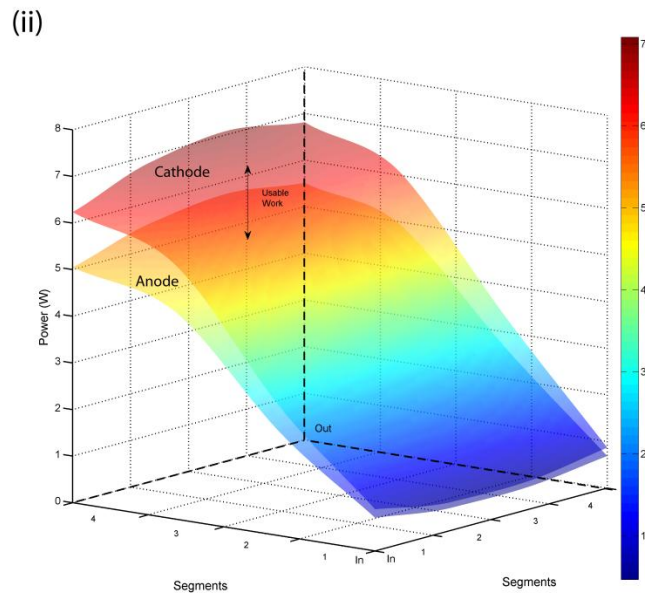
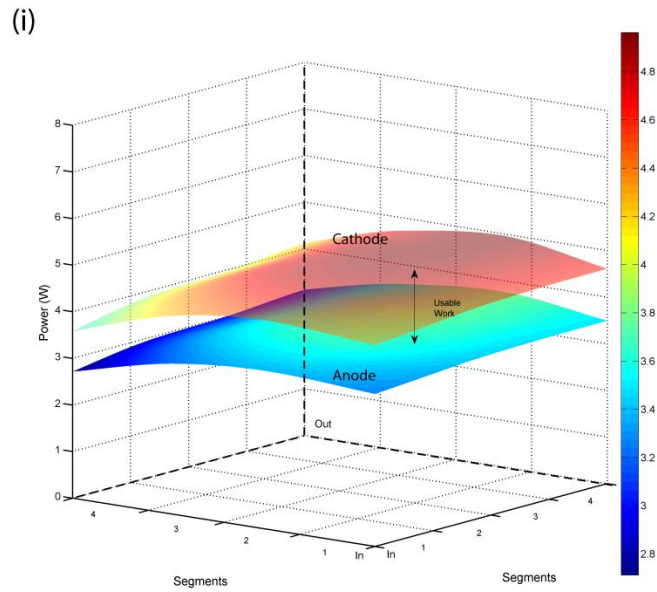


Figure 7-7 In-plane power generation from heat for the cathode (top) and anode (bottom) catalyst layers for 100 % RH (i) and under dry conditions (ii). No heat of evaporation is considered for the 100% RH case. The values were calculated using the current distributions and the overpotential values and then interpolated to create a continuous function.

7.3 SUMMARY

Anodic and cathodic individual overpotentials were obtained in a segmented and unsegmented fuel cell by using an arrangement of reference electrodes and different gases with different diffusion coefficients. The results show that the anodic overpotentials cannot be ignored, even if the anode conditions remain constant and changes are imposed on the cathode only. The anode can contribute up to 20 % of the losses under normal and flooding conditions and above 30 % under dry conditions. The measured and calculated kinetic parameters support these results, where under dry conditions the exchange current density of the anode is even smaller than that of the cathode and very similar to that of the overall reaction.

The anode overpotentials are affected by the oxygen concentration that limits the cathodic reaction controlling the proton movement and dictating the proton production. The anode potential is also largely affected by the current distribution as the iR losses contribute to about 30 % of its total overpotentials. However, in order to have more reliable results, it is necessary to measure the resistances and potentials individually (i.e., not only the current) and as close to the electrode as possible.

The activation losses for both the anode and the cathode are the largest, even for state of the art electrodes [28]. Cathode activation overpotentials are the largest, but anodic overpotentials can be significant, especially under dry conditions. The activation overpotentials increase in the order from normal to flooding to dry conditions. Under dry conditions, the membrane conductivity decreases leading to higher ionic resistances that increase all the overpotentials, especially at the anode. Ohmic losses increase with current density and vary depending on the humidity conditions. These conditions also affect the temperature profile in the fuel cell, e.g., cooling it under dry conditions due to water vaporization. Based on the calculated overpotentials and enthalpies of the half-cell reactions, it was possible to calculate the temperature distribution over the active area. The results show that the heat from the cathodic exothermic reaction is highly affected by the water vaporization for dry conditions and a large current gradient exists. However, in

order to confirm these temperature profiles, it is necessary to measure the temperature as close to the catalyst layers as possible.

The activation, ohmic, concentration and mass transport losses increase proportionally with current density and vary locally with different gradients across the fuel cell, especially during dry conditions. By combining the use of reference electrodes and current mapping, it is possible to measure and calculate different parameters that can be used for modeling and to understand the behavior of the anode and the cathode independently.

8 CONCLUSIONS

A new approach to fuel cell diagnostics is presented. The approach is based on sensing electrodes. The sensing electrodes that were placed in direct contact with the fuel cell environment were found to be sensitive to the local conditions of the fuel cell making them useful as a diagnostic tool. Each failure mode had a characteristic response based on the sensing electrode measurements prior to any changes in the overall cell voltage. These sensing electrodes were able to diagnose flooding, dehydration, low fuel stoichiometry and low oxidant stoichiometry. It was found that if the local conditions for the sensing electrodes change with respect to the operating conditions and associated failure mode, the sensing electrodes will have a potential response characteristic to that failure. In this case, a smaller contact area for the sensing electrodes, such as a wire contact instead of the catalyst patch will increase the sensitivity to the different failure modes (as shown in the faster response in Chapter 5 than in Chapter 6).

This type of approach can be used in practical applications as it is cost effective and not very invasive. The sensing electrodes could be located at the inlet cell and at the end cell of a fuel cell stack or at the inlet and outlet of random cells in the stack. That way, it would only be necessary to monitor 4-10 potentials without damaging the fuel cell stack or imposing extra costs. This type of approach (with a DHE) has been used by AFCC to study corrosion and diagnose contamination in a PEMFC [110].

We have shown a new approach for the accurate use of reference electrodes in fuel cells. In order to have a reliable reference electrode, it is necessary to at least know the conditions of the electrode. In the approach used here, the conditions for the reference electrode were kept constant so that the potential didn't drift or oscillate during different fuel cell operating conditions (e.g., low stoichiometry, flooding, and dehydration). Furthermore, to improve the reference electrode response and reduce the potential for oscillation, an isolated catalyst patch on the membrane was found to be better than just a platinum wire in contact with the membrane. The catalyst patch reinforces the membrane (i.e., reduces the dimensional change/wrinkling) and averages the potential value over a larger area, hence providing more accurate results. By using several reference electrodes

around the perimeter of the active area it was found that all the reference electrodes gave essentially the same potential regardless of position for a variety of fuel cell operating conditions.

By using the reference electrode arrangement in this thesis and different oxidant gases with different diffusion coefficients, it is possible to obtain the anodic and cathodic individual overpotentials in segmented and un-segmented fuel cells. The results show that the anodic overpotentials cannot be ignored, even if the anode conditions remain constant and changes are imposed on the cathode only. The anode can contribute up to 20 % of the losses under normal and flooding conditions and above 30 % under dry conditions. The measured and calculated kinetic parameters support these results, where under dry conditions the exchange current density of the anode is even smaller than that of the cathode and very similar to that of the overall reaction.

The anode overpotentials are affected by the oxygen concentration that limits the cathodic reaction, controlling the proton movement and dictating the proton production. The anode potential is also largely affected by the current distribution as the iR losses contribute to about 30 % of its total overpotentials.

Cathode activation overpotentials are the largest, but anodic overpotentials can be significant, especially under dry conditions. The activation overpotentials increase in the order from normal to flooding to dry conditions. Under dry conditions, the membrane conductivity decreases leading to higher ionic resistances that increase all the overpotentials, especially at the anode. Ohmic losses increase with current density and vary depending on the humidity conditions. These conditions also affect the temperature profile in the fuel cell, e.g., cooling it under dry conditions due to water vaporization. Based on the calculated overpotentials and enthalpies of the half-cell reactions, it was possible to calculate the temperature distribution over the active area. The results show that the heat from the cathodic exothermic reaction is highly affected by the water vaporization for dry conditions, and a large current gradient exists between the inlet and the outlet. However, in order to confirm these temperature profiles, it is necessary to measure the temperature as close to the catalyst layers as possible.

The activation, ohmic, concentration and mass transport losses increase proportionally with current density and vary locally with different gradients across the fuel cell, especially during dry conditions. By combining the use of reference electrodes and current mapping, it is possible to measure and calculate different parameters that can be used for modeling and to understand the behavior of the anode and the cathode independently.

9 FUTURE WORK AND RECOMMENDATIONS

Fuel cells are at the brink of commercialization. Therefore, there has been an increased interest in improving fuel cell durability and reliability. Thus, preventing failure modes has been one of the main focuses. At the beginning of this PhD, the approach was to look for alternate methods of diagnosing fuel cell failure modes. So far, research has resulted in a diagnostic method based on sensing electrodes. In the process, it was clear that before this work, the anodic contributions had been assumed to be negligible. This work shows the importance of the anodic contributions and their effect on the overall fuel cell's overpotentials. The following are the proposed research directions for future work:

1. Sensing electrodes

In order to demonstrate the use of sensing electrodes in real life applications, it is necessary to test them in state of the art membranes. This could be done by placing a Nafion[®] coated platinized platinum wire or by adding a small piece of Nafion[®] coated with catalyst (half-cell) on top of a catalyst coated membrane, as shown in Figure 9-1.

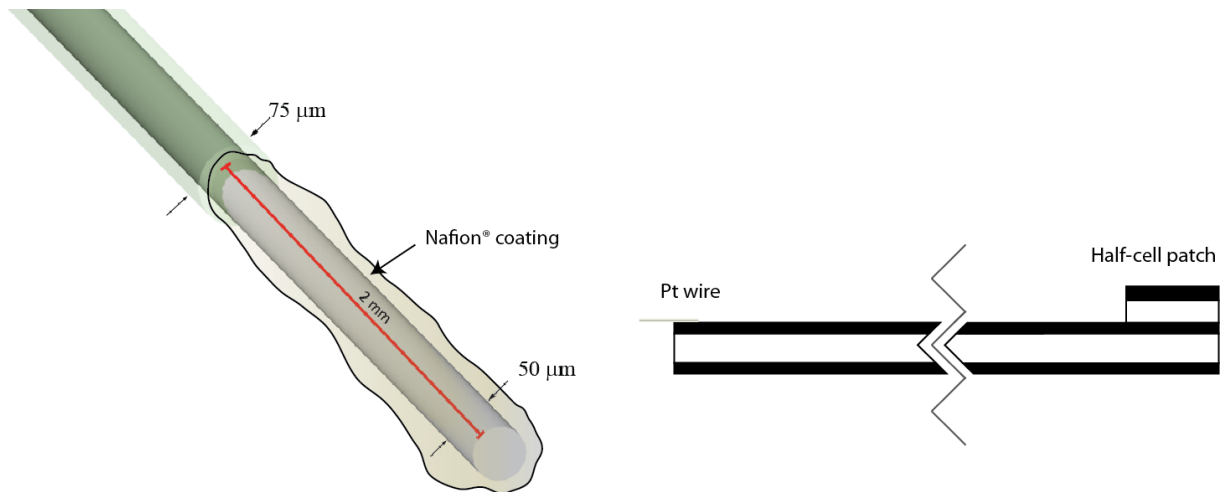


Figure 9-1 Nafion[®] coated platinized platinum wire located in catalyst coated membrane and half-cell patch located in a catalyst coated membrane to use as a sensing electrode.

After the process has been proven, the sensing electrodes need to be tested in a fuel cell stack to know the proper locations for the different types of failure modes. From what was found in this thesis the starting locations would be:

- a. Drying – First cells of the stack at the inlets.
- b. Flooding – Last cells of the stack at the outlets.
- c. Low fuel stoichiometry – Last cells of the stack at the outlets on the fuel side.
- d. Low oxidant stoichiometry – Last cells of the stack at the outlets on the oxidant side.

However, it is recommendable to place sensing electrodes on the first cells of the fuel cell stack, the middle cells of the fuel cell stack and the last cells of the fuel cell stack. The average values can be recorded and manipulated to have more insight about the performance of the fuel cell stack. Similar to what was done in a single cell in Chapter 5.

2. Reference electrodes

Accurate isolation of the anodic and cathodic contributions is possible with reference electrodes. The necessary kinetic parameters in order to improve catalyst development and fuel cell performance can be obtained. Therefore, the approach used with reference electrodes should be done for new MEA types and cell designs. New methods for implementing the reference electrode could be done similar to the proposed for the sensing electrodes (shown in Figure 9-1), where a platinized platinum wire is coated with Nafion[®] or a half-cell patch is used.

Further research could involve using the reference electrodes for the isolation of the anodic and cathodic impedance spectra. The reliable isolation of the anodic and cathodic contributions can provide information about the behaviour of the capacitive resistance developed while running the cell under different regimes.

3. **Individual anodic and cathodic overpotentials**

The work in this thesis has shown that it is possible to obtain individual anodic and cathodic overpotentials. A further step would be using the data gathered in a model that can simulate different types of conditions and potential responses. Additionally, the technique could be used to study specific layers of the fuel cell (e.g., catalyst, membrane, GDL...) and their effect on the anode and cathode. This may require placing sensing electrodes in the different layers.

4. **Heat, overpotential and current distribution**

In this thesis it was shown that the current distribution creates gradients that affect the localized overpotentials, creating heat differentials. However, it is still necessary to measure the temperature as close as possible to the reaction sites, i.e., catalyst layer. The measured temperature can lead to the confirmation of the calculated overpotentials and heat profiles. Measuring the temperature on the catalyst layer can also lead to valuable information about the transient behaviour, especially for water production and evaporation. The segmented cell is a valuable tool that can help the development of flow fields, GDL's, catalysts, etc.

In order to make data clearer, the gas flow field should be in co-flow with the coolant flow-field. Parallel channels would also help in the interpretation of data.

BIBLIOGRAPHY

1. Bossel, U. *The Birth of the Fuel Cell*. in *European Fuel Cell Forum*. 2000. Oberrohrdorf, Switzerland.
2. Oesper, R.E., *Christian Friedrich Schonbein. Part II. Experimental labors*. Journal of Chemical Education, 1929. **6**(4): p. 677-null.
3. Sandstede, G., E.J. Cairn, V.S. Bagotsky, and K. Wiesener, eds. *History of low temperature fuel cells*. Handbook of Fuel Cells: Fundamentals, Technologies, and Applications. Vol. 1 Chapter 12. 2003, John Wiley & Sons: New York.
4. Grove, W.R., *On a gaseous voltaic battery*. Philosophical Magazine Series 3. **21**(140): p. 417 - 420.
5. Grove, W.R., *On the Gas Voltaic Battery. Voltaic Action of Phosphorus, Sulphur and Hydrocarbons*. Philosophical Transactions of the Royal Society of London, 1845. **135**: p. 351-361.
6. Mond, L. and C. Langer, *A New Form of Gas Battery*. Proceedings of the Royal Society of London, 1889. **46**(280-285): p. 296-304.
7. Appleby, A.J., *From Sir William Grove to today: fuel cells and the future*. Journal of Power Sources, 1990. **29**(1-2): p. 3-11.
8. The_Smithsonian_Institute. *Collecting History of Fuel Cells*
<http://americanhistory.si.edu/fuelcells/index.htm>. 2010.
9. Hammet, A., ed. *The components of an electrochemical cell*. Handbook of Fuel Cells: Fundamentals, Technologies, and Applications, ed. Vielstich, W., A. Lamm, and H.A. Gasteiger. Vol. 1 Chapter 1. 2003, John Wiley & Sons: New York.
10. Perry, R.H. and D.W. Green, *Perry's Chemical Engineers' Handbook (7th Edition)*. 1997, McGraw-Hill.
11. Haynes, W.M., ed. *CRC Handbook of Chemistry and Physics 91st Edition*. 2011, CRC Press/Taylor and Francis: Boca Raton.
12. Gyenge, E., *ChBE 477: Fuel Cells & Electrochemical Systems Course Notes*. 2006.
13. McNaught, A.D. and A. Wilkinson, *Compendium of Chemical Terminology*. 1997, Blackwell Science Ltd.: <http://goldbook.iupac.org/index.html>.
14. Gasteiger, H.A., W. Gu, R. Makharia, M.F. Mathias, and B. Sompalli, eds. Handbook of Fuel Cells: Fundamentals, Technologies, and Applications, ed. Vielstich, W., A. Lamm, and H.A. Gasteiger. Vol. 3 Chapter 46. 2003, John Wiley & Sons: New York.
15. Larminie, J. and A. Dicks, *Fuel Cell Systems Explained (2nd Edition)*, John Wiley & Sons.
16. Reusch, W., *Virtual Text of Organic Chemistry*. 1999, Michigan: Michigan State University.
17. Larminie, J.D., Andrew, *Fuel Cell Systems Explained*. 2nd ed. 2003, New York: John Wiley & Sons. p. 1 - 200.
18. Kim, J., S.-M. Lee, S. Srinivasan, and C.E. Chamberlin, *Modeling of proton exchange membrane fuel cell performance with an empirical equation*. Journal of the Electrochemical Society, 1995. **142**(Compendex): p. 2670-2674.
19. Haji, S., *Analytical modeling of PEM fuel cell i-V curve*. Renewable Energy, 2011. **36**(2): p. 451-458.
20. Hsuen, H.-K. and K.-M. Yin, *Performance equations for a polymer electrolyte membrane fuel cell with unsaturated cathode feed*. Journal of Power Sources, 2011. **196**(1): p. 218-227.

21. Chiu, Y.-J., *An algebraic semi-empirical model for evaluating fuel crossover fluxes of a DMFC under various operating conditions*. International Journal of Hydrogen Energy, 2010. **35**(12): p. 6418-6430.
22. Ang, S.M.C., D.J.L. Brett, and E.S. Fraga, *A multi-objective optimisation model for a general polymer electrolyte membrane fuel cell system*. Journal of Power Sources, 2010. **195**(9): p. 2754-2763.
23. Kulikovskiy, A.A., T. Wuster, A. Egmen, and D. Stolten, *Analytical and Numerical Analysis of PEM Fuel Cell Performance Curves*. Journal of the Electrochemical Society, 2005. **152**(6): p. A1290-A1300.
24. Dannenberg, K., P. Ekdunge, and G. Lindbergh, *Mathematical model of the PEMFC*. Journal of Applied Electrochemistry, 2000. **30**(12): p. 1377-1387.
25. Squadrito, G., G. Maggio, E. Passalacqua, F. Lufrano, and A. Patti, *An empirical equation for polymer electrolyte fuel cell (PEFC) behaviour*. Journal of Applied Electrochemistry, 1999. **29**(12): p. 1449-1455.
26. Inaba, M., T. Kinumoto, M. Kiriake, R. Umebayashi, A. Tasaka, and Z. Ogumi, *Gas crossover and membrane degradation in polymer electrolyte fuel cells*. Electrochimica Acta, 2006. **51**(26): p. 5746-5753.
27. Adler, S.B., B.T. Henderson, M.A. Wilson, D.M. Taylor, and R.E. Richards, *Reference electrode placement and seals in electrochemical oxygen generators*. Solid State Ionics, 2000. **134**(1-2): p. 35-42.
28. Wood, D.L. and I.I.I.R.L. Borup, *Estimation of Mass-Transport Overpotentials during Long-Term PEMFC Operation*. Journal of the Electrochemical Society, 2010. **157**(8): p. B1251-B1262.
29. Roelofs, M. *Membrane issues for PEM fuel cells*. in *NSF Workshop*. 2001. Arlington, Virginia.
30. Okada, T., *Theory for water management in membranes for polymer electrolyte fuel cells: Part 1. The effect of impurity ions at the anode side on the membrane performances*. Journal of Electroanalytical Chemistry, 1999. **465**(1): p. 1-17.
31. Okada, T., *Theory for water management in membranes for polymer electrolyte fuel cells: Part 2. The effect of impurity ions at the cathode side on the membrane performances*. Journal of Electroanalytical Chemistry, 1999. **465**(1): p. 18-29.
32. Okada, T., G. Xie, and M. Meeg, *Simulation for water management in membranes for polymer electrolyte fuel cells*. Electrochimica Acta, 1998. **43**(14-15): p. 2141-2155.
33. Eisenberg, A. and J.S. Kim, *Introduction to Ionomers*. 1998, New York: Wiley.
34. Grot, W., *Fluorinated Ionomers*. 2008, Norwich, NY: William Andrew Publishing. 250.
35. Adachi, M., *Proton Exchange Membrane Fuel Cells: Water Permeation Through Nafion[®] Membranes*, in *Department of Chemistry*. 2010, Simon Fraser University: Burnaby. p. 167.
36. Mauritz, K.A. and R.B. Moore, *State of Understanding of Nafion*. Chemical Reviews, 2004. **104**(10): p. 4535-4586.
37. Eikerling, M., Y.I. Kharkats, A.A. Kornyshev, and Y.M. Volkovich, *Phenomenological theory of electro-osmotic effect and water management in polymer electrolyte proton-conducting membranes*. Journal of The Electrochemical Society, 1998. **145**(8): p. 2684-2699.
38. Dai, W., H. Wang, X.-Z. Yuan, J.J. Martin, D. Yang, J. Qiao, and J. Ma, *A review on water balance in the membrane electrode assembly of proton exchange membrane fuel cells*. International Journal of Hydrogen Energy, 2009. **34**(23): p. 9461-9478.

39. Zawodzinski, J.T.A., C. Derouin, S. Radzinski, R.J. Sherman, V.T. Smith, T.E. Springer, and S. Gottesfeld, *Water Uptake by and Transport Through Nafion^{[sup [registered sign]]} 117 Membranes*. Journal of the Electrochemical Society, 1993. **140**(4): p. 1041-1047.
40. Romero, T. and W. Mérida, *Water transport in liquid and vapour equilibrated Nafion(TM) membranes*. Journal of Membrane Science, 2009. **338**(1-2): p. 135-144.
41. Springer, T.E., M.S. Wilson, and S. Gottesfeld, *Modeling and Experimental Diagnostics in Polymer Electrolyte Fuel Cells*. Journal of the Electrochemical Society, 1993. **140**(12): p. 3513-3526.
42. Nguyen, T.V. and R.E. White, *Water and heat management model for proton-exchange-membrane fuel cells*. Journal of The Electrochemical Society, 1993. **140**(8): p. 2178-2186.
43. Stumper, J., H. Haas, and A. Granados, *In Situ Determination of MEA Resistance and Electrode Diffusivity of a Fuel Cell*. Journal of The Electrochemical Society, 2005. **152**(4): p. A837-A844.
44. Chen, F., Y.-G. Su, C.-Y. Soong, W.-M. Yan, and H.-S. Chu, *Transient behavior of water transport in the membrane of a PEM fuel cell*. Journal of Electroanalytical Chemistry, 2004. **566**(1): p. 85-93.
45. De Francesco, M., E. Arato, and P. Costa, *Transport phenomena in membranes for PEMFC applications: an analytical approach to the calculation of membrane resistance*. Journal of Power Sources, 2004. **132**(1-2): p. 127-134.
46. Natarajan, D. and T. Van Nguyen, *Three-dimensional effects of liquid water flooding in the cathode of a PEM fuel cell*. Journal of Power Sources, 2003. **115**(1): p. 66-80.
47. Sun, H., H. Liu, and L.-J. Guo, *PEM fuel cell performance and its two-phase mass transport*. Journal of Power Sources, 2005. **143**(1-2): p. 125-135.
48. Karimi, G. and X. Li, *Electroosmotic flow through polymer electrolyte membranes in PEM fuel cells*. Journal of Power Sources, 2005. **140**(1): p. 1-11.
49. He, W., J.S. Yi, and T. Van Nguyen, *Two-phase flow model of the cathode of PEM fuel cells using interdigitated flow fields*. AIChE Journal, 2000. **46**(10): p. 2053-2064.
50. Lin, G., W. He, and T. Van Nguyen, *Modeling liquid water effects in the gas diffusion and catalyst layers of the cathode of a PEM fuel cell*. Journal of The Electrochemical Society, 2004. **151**(12): p. 1999-2006.
51. Cukierman, S., *Et tu, Grotthuss! and other unfinished stories*. Biochimica et Biophysica Acta (BBA) - Bioenergetics, 2006. **1757**(8): p. 876-885.
52. Agmon, N., *The Grotthuss mechanism*. Chemical Physics Letters, 1995. **244**(5-6): p. 456-462.
53. Aotani, K., S.-i. Miyazaki, N. Kubo, and M. Katsuta, *An Analysis of The Water Transport Properties of Polymer Electrolyte Membrane*. ECS Transactions, 2008. **16**(2): p. 341-352.
54. Fuller, T.F. and J. Newman, *Experimental Determination of the Transport Number of Water in Nafion 117 Membrane*. Journal of the Electrochemical Society, 1992. **139**(5): p. 1332-1337.
55. Ge, S. and C.-Y. Wang, *In Situ Imaging of Liquid Water and Ice Formation in an Operating PEFC during Cold Start*. Electrochemical and Solid-State Letters, 2006. **9**(11): p. A499-A503.
56. Ge, S., B. Yi, and P. Ming, *Experimental Determination of Electro-Osmotic Drag Coefficient in Nafion Membrane for Fuel Cells*. Journal of the Electrochemical Society, 2006. **153**(8): p. A1443-A1450.

57. Ise, M., K.D. Kreuer, and J. Maier, *Electroosmotic drag in polymer electrolyte membranes: an electrophoretic NMR study*. Solid State Ionics, 1999. **125**(1-4): p. 213-223.
58. Xie, G. and T. Okada, *Water Transport Behavior in Nafion 117 Membranes*. Journal of the Electrochemical Society, 1995. **142**(9): p. 3057-3062.
59. Ye, X. and C.-Y. Wang, *Measurement of Water Transport Properties Through Membrane Electrode Assemblies*. Journal of the Electrochemical Society, 2007. **154**(7): p. B683-B686.
60. Zawodzinski Jr, T.A., T.E. Springer, F. Uribe, and S. Gottesfeld, *Characterization of polymer electrolytes for fuel cell applications*. Solid State Ionics, 1993. **60**(1-3): p. 199-211.
61. Mérida, W.R., *PhD. Thesis: Diagnosis of PEMFC Stack Failures via Electrochemical Impedance Spectroscopy*, in *Department of Mechanical Engineering*. 2002, University of Victoria: Victoria. p. 204.
62. St-Pierre, J., *PEMFC In Situ Liquid-Water-Content Monitoring Status*. Journal of The Electrochemical Society, 2007. **154**(7): p. B724-B731.
63. Feindel, K.W., S.H. Bergens, and R.E. Wasylshen, *Insights into the Distribution of Water in a Self-Humidifying H₂/O₂ Proton-Exchange Membrane Fuel Cell Using ¹H NMR Microscopy*. J. Am. Chem. Soc., 2006. **128**(43): p. 14192-14199.
64. Feindel, K.W., L.P.A. LaRocque, D. Starke, S.H. Bergens, and R.E. Wasylshen, *In Situ Observations of Water Production and Distribution in an Operating H₂/O₂ PEM Fuel Cell Assembly Using ¹H NMR Microscopy*. J. Am. Chem. Soc., 2004. **126**(37): p. 11436-11437.
65. Teranishi, K., S. Tsushima, and S. Hirai, *Study of the Effect of Membrane Thickness on the Performance of Polymer Electrolyte Fuel Cells by Water Distribution in a Membrane*. Electrochemical and Solid-State Letters, 2005. **8**(6): p. A281-A284.
66. Tsushima, S., K. Teranishi, and S. Hirai, *Magnetic Resonance Imaging of the Water Distribution within a Polymer Electrolyte Membrane in Fuel Cells*. Electrochemical and Solid-State Letters, 2004. **7**(9): p. A269-A272.
67. Minard, K.R., V.V. Viswanathan, P.D. Majors, L.-Q. Wang, and P.C. Rieke, *Magnetic resonance imaging (MRI) of PEM dehydration and gas manifold flooding during continuous fuel cell operation*. Journal of Power Sources, 2006. **161**(2): p. 856-863.
68. Albertini, V.R., B. Paci, A. Generosi, S. Panero, M.A. Navarra, and M. di Michiel, *In Situ XRD Studies of the Hydration Degree of the Polymeric Membrane in a Fuel Cell*. Electrochemical and Solid-State Letters, 2004. **7**(12): p. A519-A521.
69. Sinha, P.K., P. Halleck, and C.-Y. Wang, *Quantification of Liquid Water Saturation in a PEM Fuel Cell Diffusion Medium Using X-ray Microtomography*. Electrochemical and Solid-State Letters, 2006. **9**(7): p. A344-A348.
70. Geiger, A.B., A. Tsukada, E. Lehmann, P. Vontobel, A. Wokaun, and G.G. Scherer, *In Situ Investigation of Two-Phase Flow Patterns in Flow Fields of PEFCs Using Neutron Radiography*. Fuel Cells, 2002. **2**(2): p. 92-98.
71. Bellows, R.J., M.Y. Lin, M. Arif, A.K. Thompson, and D. Jacobson, *Neutron Imaging Technique for In Situ Measurement of Water Transport Gradients within Nafion in Polymer Electrolyte Fuel Cells*. Journal of the Electrochemical Society, 1999. **146**(3): p. 1099-1103.

72. Hickner, M.A., N.P. Siegel, K.S. Chen, D.N. McBrayer, D.S. Hussey, D.L. Jacobson, and M. Arif, *Real-Time Imaging of Liquid Water in an Operating Proton Exchange Membrane Fuel Cell*. Journal of the Electrochemical Society, 2006. **153**(5): p. A902-A908.
73. Kowal, J.J., A. Turhan, K. Heller, J. Brenizer, and M.M. Mench, *Liquid Water Storage, Distribution, and Removal from Diffusion Media in PEFCs*. Journal of the Electrochemical Society, 2006. **153**(10): p. A1971-A1978.
74. Kramer, D., E. Lehmann, G. Frei, P. Vontobel, A. Wokaun, and G.G. Scherer, *An on-line study of fuel cell behavior by thermal neutrons*. Nuclear Instruments and Methods in Physics Research Section A: Accelerators, Spectrometers, Detectors and Associated Equipment, 2005. **542**(1-3): p. 52-60.
75. Kramer, D., J. Zhang, R. Shimoi, E. Lehmann, A. Wokaun, K. Shinohara, and G.G. Scherer, *In situ diagnostic of two-phase flow phenomena in polymer electrolyte fuel cells by neutron imaging: Part A. Experimental, data treatment, and quantification*. Electrochimica Acta, 2005. **50**(13): p. 2603-2614.
76. Ludlow, D.J., C.M. Calebrese, S.H. Yu, C.S. Dannehy, D.L. Jacobson, D.S. Hussey, M. Arif, M.K. Jensen, and G.A. Eisman, *PEM fuel cell membrane hydration measurement by neutron imaging*. Journal of Power Sources, 2006. **162**(1): p. 271-278.
77. Mosdale, R., G. Gebel, and M. Pineri, *Water profile determination in a running proton exchange membrane fuel cell using small-angle neutron scattering*. Journal of Membrane Science, 1996. **118**(2): p. 269-277.
78. Owejan, J.P., T.A. Trabold, D.L. Jacobson, D.R. Baker, D.S. Hussey, and M. Arif, *In situ investigation of water transport in an operating PEM fuel cell using neutron radiography: Part 2 - Transient water accumulation in an interdigitated cathode flow field*. International Journal of Heat and Mass Transfer, 2006. **49**(25-26): p. 4721-4731.
79. Pekula, N., K. Heller, P.A. Chuang, A. Turhan, M.M. Mench, J.S. Brenizer, and K. Unlu, *Study of water distribution and transport in a polymer electrolyte fuel cell using neutron imaging*. Nuclear Instruments and Methods in Physics Research Section A: Accelerators, Spectrometers, Detectors and Associated Equipment, 2005. **542**(1-3): p. 134-141.
80. Satija, R., D.L. Jacobson, M. Arif, and S.A. Werner, *In situ neutron imaging technique for evaluation of water management systems in operating PEM fuel cells*. Journal of Power Sources, 2004. **129**(2): p. 238-245.
81. Schneider, I.A., D. Kramer, A. Wokaun, and G.G. Scherer, *Spatially resolved characterization of PEFCs using simultaneously neutron radiography and locally resolved impedance spectroscopy*. Electrochemistry Communications, 2005. **7**(12): p. 1393-1397.
82. Trabold, T.A., J.P. Owejan, D.L. Jacobson, M. Arif, and P.R. Huffman, *In situ investigation of water transport in an operating PEM fuel cell using neutron radiography: Part 1 - Experimental method and serpentine flow field results*. International Journal of Heat and Mass Transfer, 2006. **49**(25-26): p. 4712-4720.
83. Turhan, A., K. Heller, J.S. Brenizer, and M.M. Mench, *Quantification of liquid water accumulation and distribution in a polymer electrolyte fuel cell using neutron imaging*. Journal of Power Sources, 2006. **160**(2): p. 1195-1203.
84. Zhang, J., D. Kramer, R. Shimoi, Y. Ono, E. Lehmann, A. Wokaun, K. Shinohara, and G.G. Scherer, *In situ diagnostic of two-phase flow phenomena in polymer electrolyte fuel cells by neutron imaging: Part B. Material variations*. Electrochimica Acta, 2006. **51**(13): p. 2715-2727.

85. Hakenjos, A., H. Muentler, U. Wittstadt, and C. Hebling, *A PEM fuel cell for combined measurement of current and temperature distribution, and flow field flooding*. Journal of Power Sources, 2004. **131**(1-2): p. 213-216.
86. Liu, X., H. Guo, and C. Ma, *Water flooding and two-phase flow in cathode channels of proton exchange membrane fuel cells*. Journal of Power Sources, 2006. **156**(2): p. 267-280.
87. Liu, X., H. Guo, F. Ye, and C.F. Ma, *Water flooding and pressure drop characteristics in flow channels of proton exchange membrane fuel cells*. Electrochimica Acta, 2007. **52**(11): p. 3607-3614.
88. Yamada, H., T. Hatanaka, H. Murata, and Y. Morimoto, *Measurement of Flooding in Gas Diffusion Layers of Polymer Electrolyte Fuel Cells with Conventional Flow Field*. Journal of the Electrochemical Society, 2006. **153**(9): p. A1748-A1754.
89. Sugiura, K., M. Nakata, T. Yodo, Y. Nishiguchi, M. Yamauchi, and Y. Itoh, *Evaluation of a cathode gas channel with a water absorption layer/waste channel in a PEFC by using visualization technique*. Journal of Power Sources, 2005. **145**(2): p. 526-533.
90. Tuber, K., D. Pocza, and C. Hebling, *Visualization of water buildup in the cathode of a transparent PEM fuel cell*. Journal of Power Sources, 2003. **124**(2): p. 403-414.
91. Weng, F.-B., A. Su, C.-Y. Hsu, and C.-Y. Lee, *Study of water-flooding behaviour in cathode channel of a transparent proton-exchange membrane fuel cell*. Journal of Power Sources, 2006. **157**(2): p. 674-680.
92. Yang, X.G., F.Y. Zhang, A.L. Lubawy, and C.Y. Wang, *Visualization of Liquid Water Transport in a PEFC*. Electrochemical and Solid-State Letters, 2004. **7**(11): p. A408-A411.
93. Zhang, F.Y., X.G. Yang, and C.Y. Wang, *Liquid Water Removal from a Polymer Electrolyte Fuel Cell*. Journal of the Electrochemical Society, 2006. **153**(2): p. A225-A232.
94. Diep, J., D. Kiel, J. St-Pierre, and A. Wong, *Development of a residence time distribution method for proton exchange membrane fuel cell evaluation*. Chemical Engineering Science, 2007. **62**(3): p. 846-857.
95. St-Pierre, J., A. Wong, J. Diep, and D. Kiel, *Demonstration of a residence time distribution method for proton exchange membrane fuel cell evaluation*. Journal of Power Sources, 2007. **164**(1): p. 196-202.
96. Barbir, F., H. Gorgun, and X. Wang, *Relationship between pressure drop and cell resistance as a diagnostic tool for PEM fuel cells*. Journal of Power Sources, 2005. **141**(1): p. 96-101.
97. He, W., G. Liu, and T. Van Nguyen, *Diagnostic Tool to Detect Electrode Flooding in Proton-Exchange Membrane Fuel Cells*. AIChE Journal, 2003. **49**(12): p. 3221-3228.
98. Buchi, F.N., B. Gupta, O. Haas, and G.G. Scherer, *Performance of Differently Cross-Linked, Partially Fluorinated Proton Exchange Membranes in Polymer Electrolyte Fuel Cells*. Journal of The Electrochemical Society, 1995. **142**(9): p. 3044-3048.
99. Buchi, F.N. and G.G. Scherer, *In-situ resistance measurements of Nafion(R) 117 membranes in polymer electrolyte fuel cells*. Journal of Electroanalytical Chemistry, 1996. **404**(1): p. 37-43.
100. Buchi, F.N. and G.G. Scherer, *Investigation of the Transversal Water Profile in Nafion Membranes in Polymer Electrolyte Fuel Cells*. Journal of the Electrochemical Society, 2001. **148**(3): p. A183-A188.
101. Gorgun, H., M. Arcak, and F. Barbir, *An algorithm for estimation of membrane water content in PEM fuel cells*. Journal of Power Sources, 2006. **157**(1): p. 389-394.

102. Watanabe, M., H. Igarashi, H. Uchida, and F. Hirasawa, *Experimental analysis of water behavior in Nafion(R) electrolyte under fuel cell operation*. Journal of Electroanalytical Chemistry, 1995. **399**(1-2): p. 239-241.
103. Fushinobu, K., K. Shimizu, N. Miki, and K. Okazaki, *Optical Measurement Technique of Water Contents in Polymer Membrane for PEFCs*. Journal of Fuel Cell Science and Technology, 2006. **3**(1): p. 13-17.
104. Matic, H., A. Lundblad, G. Lindbergh, and P. Jacobsson, *In Situ Micro-Raman on the Membrane in a Working PEM Cell*. Electrochemical and Solid-State Letters, 2005. **8**(1): p. A5-A7.
105. Patil, Y.P., T.A.P. Seery, M.T. Shaw, and R.S. Parnas, *In Situ Water Sensing in a Nafion Membrane by Fluorescence Spectroscopy*. Ind. Eng. Chem. Res., 2005. **44**(16): p. 6141-6147.
106. Li, G. and P.G. Pickup, *Measurement of single electrode potentials and impedances in hydrogen and direct methanol PEM fuel cells*. Electrochimica Acta, 2004. **49**(24): p. 4119-4126.
107. Ciureanu, M., *Effects of Nafion [registered trademark] dehydration in PEM fuel cells*. Journal of Applied Electrochemistry, 2004. **34**(7): p. 705-714.
108. Wilkinson, D.P., S.D. Knights, and M.V. Lauritzen., *Sensor Cell for an Electrochemical Fuel Cell Stack*. 2000, Ballard Power Systems Inc.: US 6,673,480. p. 59.
109. Wilkinson, D.P., S.D. Knights, and M.V. Lauritzen., *Sensor Cell for an Electrochemical Fuel Cell Stack*. 2000, Ballard Power Systems Inc.: WO 00/02282. p. 59.
110. Lauritzen, M.V., P. He, A.P. Young, S. Knights, V. Colbow, and P. Beattie, *Study of Fuel Cell Corrosion Processes Using Dynamic Hydrogen Reference Electrodes*. Journal of New Materials for Electrochemical Systems, 2007. **10**(3): p. 143-145.
111. Herrera, O., W. Mérida, and D.P. Wilkinson, *Sensing electrodes for failure diagnostics in fuel cells*. Journal of Power Sources, 2009. **190**(1): p. 103-109.
112. Herrera, O.E., W. Merida, and D.P. Wilkinson, *Method and Apparatus for Sensing Failure Modes in a Fuel Cell*. 2008: US Patent Application.
113. Herrera, O.E., W. Merida, and D.P. Wilkinson. *Sensing Electrodes for Failure Diagnostics in Fuel Cells*. in *Ulm Electrochemical Talks*. 2008. Ulm, Germany.
114. Herrera, O.E., W. Merida, and D.P. Wilkinson, *New Reference Electrode Approach for Fuel Cell Performance Evaluation*. ECS Transactions, 2008. **16**(2): p. 1915-1926.
115. Gerard, M., J.-P. Poirot-Crouvezier, D. Hissel, and M.-C. Pera, *Oxygen starvation analysis during air feeding faults in PEMFC*. International Journal of Hydrogen Energy, 2010. **35**(22): p. 12295-12307.
116. Ye, S., P. Beattie, S.A. Campbell, D.P. Wilkinson, B.R.C. Theobald, and D. Thompsett, *Anode catalyst compositions for a voltage reversal tolerant fuel cell*. 2007: US Patent Application 20070037042.
117. Knights, S., J. Taylor, D.P. Wilkinson, and D. Wainright, *Fuel cell anode structures for voltage reversal tolerance*. 2003: US Patent 6,517,962.
118. Colbow, K., M. Van der Geest, C. Longley, J. Muller, J. Roberts, J. St-Pierre, P. Urban, R. Wezel, D.P. Wilkinson, and J. Zhang, *Method and apparatus for operating an electrochemical fuel cell with periodic reactant starvation*. 2002.
119. Tsushima, S., T. Ikeda, T. Koido, and S. Hirai, *Investigation of Water Distribution in a Membrane in an Operating PEMFC by Environmental MRI*. Journal of the Electrochemical Society, 2010. **157**(12): p. B1814-B1818.

120. Fu, R.S., X. Zhang, and U. Pasaogullari, *Heat and Mass Transfer in Polymer Electrolyte Fuel Cells in Ultra-Low Humidity Operation*. ECS Transactions, 2009. **25**(1): p. 323-332.
121. Weng, F.-B., B.-S. Jou, C.-W. Li, A. Su, and S.-H. Chan, *The effect of low humidity on the uniformity and stability of segmented PEM fuel cells*. Journal of Power Sources, 2008. **181**(2): p. 251-258.
122. Mueller, J.T., P.M. Urban, and W.F. Hoelderich, *Impedance studies on direct methanol fuel cell anodes*. Journal of Power Sources, 1999. **84**(2): p. 157-160.
123. Sandhu, S.S., Y.A. Saif, and J.P. Fellner. *A reformer performance model for fuel cell applications*. 2004. Austin, TX, United States: American Institute of Chemical Engineers, New York, NY 10016-5991, United States.
124. Schneider, I.A., H. Kuhn, A. Wokaun, and G.G. Scherer, *Fast locally resolved electrochemical impedance spectroscopy in polymer electrolyte fuel cells*. Journal of the Electrochemical Society, 2005. **152**(10): p. 2092-2103.
125. Voss, H.H., D.P. Wilkinson, P.G. Pickup, M.C. Johnson, and V. Basura, *Anode water removal: a water management and diagnostic technique for solid polymer fuel cells*. Electrochimica Acta, 1995. **40**(3): p. 321-328.
126. Zhang, F.Y., X.G. Yang, and C.Y. Wang, *Liquid water removal from a polymer electrolyte fuel cell*. Journal of the Electrochemical Society, 2006. **153**(2): p. 225-232.
127. Knights, S.D., D.P. Wilkinson, S.A. Campbell, J.L. Taylor, J.M. Gascoyne, and T.R. Ralph, *Solid polymer fuel cell with improved voltage reversal tolerance*. 2005: US Patent 6,936,370.
128. Knights, S., J. Taylor, D.P. Wilkinson, and S.A. Campbell, *Supported catalysts for the anode of a voltage reversal tolerant fuel cell*. 2001: PCT WO 01/15254 A2.
129. Wilkinson, D.P., C. Chow, D. Allan, E. Johannes, J. Roberts, J. St-Pierre, C. Longley, and J. Chan, *Method and apparatus for operating an electrochemical fuel cell with periodic fuel starvation at the anode*. 2000: US Patent 6,096,448.
130. Liu, Z., L. Yang, Z. Mao, W. Zhuge, Y. Zhang, and L. Wang, *Behavior of PEMFC in starvation*. Journal of Power Sources, 2006. **157**(1): p. 166-176.
131. Kim, S., S. Shimpalee, and J.W. Van Zee, *The effect of stoichiometry on dynamic behavior of a proton exchange membrane fuel cell (PEMFC) during load change*. Journal of Power Sources, 2004. **135**(1-2): p. 110-121.
132. Liu, Z., L. Yang, Z. Mao, W. Zhuge, Y. Zhang, and L. Wang, *Behavior of PEMFC in starvation*. Journal of Power Sources. **In Press, Corrected Proof**.
133. Stumper, J., S.A. Campbell, D.P. Wilkinson, M.C. Johnson, and M. Davis, *In-situ methods for the determination of current distributions in PEM fuel cells*. Electrochimica Acta, 1998. **43**(24): p. 3773-3783.
134. Colbow, K.M., M. Van der Geest, C.J. Longley, J. Muller, J. Roberts, J. St-Pierre, P. Urban, R. Wezel, D.P. Wilkinson, and J. Zhang, *Method and apparatus for operating an electrochemical fuel cell with periodic reactant starvation*. 2002, Ballard Power Systems Inc.: United States. p. 23.
135. Reiser, C.A. and R.J. Balliet, *Fuel cell performance recovery by cyclic oxidant starvation*. 2005, UTC Fuel Cells, LLC: United States. p. 9.
136. Wilkinson, D.P., C.Y.F. Chow, D.e. Allan, E.P. Johannes, J.A. Roberts, J. St-Pierre, L.C. J., and J.K.K. Chan, *Method and Apparatus for Operating an Electrochemical Fuel Cell with Periodic Fuel Starvation at the Anode*. 2000, Ballard Power Systems Inc.: US 6,096,448.
137. Walsh, F., *A First Course in Electrochemical Engineering*. First ed. 1993, Romsey: The Electrochemical Consultancy Ltd. 381.

138. Stumper, J., M. Lohr, and S. Hamada, *Diagnostic tools for liquid water in PEM fuel cells*. Journal of Power Sources, 2005. **143**(1-2): p. 150-157.
139. Wheat, W.S., B.J. Clingerman, and M.K. Hortop, *Electronic by-pass control of gas around the humidifier to the fuel cell stack*. 2005, General Motors Corporation: US 6,884,534. p. 10.
140. Bosco, A.D. and M.H. Fronk, *Fuel Cell Flooding Detection and Correction*. 2000, General Motors Corporation: US 6,103,409. p. 9.
141. Mathias, M.F. and S.A. Grot, *System and Method for Controlling the Humidity Level of a Fuel Cell*. 2002, General Motors Corporation: US 6,376,111. p. 8.
142. Voss, H.H., D.P. Wilkinson, and D.S. Watkins, *Method and Apparatus for Removing Water from Electrochemical Fuel Cells*. 1993, Ballard Power Systems Inc.: US 5,260,143. p. 20.
143. Nelson, P.J., J.R. Forte, and A.K. Thompson, *Relative Humidity Sensor with Compensation for Changes in Pressure and Gas Composition*. 2004, General Motors Corporation: US 6,777,120. p. 8.
144. Shimotori, S., Y. Ogami, and M.L. Perry, *Fuel Cell System with Improved Humidification System*. 2005, UTC Fuel Cells, LLC.: US 6,869,709. p. 18.
145. Cargnelli, J., T.A. Simpson, R.C. Del Core, S. Burany, J. Ye, and R. Bazzarella, *System and Method for Management of Gas and Water in Fuel Cell System*. 2002, Hydrogenics Corporation: US 7,018,732. p. 10.
146. Aramaki, K., *Water Supply System for Fuel Cell Vehicle*. 2003, Nissan Motor Co., Ltd.: US 6,635,374. p. 12.
147. Yamanashi, F., *Water purge fuel cell system and method*. 2003, Nissan Motor Co. Ltd.: US 6,632,552. p. 16.
148. Hauer, K.-H., R. Potthast, T. Wuster, and D. Stolten, *Magnetotomography--a new method for analysing fuel cell performance and quality*. Journal of Power Sources, 2005. **143**(1-2): p. 67-74.
149. Buchi, F.N., A.B. Geiger, and R.P. Neto, *Dependence of current distribution on water management in PEFC of technical size*. Journal of Power Sources, 2005. **145**(1): p. 62-67.
150. Ghosh, P.C., T. Wuster, H. Dohle, N. Kimiaie, J. Mergel, and D. Stolten, *In situ approach for current distribution measurement in fuel cells*. Journal of Power Sources, 2006. **154**(1): p. 184-191.
151. Natarajan, D. and T. Van Nguyen, *Current distribution in PEM fuel cells. Part 1: Oxygen and fuel flow rate effects*. AIChE Journal, 2005. **51**(9): p. 2587-2598.
152. Myrdal, R., *Electrochemistry and Characteristics of Embeddable Reference Electrodes for Concrete: (EFC 43)*. 2007, Woodhead Publishing.
153. Ives, D.J. and G.J. Janz, *Reference Electrodes, Theory and Practice*. 1961, N.Y.: Academic Press.
154. Schmickler, W., *Elektrochemie: Instrumental Methods in Electrochemistry*. Southampton Electrochemistry Group. R. Greef, R. Peat, L. M. Peter, D. Pletcher und J. Robinson. Halsted Press 1985. 443 S., Tab., £ 49,50. ISBN 0 853128758. Nachrichten aus Chemie, Technik und Laboratorium, 1986. **34**(7): p. 667-667.
155. Newman, J., *Current Distribution on a Rotating Disk below the Limiting Current*. Journal of the Electrochemical Society, 1966. **113**(12): p. 1235-1241.
156. West, A.C. and J. Newman, *Interpretation of Kinetic Rate Data Taken in a Channel Flow Cell*. Journal of the Electrochemical Society, 1989. **136**(12): p. 3755-3759.
157. Adler, S.B., *Reference Electrode Placement in Thin Solid Electrolytes*. Journal of the Electrochemical Society, 2002. **149**(5): p. E166-E172.

158. Chan, S.H., X.J. Chen, and K.A. Khor, *Reliability and accuracy of measured overpotential in a three-electrode fuel cell system*. Journal of Applied Electrochemistry, 2001. **31**(10): p. 1163-1170.
159. He, W. and T. Van Nguyen, *Edge Effects on Reference Electrode Measurements in PEM Fuel Cells*. Journal of the Electrochemical Society, 2004. **151**(2): p. A185-A195.
160. Liu, Z., J.S. Wainright, W. Huang, and R.F. Savinell, *Positioning the reference electrode in proton exchange membrane fuel cells: calculations of primary and secondary current distribution*. Electrochimica Acta, 2004. **49**(6): p. 923-935.
161. Krishnan, V.V., S. McIntosh, R.J. Gorte, and J.M. Vohs, *Measurement of electrode overpotentials for direct hydrocarbon conversion fuel cells*. Solid State Ionics, 2004. **166**(1-2): p. 191-197.
162. Adler, S.B., *Factors Governing Oxygen Reduction in Solid Oxide Fuel Cell Cathodes*. Chem. Rev., 2004. **104**(10): p. 4791-4844.
163. Kato, T., A. Momma, Y. Kaga, S. Nagata, Y. Kasuga, and M. Kitase, *Influence of cell configuration on measuring interfacial impedances between a solid electrolyte and an electrode*. Solid State Ionics, 2000. **132**(3-4): p. 287-295.
164. Gerteisen, D., *Realising a reference electrode in a polymer electrolyte fuel cell by laser ablation*. Journal of Applied Electrochemistry, 2007. **37**(12): p. 1447-1454.
165. Kuhn, H., B. Andreaus, A. Wokaun, and G.G. Scherer, *Electrochemical impedance spectroscopy applied to polymer electrolyte fuel cells with a pseudo reference electrode arrangement*. Electrochimica Acta, 2006. **51**(8-9): p. 1622-1628.
166. Kuhn, H., A. Wokaun, and G.G. Scherer, *Exploring single electrode reactions in polymer electrolyte fuel cells*. Electrochimica Acta, 2007. **52**(6): p. 2322-2327.
167. Li, G. and P.G. Pickup, *Dependence of Electrode Overpotentials in PEM Fuel Cells on the Placement of the Reference Electrode*. Electrochemical and Solid-State Letters, 2006. **9**(5): p. A249-A251.
168. Siroma, Z., R. Kakitsubo, N. Fujiwara, T. Ioroi, S.-I. Yamazaki, and K. Yasuda, *Compact dynamic hydrogen electrode unit as a reference electrode for PEMFCs*. Journal of Power Sources, 2006. **156**(2): p. 284-287.
169. Siroma, Z., J. Takahashi, K. Yasuda, K. Tanimoto, M. Inaba, and A. Tasaka, *Diagnostics of Cathode Flooding in a Segmented PEMFC with Local Reference Electrodes*. ECS Transactions, 2006. **3**(1): p. 1041-1047.
170. Ticianelli, E.A., C.R. Derouin, A. Redondo, and S. Srinivasan, *Methods to Advance Technology of Proton Exchange Membrane Fuel Cells*. Journal of the Electrochemical Society, 1988. **135**(9): p. 2209-2214.
171. Andreaus, B., A.J. McEvoy, and G.G. Scherer, *Analysis of performance losses in polymer electrolyte fuel cells at high current densities by impedance spectroscopy*. Electrochimica Acta, 2002. **47**(13-14): p. 2223-2229.
172. Andreaus, B. and G.G. Scherer, *Proton-conducting polymer membranes in fuel cells--humidification aspects*. Solid State Ionics, 2004. **168**(3-4): p. 311-320.
173. Wilkinson, D.P. and J. St-Pierre, *In-plane gradients in fuel cell structure and conditions for higher performance*. Journal of Power Sources, 2003. **113**(1): p. 101-108.
174. Brett, D.J.L., S. Atkins, N.P. Brandon, V. Vesovic, N. Vasileiadis, and A. Kucernak, *Localized Impedance Measurements along a Single Channel of a Solid Polymer Fuel Cell*. Electrochemical and Solid-State Letters, 2003. **6**(4): p. A63-A66.

175. Cleghorn, S.J.C., C.R. Derouin, M.S. Wilson, and S. Gottesfeld, *A printed circuit board approach to measuring current distribution in a fuel cell*. Journal of Applied Electrochemistry, 1998. **28**(7): p. 663-672.
176. Mench, M.M., Q.L. Dong, and C.Y. Wang, *In situ water distribution measurements in a polymer electrolyte fuel cell*. Journal of Power Sources, 2003. **124**(1): p. 90-98.
177. Noponen, M., T. Hottinen, T. Mennola, M. Mikkola, and P. Lund, *Determination of mass diffusion overpotential distribution with flow pulse method from current distribution measurements in a PEMFC*. Journal of Applied Electrochemistry, 2002. **32**(10): p. 1081-1089.
178. Rieke, P.C. and N.E. Vanderborgh, *Thin Film Electrode Arrays for Mapping the Current-Voltage Distributions in Proton-Exchange-Membrane Fuel Cells*. Journal of the Electrochemical Society, 1987. **134**(5): p. 1099-1104.
179. Schneider, I.A., H. Kuhn, A. Wokaun, and G.G. Scherer, *Fast Locally Resolved Electrochemical Impedance Spectroscopy in Polymer Electrolyte Fuel Cells*. Journal of The Electrochemical Society, 2005. **152**(10): p. A2092-A2103.
180. Schneider, I.A., H. Kuhn, A. Wokaun, and G.G. Scherer, *Study of Water Balance in a Polymer Electrolyte Fuel Cell by Locally Resolved Impedance Spectroscopy*. Journal of the Electrochemical Society, 2005. **152**(12): p. A2383-A2389.
181. Mitsuda, K. and T. Murahashi, *Polarization Study of a Fuel Cell with Four Reference Electrodes*. Journal of the Electrochemical Society, 1990. **137**(10): p. 3079-3085.
182. Bridgeman, O.C. and E.W. Aldrich, *Vapor Pressure Tables for Water*. J. Heat Transfer, 1964. **86**: p. 279-286.
183. Spry, D.B. and M.D. Fayer, *Proton Transfer and Proton Concentrations in Protonated Nafion Fuel Cell Membranes*. The Journal of Physical Chemistry B, 2009. **113**(30): p. 10210-10221.
184. Hashibon, A., S. Raz, and I. Riess, *Preferred position for the reference electrode in solid state electrochemistry*. Solid State Ionics, 2002. **149**(3-4): p. 167-176.
185. Zhang, J., R.N. Carter, P.T. Yu, W. Gu, F.T. Wagner, and H.A. Gasteiger, *FUEL CELLS - PROTON-EXCHANGE MEMBRANE FUEL CELLS | Catalysts: Life-Limiting Considerations*, in *Encyclopedia of Electrochemical Power Sources*, x00Fc and G. rgen, Editors. 2009, Elsevier: Amsterdam. p. 626-638.
186. Lv, H., S. Mu, N. Cheng, and M. Pan, *Nano-silicon carbide supported catalysts for PEM fuel cells with high electrochemical stability and improved performance by addition of carbon*. Applied Catalysis B: Environmental, 2010. **100**(1-2): p. 190-196.
187. Basu, S., M.W. Renfro, and B.M. Cetegen, *Spatially resolved optical measurements of water partial pressure and temperature in a PEM fuel cell under dynamic operating conditions*. Journal of Power Sources, 2006. **162**(1): p. 286-293.
188. Pharoah, J.G. and O.S. Burheim, *On the temperature distribution in polymer electrolyte fuel cells*. Journal of Power Sources, 2010. **195**(16): p. 5235-5245.
189. Darwent, B.d.B., *Bond Dissociation Energies in Simple Molecules*. 1970, National Standard Reference Data System.

A APPENDICES

A.1 FUEL CELL AND TEST STATION ASSEMBLY FOR TESTING

The fuel cell developed with Tandem technologies, shown in Figure A-1, is composed of a set of 4 plates when used in cross-flow configuration and a set of 5 plates when used in co-flow configuration. The plates for cross-flow are: anode coolant, anode, cathode and blank plate, as shown in Figure A-1 and Figure A-2. The plates for co-flow are: anode coolant, shunt plate, anode, cathode and blank plate, as shown in Figure A-3.

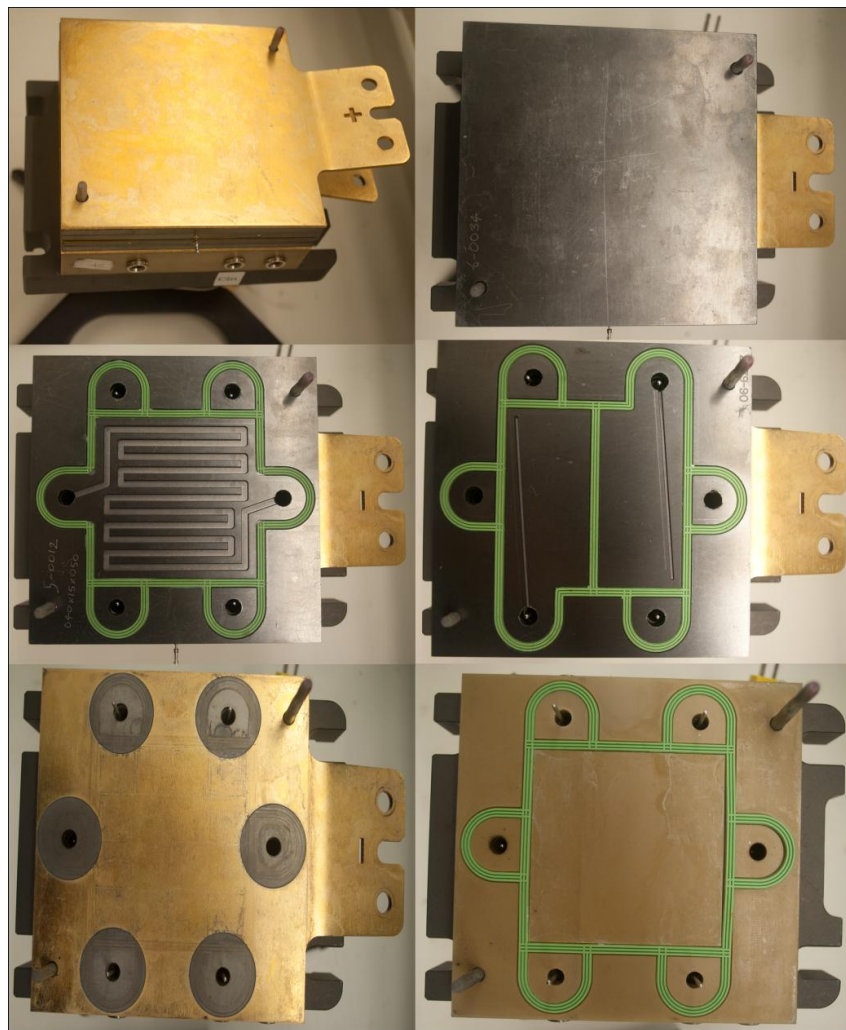


Figure A-1 Fuel Cell in cross-flow configuration

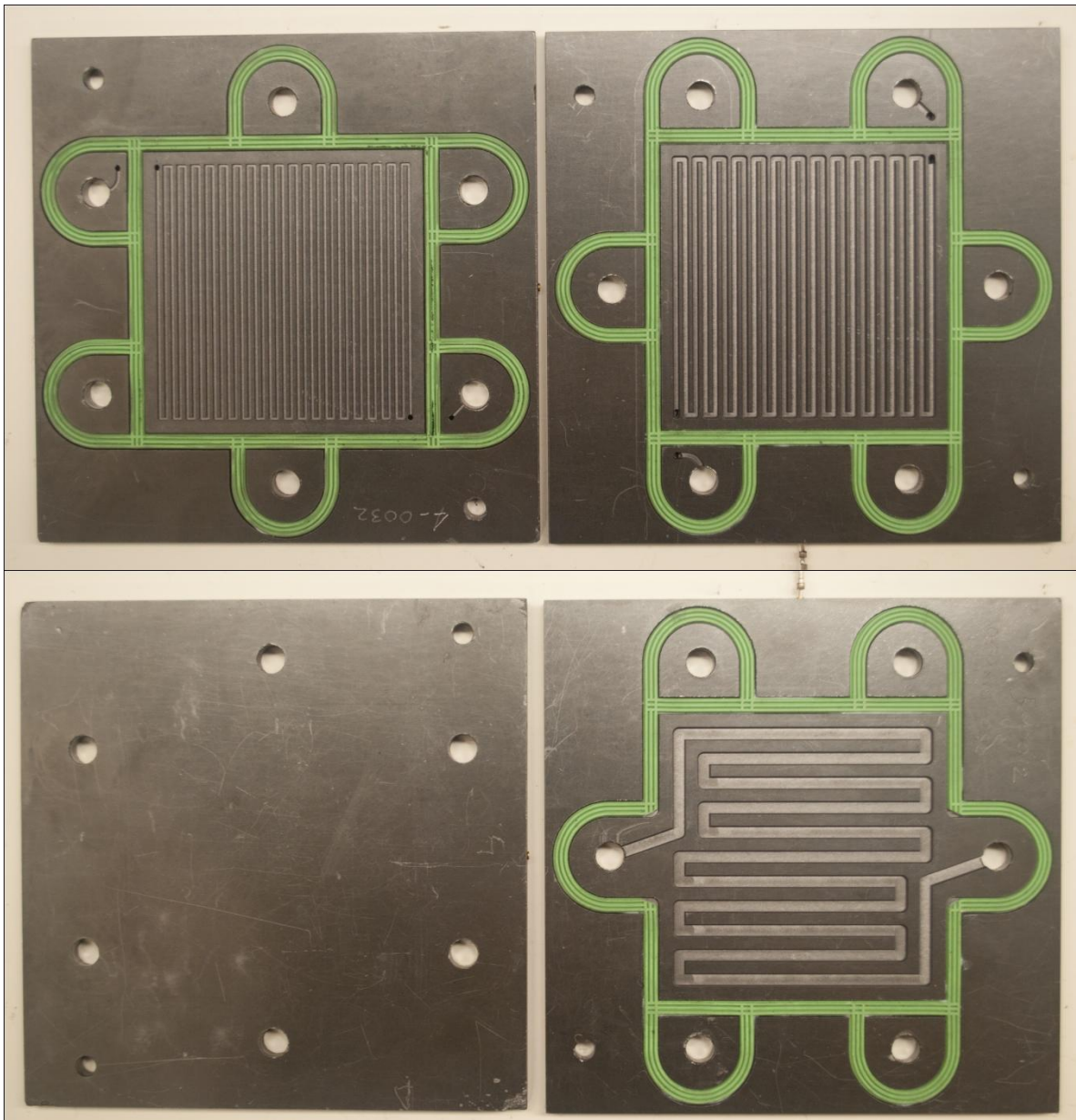


Figure A-2 Fuel Cell plates for cross-flow configuration

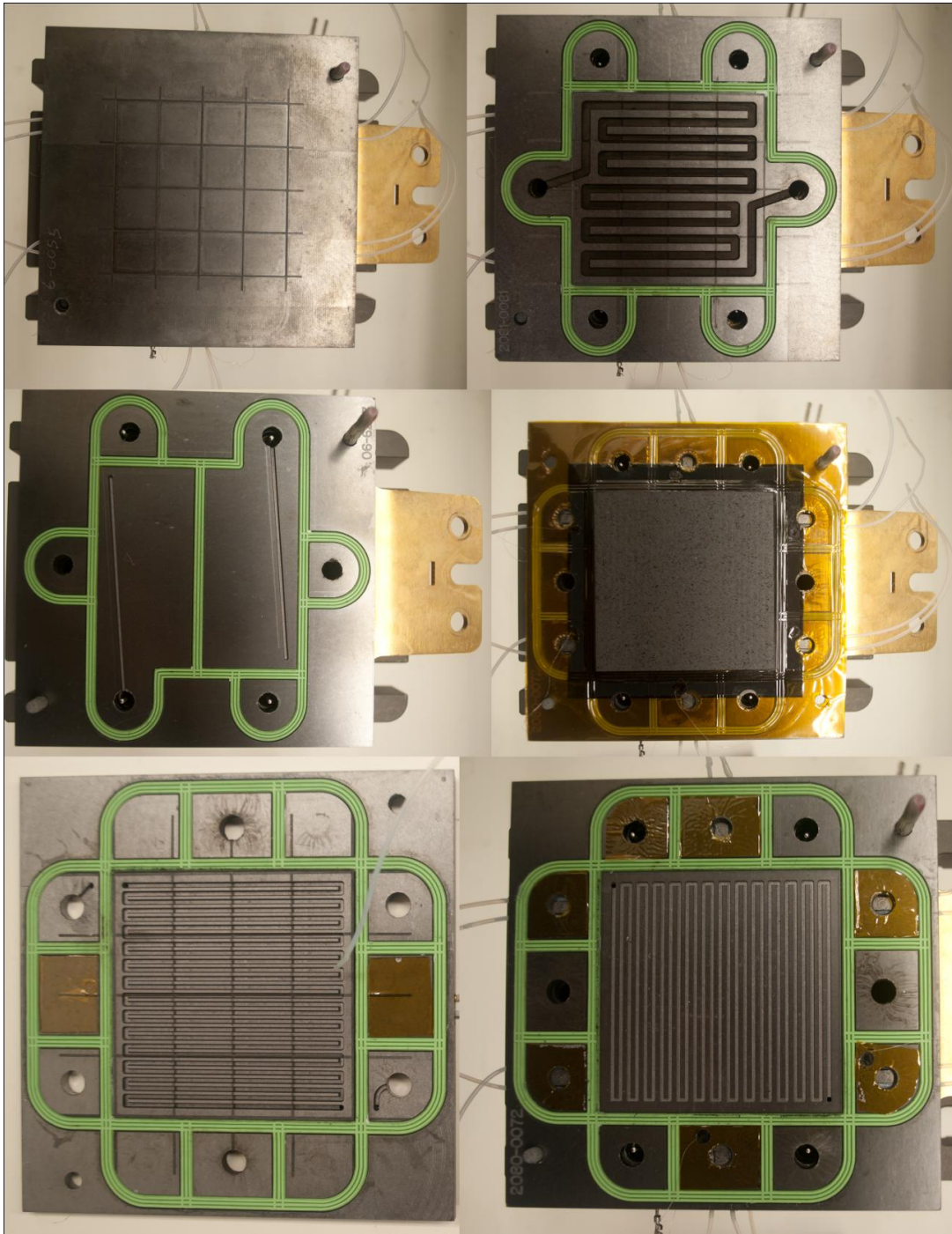


Figure A-3 Fuel Cell in co-flow configuration with reference electrodes and segmentation on the cathode.

The 500 W Arbin test station used for fuel cell testing is shown in Figure A-4. The 50 W Arbin test station is shown in . The test stations are comprised of a series of mass flow controllers that send the gases to some heaters and humidifiers. The humidifiers need a DI-water supply. The humidified gases are delivered into the fuel cell by heated hoses.

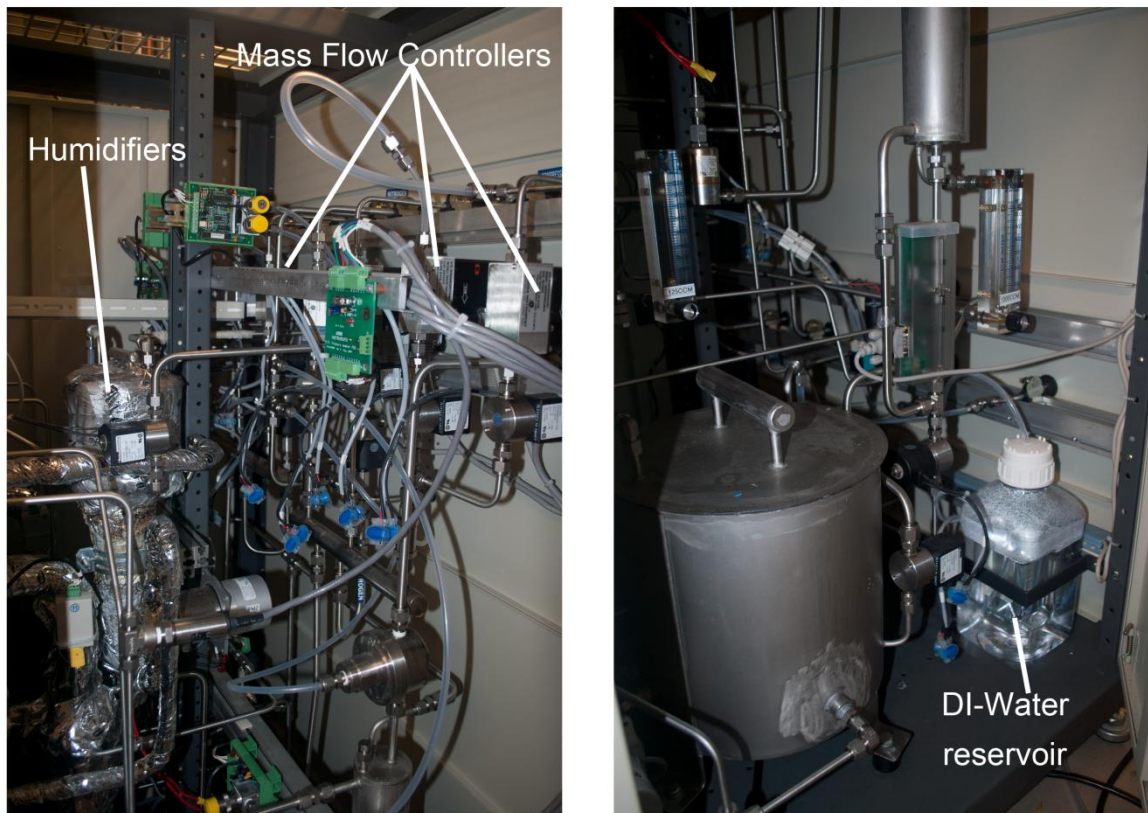


Figure A-4 Test station components

A.2 FUEL CELL TESTING PROCEDURES

A.2.1 Conditioning of MEA⁶

The following protocol is for the fuel cells and membrane electrode assemblies (MEA) described in Chapter 4. If any of these components changes then this protocol should be taken just as a guide. The volumetric flow rates of the reactant gases can be calculated as follows:

$$Q(Ls^{-1}) = \frac{M(gmol^{-1}) \cdot I(A) \cdot v}{z \cdot F(Cmol^{-1}) \cdot \rho(kgm^{-3}) \cdot \varphi} \cdot \frac{60 s}{1 min} \quad (A-1)$$

Calculate the volumetric flow at 500 mAcm^{-2} with a stoichiometric ratio for air ($v=2$) and hydrogen ($v=1.5$). For a fuel cell with an active area of 49 cm^2 (like the used in this work), the values for air = 0.821 SLPM and for hydrogen = 0.256 SLPM. Set the test station at that flow and start pressurizing the cell up to 2.04 atm in increments of 0.5 atm.

When the pressure is reached, set a current density ramp that takes 3 h to reach 500 mAcm^{-2} (i.e., $0.00680555556 \text{ mAs}^{-1}$). The current is set at this low current density so it doesn't reach potential values of less than 0.5 V.

At the same time, set the test station to the following typical temperature conditions:

$$T_{\text{cell}} = 348 \text{ K}$$

$$T_{\text{gases}} = 348 \text{ K}$$

$$\text{DPT} = 348 \text{ K (100\% RH for both sides)}$$

Once the temperature conditions are achieved, start cycling the cell between open circuit, 0.3 V, 0.6 V and 0.9 V. Each potential should be set for 10 minutes and keep cycling for 2 hours.

⁶ Adapted from Mauricio Blanco's Protocol

Operate the cell at a load that gives about 0.5 V until the cell's voltage has stabilized for more than an hour, this usually takes between 6 to 8 hours. By stabilized voltage is meant that the variations in the cell voltage are smaller than ± 10 mV for at least one hour.

These steps can also be used when conditioning an MEA that is old and has not been used for more than 3 days. In general, the total time for MEA re-conditioning for an old MEA is shorter than with a new MEA.

A.2.2 Polarization Curves⁷

The following protocol is for the fuel cells and membrane electrode assemblies (MEA) described in Chapter 4. If any of these components changes then this protocol should be taken just as a guide. This protocol is meant for polarization curve tests with standard materials (i.e., commercially available). For example, SGL Carbon GDLs, Toray carbon fiber papers, and Primea[®] Gore CCMs. Depending on the flow field channels used in both anode and cathode flow field plates the cell's overall performance may change substantially. Therefore, certain stages of this protocol may change accordingly (e.g., the amount of current density points). The minimum rate of data acquisition is 1 point every 2 seconds. The recommended rate is 1 point per second (in some cases an even faster rate is preferable). The steps for a polarization curve are:

Set the desired operating conditions (pressure and temperatures)

Once the operating conditions are ready, operate the fuel cell at the following current densities (in mAcm^{-2}) and leave the cell at each point for at least 15 minutes (i.e., at constant current):

⁷ Adapted from Mauricio Blanco's Protocol

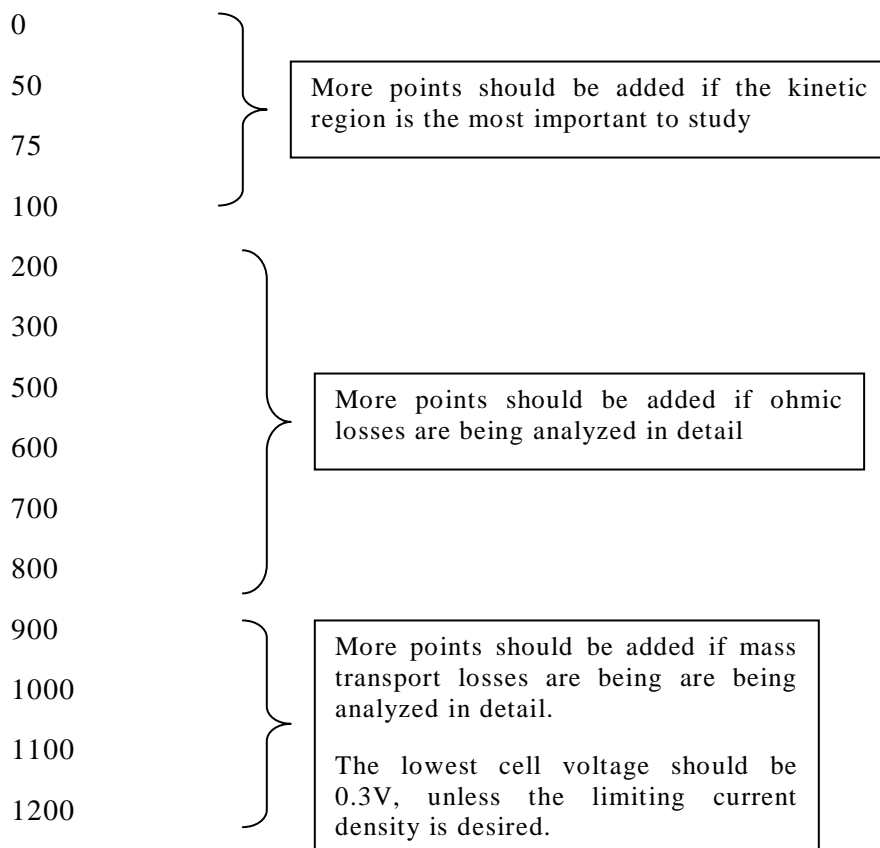


Figure A-5 Current density set points for polarization curve

The cell voltage recorded at each current measurement is averaged over a time period of at least 3 minutes corresponding to the steady state condition of the cell. Depending on the MEA and flow fields that are used the amount of points will change, therefore, the current densities shown here are just examples of the typical points that are necessary in order to cover the most important areas of the polarization curve. In addition, in some tests it is desired to study the limiting current density of the fuel cell, thus, it may be necessary to run the cell at very high current densities in which the cell's voltage would be less than 0.3 V.

The value for the open circuit voltage should be recorded after the highest current density point is completed. After this, the fuel cell has to be tested at least at six more current densities, in a descending order from high to low current values, for at least 15 to 30 minutes at each point. This was performed to compare the hysteresis associated with

increasing or decreasing current densities. This is especially important when testing at low humidity conditions since the cell could be degrading. If the difference between the increasing and decreasing cases is less than or equal to 10 mV at a given current value then the polarization curve is completed. If the difference between the cases is greater than 10 mV then the polarization curve should be repeated. The most common current densities tested in a descending order are 1000, 700, 500, and 100 mAcm⁻².

At flooding conditions (dew-point temperature greater than the temperature of the gases) it is necessary to purge the cell after each current density, thus, the water accumulated in the previous point does not affect the future current loads. In addition, these purging steps may also have to be used when materials more susceptible to water flooding are used (e.g., CFPs with no PTFE treatment) even at conditions in which the temperature of the gases are greater than the dew-point temperatures.

A.3 CALCULATIONS

A.3.1 Enthalpy from Bond Dissociation Energies

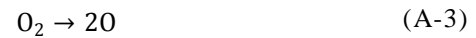
	kJmol ⁻¹
H-H	435.93
H-O	428.19
H-OH	498.73
O-O	498.34

Table A-1 Bond dissociation energies of molecules from the National Institute of Standards and Technology [189].



$$\Delta H_{\text{dissociation}}^0 = 435.93 \text{ kJmol}^{-1}$$

Cathode dissociation reactions:



$$\Delta H^0_{\text{dissociation}} = \Delta H^0_{\text{H}_2\text{O}} + \Delta H^0_{\text{HO}} - 0.5 \Delta H^0_{\text{O}_2} = -718.18 \text{ kJmol}^{-1} \quad (\text{A-6})$$

A.3.2 Tafel Plot Calculations

In order to obtain and evaluate kinetic parameters from current and activation overpotential values, a plot of $\log i$ vs. η_{Act} , known as a Tafel plot, can be used. This approximation was used to obtain the kinetic parameters in Chapter 7. From this plot it is possible to calculate the Tafel slope (b) and the exchange current density (i_0), as shown in Figure A-1.

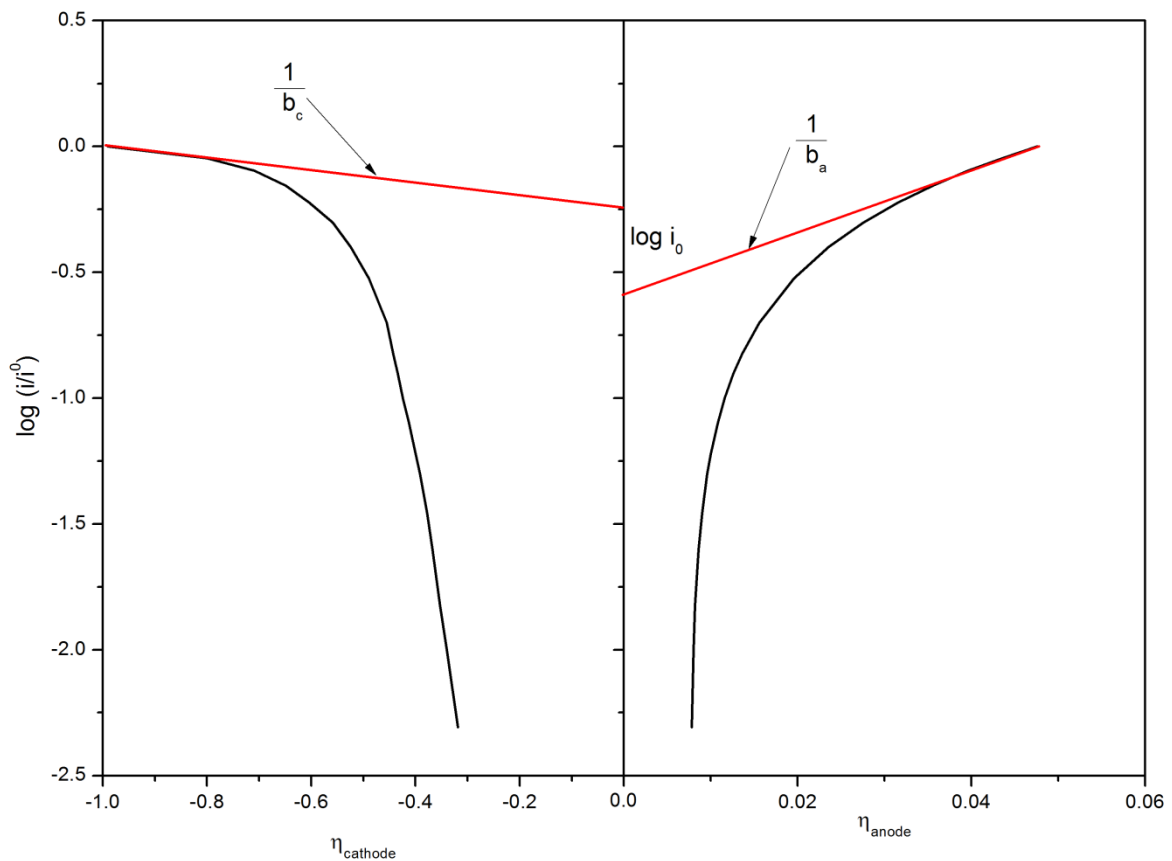


Figure A-6 Tafel plots for the anodic and cathodic branches of the current-overpotential curve for $H_2 + 1/2 O_2 \rightleftharpoons H_2O$, the fuel cell reaction evaluated in this thesis. The Tafel plot shown is the calculated from the results obtained during normal conditions.

A.3.3 Overpotential calculations

Sample calculation for overpotentials based on the potential response measurements with the different gases:

Gas	Anode		Cathode	
	E (V @ 1 Acm ⁻²)	R (Ωcm ²)	E (V @ 1 Acm ⁻²)	R (Ωcm ²)
Oxygen	0.0447	0.0354	0.5872	0.0783
Air	0.1060	0.0411	0.3962	0.0749

Table A-2 Measured potential and high frequency resistance values at 1 Acm⁻²

Ohmic losses and iR correction

$$E_{c,O_2*} = E_{c,O_2} + E_{c,O_2,\Omega} = E_{c,O_2} + iR_{c,O_2} = 0.5872 V + 0.0783 V = 0.6655 V \quad (A-7)$$

$$E_{c,Air*} = E_{c,O_2} + E_{c,Air,\Omega} = E_{c,Air} + iR_{c,Air} = 0.3962 V + 0.0749 V = 0.4745 V \quad (A-8)$$

$$E_{a,O_2*} = E_{a,O_2} + E_{a,O_2,\Omega} = E_{a,O_2} - iR_{c,O_2} = 0.0447 V - 0.0354 V = 0.0092 V \quad (A-9)$$

$$E_{a,Air*} = E_{a,Air} + E_{a,Air,\Omega} = E_{a,Air} - iR_{c,Air} = 0.1060 V - 0.0411 V = 0.0706 V \quad (A-10)$$

Activation overpotential

$$\eta_{Act,c} = E^0 - E_{c,O_2*} = 1.212 V - 0.6655 V = 0.5465 V \quad (A-11)$$

$$-\eta_{Act,a} = E_{a,O_2*} - E^0 = 0.0092 V - (-0.068 V) = 0.0772 V \quad (A-12)$$

Diffusion overpotential

$$\eta_{d,c} = E_{c,O_2*} - E_{c,Air*} = 0.6655 V - 0.4745 V = 0.1910 V \quad (A-13)$$

$$-\eta_{d,a} = E_{a,Air*} - E_{a,O_2*} = 0.0706 V - 0.0092 V = 0.0614 V \quad (A-14)$$

A.4 SEGMENTED CELL

The segmented cell test system consisted of a set of segmented plates designed in collaboration with Tandem Technologies Ltd. The active area of the plates was divided in 16 segments as shown in Figure A-2. The process consisted of cutting a groove for the segments, then filling them with epoxy and then machining them as shown in the diagram in Figure A-3.

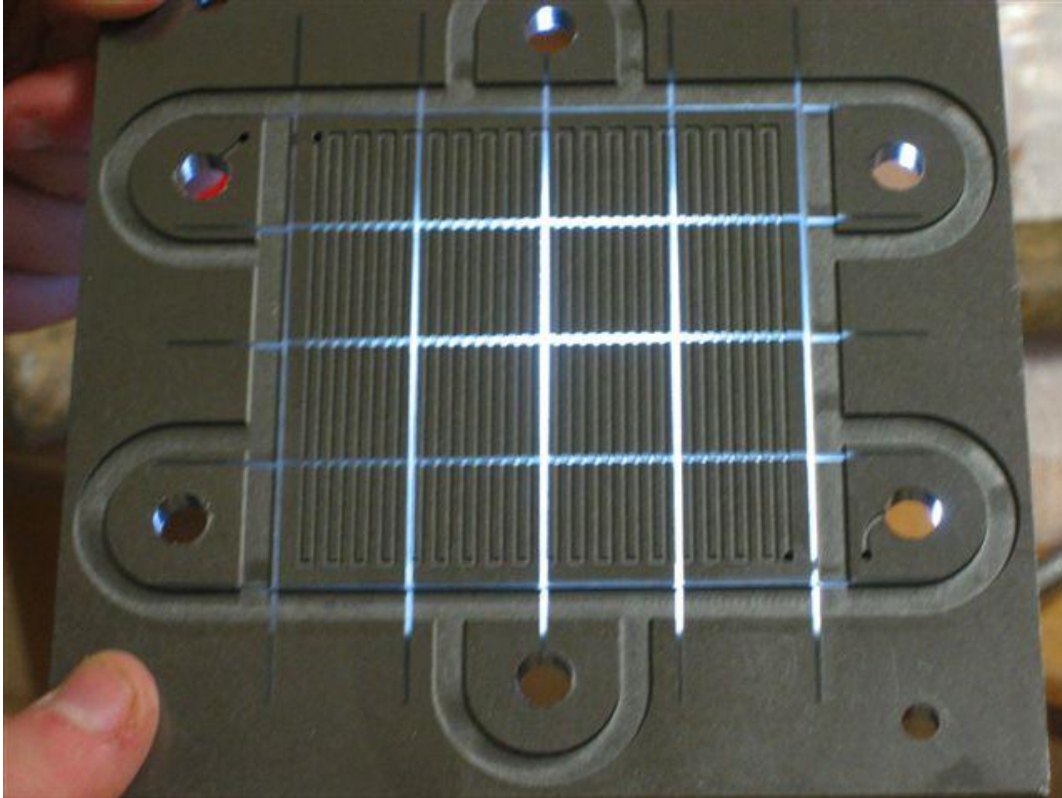


Figure A-7 Segmented fuel cell graphite plate.

The current collection was done with a printed circuit board designed in collaboration with Pronine Electronics Design. The PCB consisted of 16 gold plated segments each one with a thermistor for temperature measurements as previously shown in Figure 4-6. The current from the segments then passed through a resistor where voltage was measured and read by the National Instruments system as shown in the following diagrams:

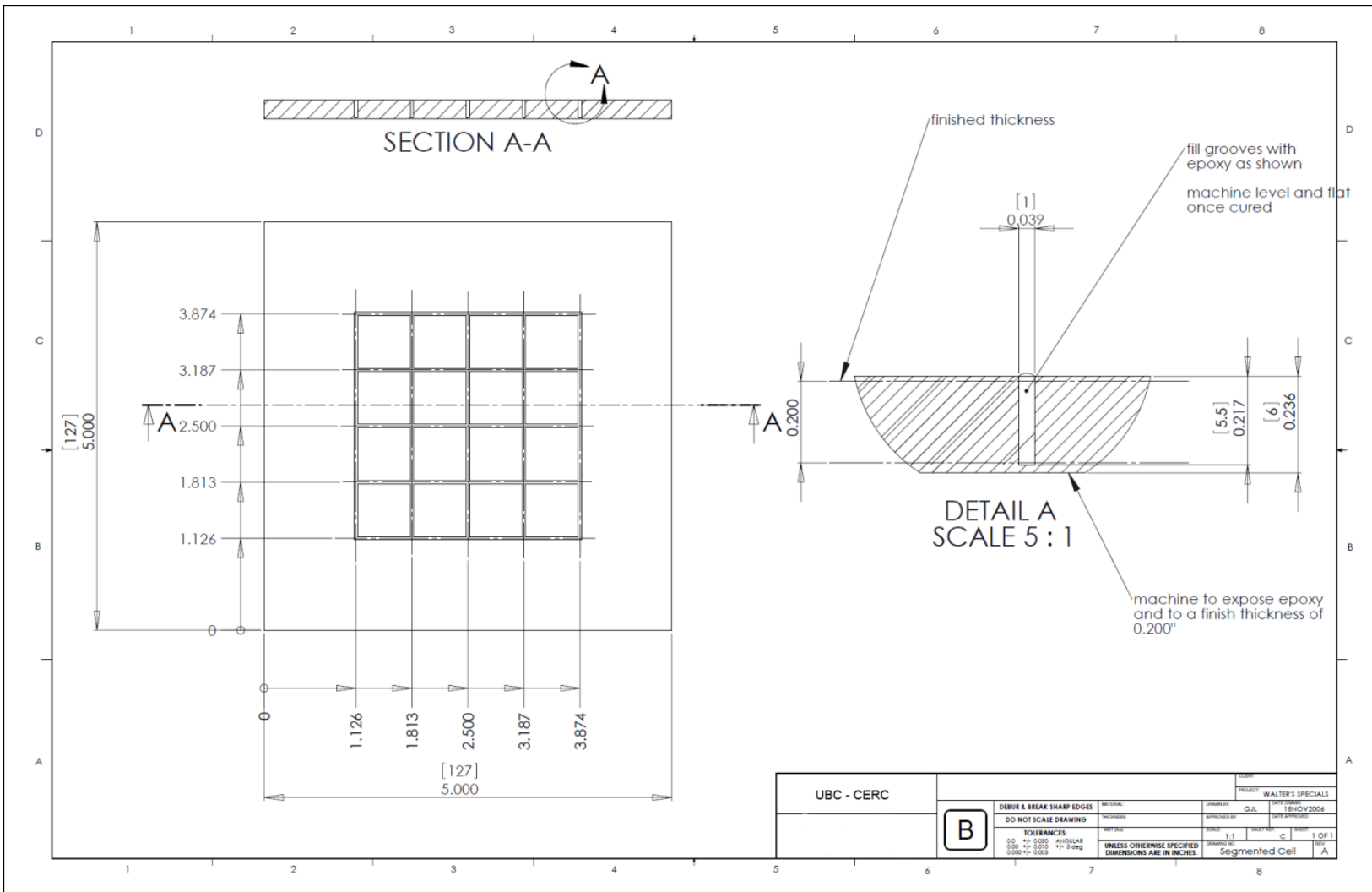


Figure A-8 Diagram for the machining of segmented graphite plates.

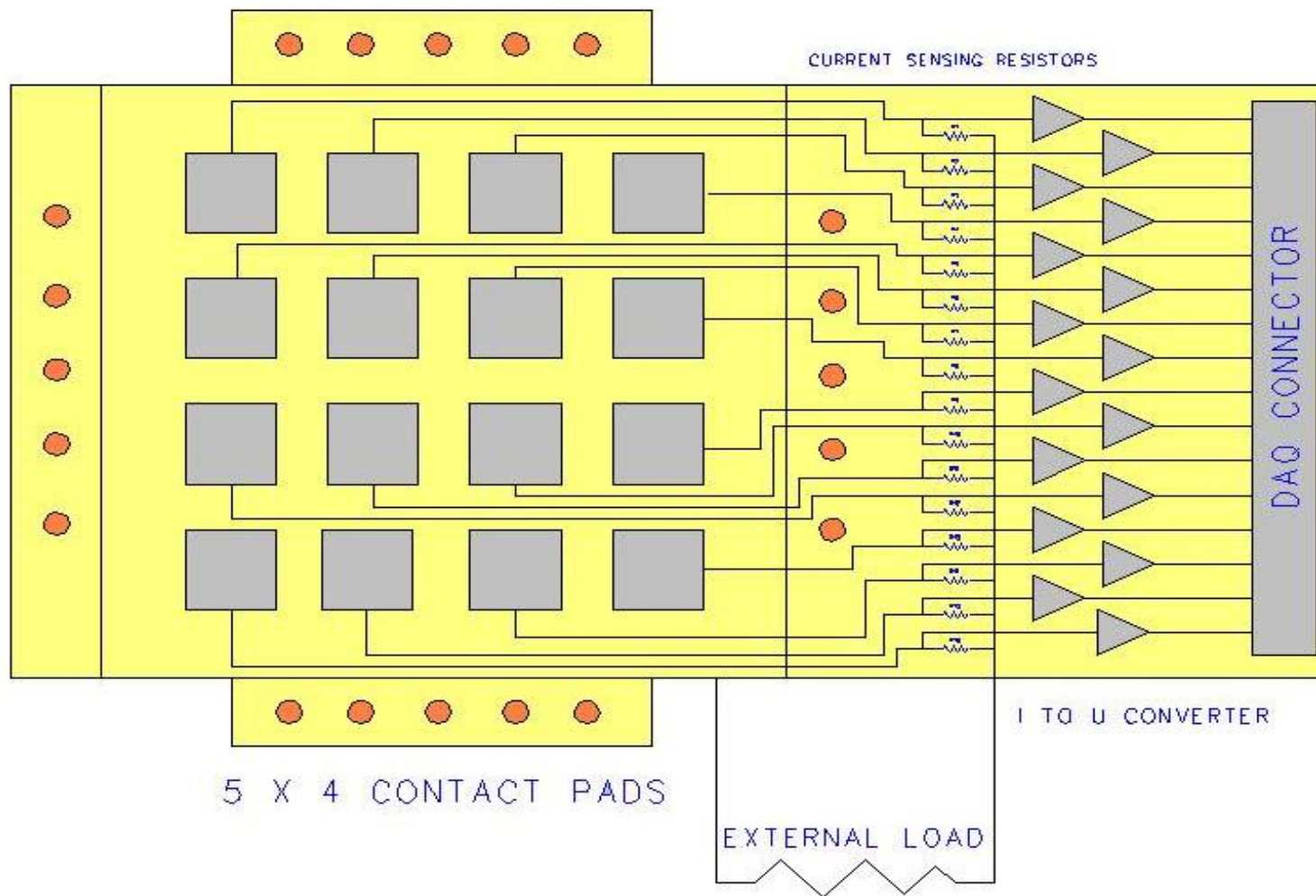


Figure A-9 Segmented current collector diagram

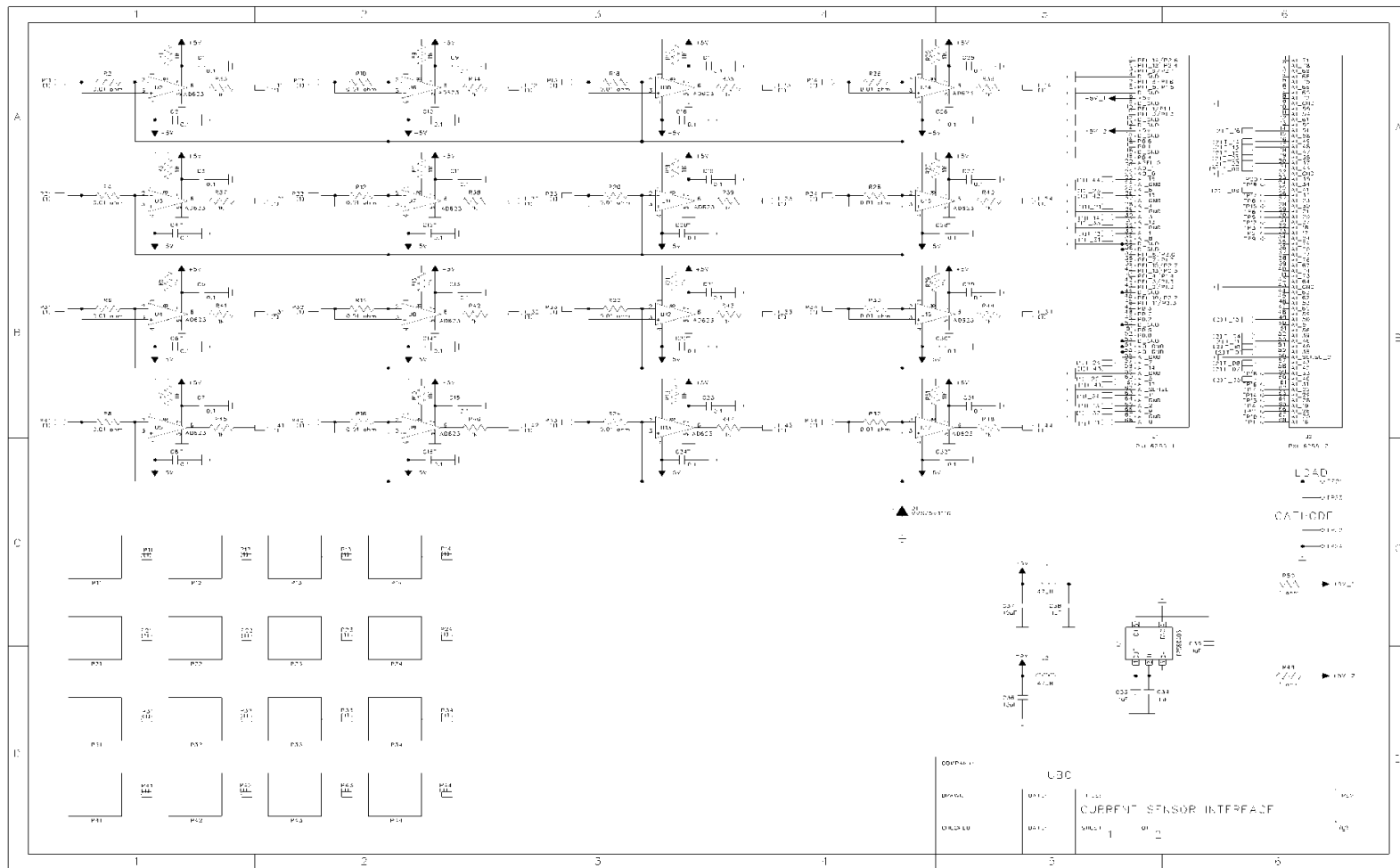


Figure A-10 Segmented cell current collector PCB detailed diagram

Bill Of Materials

Item	Qty	Reference	Description	Value	PART NUMBER	Manufacturer	Digikey	Mouser
2	33	C1-32 C40	CAP .1UF 16V CERAMIC X7R 0603	0.1	ECJ-1VB1C104K	Panasonic	PCC1762CT-ND	
3	3	C36-37 C39	CAP 10UF 6.3V CERAMIC X5R 0805	10uF	ECJ-2FB0J106M	Panasonic	PCC2225CT-ND	
4	4	C33-35 C38	CAP CER 1.0UF 16V 10% X7R 0805	1uF	GRM21BR71C105KA01L	Murata	490-1691-1-ND	
6	1	D1	DIODE ZENER 5.1V 500MW SOD-123		MMSZ5V1T1G	On	MMSZ5V1T1GOSCT-ND	
9	2	J1 J2	D-Subminiature Connector PLUG 68P		2-5174225-5	Tyco		571-2-5174225-5
7	2	L1-2	INDUCTOR, SMD	47uH	PM1210-470J-RC	JW Miller	M8549CT-ND	
11	16	R2 R4 R6 R8 R10 R12 R14 R16 R18 R20 R22 R24 R26 R28 R30 R32	RES .01 OHM 1W 1% 2010 SMD	0.01 ohm	CSRN 1 0.01 1% R	Stackpole	CSRN10.01FRCT-ND	
12	2	R49-50	RESISTOR 1.0 OHM 1/10W 5% 0603	1 ohm	ERJ-3GEYJ1R0V	Panasonic	P1.0GCT-ND	
13	16	R1 R3 R5 R7 R9 R11 R13 R15 R17 R19 R21 R23 R25 R27 R29 R31	RES 11.0K OHM 1/10W 1% 0603 SMD	11K	ERJ-3EKF1102V	Panasonic	P11.0KHCT-ND	
14	16	R51-66	RES 18.7K OHM 1/10W 1% 0603 SMD	18.7K	ERJ-3EKF1872V	Panasonic	P18.7KHCT-ND	
15	16	R33-48	RES 1.00K OHM 1/10W 1% 0603 SMD	1K	ERJ-3EKF1001V	Panasonic	P1.00KHCT-ND	
16	16	T1-16	THERMISTOR NTC .065"DIA 10K OHM	10K	MC65F103B	GE	235-1058-ND	
18	1	U1	IC UNREG CHG PUMP V-INV SOT23-5		TPS60403QDBVRQ1	TI	296-18036-1-ND	
1	16	U2-17	IC AMP INSTR SGL R-R OUT 8-SOIC		AD623	Analog	AD623ARZ-ND	
8	1	U18	IC REF LDO PREC 2.5V SOT23-5		LM4132BMF-2.5/NOPB	National	LM4132BMF-2.5CT-ND	

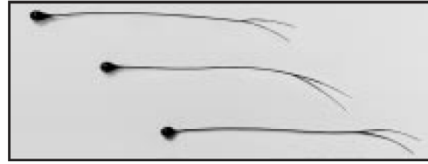


NTC THERMISTORS: TYPE MC65

INSULATED LEAD INTERCHANGEABLE CHIP THERMISTOR

DESCRIPTION:

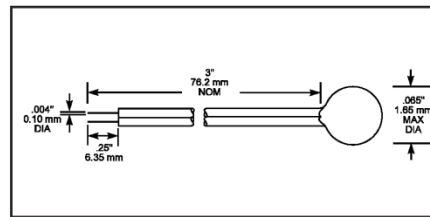
Epoxy Coated interchangeable chip thermistors with heavy isomid insulated Nickel lead-wires.



FEATURES:

- Precision, solid state temperature sensor
- Interchangeability down to $\pm 0.05^\circ\text{C}$
- Suitable for use over the range of -40°C to $+105^\circ\text{C}$
- High sensitivity greater than $-4\%/^\circ\text{C}$ at 25°C
- Suitable for temperature measurement, control and compensation
- High reliability and stability over interchangeable range
- Special tight tolerances in the clinical range for Medical applications
- Most popular R-vs-T curves are available
- Fully insulated
- Resin coated for good mechanical strength and resistance to solvents
- .004" (.1 mm) dia. heavy isomid insulated Bifilar Nickel lead-wires

DIMENSIONS:



Select appropriate part number below for resistance and temperature tolerance desired

R _{25°C}	MATERIAL SYSTEM	$\pm .05^\circ\text{C}; 35^\circ\text{C to } 39^\circ\text{C}$		$\pm .1^\circ\text{C}; 35^\circ\text{C to } 39^\circ\text{C}$		$\pm .15^\circ\text{C}; 35^\circ\text{C to } 39^\circ\text{C}$	
		$\pm .075^\circ\text{C}; 39^\circ\text{C to } 42^\circ\text{C}$	$\pm .10^\circ\text{C}; 20^\circ\text{C to } 45^\circ\text{C}$	$\pm .15^\circ\text{C}; 20^\circ\text{C to } 45^\circ\text{C}$	$\pm .2^\circ\text{C}; 0^\circ\text{C to } 50^\circ\text{C}$	$\pm .2^\circ\text{C}; 20^\circ\text{C to } 45^\circ\text{C}$	$\pm .25^\circ\text{C}; 0^\circ\text{C to } 50^\circ\text{C}$
2252	F	MC65F232A	MC65F232B	MC65F232C			
3000	F	MC65F302A	MC65F302B	MC65F302C			
5000	F	MC65F502A	MC65F502B	MC65F502C			
10000	F	MC65F103A	MC65F103B	MC65F103C			
10000	Y	MC65Y103A	MC65Y103B	MC65Y103C			
30000	H	MC65H303A	MC65H303B	MC65H303C			
50000	G	MC65G503A	MC65G503B	MC65G503C			
100000	Y	MC65Y104A	MC65Y104B	MC65Y104C			
100000	G	MC65G104A	MC65G104B	MC65G104C			

OPTIONS:

Consult factory for availability of options:

- Other resistance values in the range of 100Ω - $100k\Omega$
- Other tolerances or ranges
- Other lead wires or lengths
- Non standard R-vs-T curves
- Controlled dimensions

DATA:

THERMAL AND ELECTRICAL PROPERTIES:

Dissipation constant:.....(still air) .5 mW/ $^\circ\text{C}$
(stirred oil) 4 mW/ $^\circ\text{C}$

Thermal time constant:.....(still air) 8 sec.
(stirred oil) .5 sec.

Maximum power at 25°C25mW
(derated from 100% at 25°C to 0% at 100°C)

Crown Industrial Estate, Priorswood Road
Taunton, Somerset TA2 8QY UK
Tel +44 (0) 1823 335200
Fax +44 (0) 1823 332637

808 US Highway 1
Edison, New Jersey 08817-4695 USA
Tel +1 (732) 287 2870
Fax +1 (732) 287 8847

967 Windfall Road
St. Marys, Pennsylvania 15857-3397 USA
Tel +1 (814) 834 9140
Fax +1 (814) 781 7969

A.5 DUPONT™ NAFION® PFSA MEMBRANES



N 115, N 117, N 1110

Description

DuPont™ Nafion® PFSA membranes are non-reinforced films based on chemically stabilized perfluorosulfonic acid/PTFE copolymer in the acid (H⁺) form. The physical properties remain the same for the chemically stabilized membranes, which exhibit substantially lower fluoride ion release compared to the non-stabilized polymer – a sign of improved chemical durability. Nafion® PFSA membranes are widely used for Proton Exchange Membrane (PEM) fuel cells and water electrolyzers. The membrane performs as a separator and solid electrolyte in a variety of electrochemical cells that require the membrane to selectively transport cations across the cell junction. The polymer is chemically resistant and durable.

Order and Packaging Information

Membrane dimensions are based on dry product conditioned at 23 °C and 50% Relative Humidity before cutting. The membrane's water content will affect its dimensions, and the change may not be symmetrical in the length, width, and thickness directions. In addition, certain conditioning steps performed by the customer also may affect the dimensions. Customers may wish to review their membrane treatment steps and dimensional requirements with a Nafion® technical representative before establishing membrane shipping dimensions.

Standard dry product dimensions for individual pieces include:

Width: 0.30 m (min.) to 1.22 m (max.)

Length: 0.30 m (min.) to 1.22 m (max.)

The membrane delivery package for cut pieces will depend on the size and quantity of the membrane order. Smaller-sized membranes are shipped flat, while longer lengths of individual pieces are shipped on a roll. The membranes are protected with a polyethylene wrap and inner packaging, then placed in shipping containers.

Standard dry product dimensions for roll goods include:

Width: 12-in (0.305-m) and 24-in (0.610-m) standard roll widths, and roll widths from 0.20-m (min.) up to 1.22-m (max.) on special order. Intermediate widths available in increments of 0.125-in.

Length: 50-meter standard roll length

There is a 100 m² minimum order requirement for non-standard roll widths and lengths. Membrane pieces or rolls can be cut to custom sizes, and special packaging provided at additional cost and/or delivery time. Please contact Nafion® customer service for details.



The miracles of science™

Properties of Nafion® PFSA Membrane

A. Thickness and Basis Weight Properties¹

Membrane Type	Typical Thickness (microns)	Basis Weight (g/m ²)
N 115	127	250
N 117	183	360
N 1110	254	500

B. Physical and Other Properties²

Property	Typical Value	Test Method
Physical Properties		
Tensile Modulus, MPa (kpsi)		
50% RH, 23 °C	249 (36)	ASTM D 882
water soaked, 23 °C	114 (16)	ASTM D 882
water soaked, 100 °C	64 (9.4)	ASTM D 882
Tensile Strength, maximum, MPa (kpsi)		
50% RH, 23 °C	43 (6.2) in MD, 32 (4.6) in TD	ASTM D 882
water soaked, 23 °C	34 (4.9) in MD, 26 (3.8) in TD	ASTM D 882
water soaked, 100 °C	25 (3.6) in MD, 24 (3.5) in TD	ASTM D 882
Elongation at Break, %		
50% RH, 23 °C	225 in MD, 310 in TD	ASTM D 882
water soaked, 23 °C	200 in MD, 275 in TD	ASTM D 882
water soaked, 100 °C	180 in MD, 240 in TD	ASTM D 882
Tear Resistance - Initial, g/mm		
50% RH, 23 °C	6000 in MD, TD	ASTM D 1004
water soaked, 23 °C	3500 in MD, TD	ASTM D 1004
water soaked, 100 °C	3000 in MD, TD	ASTM D 1004
Tear Resistance ³ - Propagating, g/mm		
50% RH, 23 °C	>100 in MD, >150 in TD	ASTM D 1922
water soaked, 23 °C	92 in MD, 104 in TD	ASTM D 1922
water soaked, 100 °C	74 in MD, 85 in TD	ASTM D 1922
Specific Gravity	1.98	—
Other Properties		
Conductivity, S/cm	0.10 min	see footnote ⁴
Available Acid Capacity, meq/g	0.90 min	see footnote ⁵
Total Acid Capacity, meq/g	0.95 to 1.01	see footnote ⁵

¹ Measurements taken with membrane conditioned to 23 °C, 50% relative humidity (RH).

² Physical Properties measured for N 115. Where specified, MD - machine direction, TD - transverse direction. Conditioning state of membrane given. Measurements taken at 23 °C, 50% RH.

³ Tear resistance (g/mm) of dry membrane increases with thickness. Values given measured using 50 micron membrane.

⁴ Conductivity measurement as described by Zawodzinski, et al. *J. Phys. Chem.*, 95 (15), 6040 (1991). Membrane conditioned in 100 °C water for 1 hour. Measurement cell submersed in 25 °C D.I. water during experiment. Membrane impedance (real) taken at zero imaginary impedance.

⁵ A base titration procedure measures the equivalents of sulfonic acid in the polymer, and uses the measurement to calculate the acid capacity or equivalent weight of the membrane.

Properties of Nafion® PFSA Membrane

C. Hydrolytic Properties²

Property	Typical Value	Test Method
Hydrolytic Properties		
Water content, % water ⁶	5	ASTM D 570
Water uptake, % water ⁷	38	ASTM D 570
Thickness change, % increase		
from 50% RH, 23 °C to water soaked, 23 °C	10	ASTM D 756
from 50% RH, 23 °C to water soaked, 100 °C	14	ASTM D 756
Linear expansion, % increase ⁸		
from 50% RH, 23 °C to water soaked, 23 °C	10	ASTM D 756
from 50% RH, 23 °C to water soaked, 100 °C	15	ASTM D 756

Recommended Roll Storage Conditions

Unopened roll packages of Nafion® PFSA membrane should be stored in the original shipping box, out of direct sunlight, and in a climate-controlled environment, maintained at 10 to 30°C, and 30 to 70% relative humidity. Before opening the package, pre-condition the membrane roll to the processing area temperature for 24 hours.

Once opened and exposed to the environment, the membrane will equilibrate to the ambient relative humidity, and change in dimensions accordingly. Membrane order dimensions are specified and measured at 23°C and 50% Relative Humidity.

Handling Practices

Ventilation should be provided for safe handling and processing of Nafion® PFSA membrane. The amount of local exhaust necessary for processing Nafion® PFSA membrane at elevated temperatures will depend on the combined factors of membrane quantity, temperature, and exposure time.

Scrap Disposal

Preferred disposal options are (1) recycling and (2) landfill. Incinerate only if incinerator is capable of scrubbing-out hydrogen fluoride and other acidic combustion products. Treatment, storage, transportation, and disposal must be in accordance with applicable federal, state/provincial and local regulations.

Safe Handling and Use of Nafion® PFSA Membranes

The following information should be reviewed before handling and processing Nafion® PFSA Membranes:

- DuPont Material Safety Data Sheet for Nafion® PFSA Membranes N115, N117 and N1110
- "Safe Handling and Use of Perfluorosulfonic Acid Products" bulletin (DFC301.0209).
- "Guide to Safe Handling of Fluoropolymer Resins", Fourth Edition, November 2005, Published by the Fluoropolymers Division of the Society of the Plastics Industry, Inc.

⁶ Water content of membrane conditioned to 23 °C, 50% relative humidity (RH), compared to dry weight basis.

⁷ Water uptake from dry membrane to water soaked at 100 °C for 1 hour (dry weight basis).

⁸ Typical MD and TD values. MD expansion is slightly less than TD.

For information about product offerings from DuPont Fuel Cells, contact:

UNITED STATES, CANADA, MEXICO and CENTRAL AMERICA

Nafion® Membranes and Dispersions

MEA Components

DuPont Fuel Cells
P.O. Box 80701
Wilmington, DE 19880-0701
Tel: (302) 774-1258 or (800) 207-0756 (USA only)

EUROPE, MIDDLE EAST and AFRICA

Nafion® Membranes and Dispersions

DuPont
Via A. Volta 16
20093 Cologno Monzese
Milano, Italy
Fax: +39.02.27300969

MEA Components

DuPont
2 Chemin du Pavillion
CH-1228 Le Grand-Saconnex
Geneva, Switzerland
Fax: +41.22.717.5411

JAPAN

DuPont Kabushiki Kaisha
4th Floor Chiyoda Honsha Bldg.
5-18, Sarugaku-cho 1-chrome
Chiyoda-Ku, Tokyo 101-0064
Fax: (03) 5281-5899

SOUTH AMERICA

DuPont do Brasil SA
Alameda Itapecuru, 506 – Alphaville
Barueri - S.P.
Brasil
CEP 06454-080

CHINA

DuPont China Holding Co., Ltd.
15th Floor, Shui On Plaza
333 Huai Hai Road (Central)
Shanghai 200021, China

KOREA

DuPont Korea, Inc.
3-5th Floors, Asia Tower #726
Yeoksam-dong, Kangnam-Ku
Seoul 135-719 Korea

TAIWAN

DuPont Taiwan Limited
Hung Kuo Bldg.
13th Floor, 167 Tun Hwa North Road
Taipei, Taiwan 105

INDIA

E.I. DuPont India Pvt. Ltd.
DLF Plaza Tower
DLF Qutab Enclave, Phase 1
Gurgaon 122 002
Haryana, India

fuelcells.dupont.com

Copyright © 2009 DuPont or its affiliates. The DuPont Oval Logo, DuPont™, The miracles of science™, Nafion® and all products denoted with ™ are trademarks or registered trademarks of E. I. du Pont de Nemours and Company or its affiliates. DFC101.0209

The data listed here fall within the normal range of product properties, but they should not be used to establish specification limits nor used alone as the basis of design. This information is based on technical data that DuPont believes to be reliable. It is intended for use by persons having technical skill and at their own discretion and risk. This information is given with the understanding that those using it will satisfy themselves that their particular conditions of use present no health or safety hazards. Because conditions of product use are outside our control, DuPont makes no warranties, express or implied, and assumes no obligation or liability in connection with any use of this information or for results obtained in reliance thereon. The disclosure of the information is not a license to operate under or a recommendation to infringe any patent of DuPont or others.

Caution: Do not use in medical applications involving permanent implantation in the human body. For other medical applications, see "DuPont Medical Caution Statement", H-50102.



The miracles of science™